Contributions to Efficient Finite Element Solvers for Time-Harmonic Wave Propagation Problems

Axel Modave

INSTITUT POLYTECHNIQUE DE PARIS

ENSTA

IP PARIS

Habilitation à Diriger des Recherches

Contributions to Efficient Finite Element Solvers for Time-Harmonic Wave Propagation Problems

Mémoire d'Habilitation à Diriger des Recherches de l'IP Paris
préparé au laboratoire POEMS (CNRS, Inria, ENSTA Paris)

Habilitation présentée et soutenue à Palaiseau, le 24 juin 2024, par

Axel Modave

Jury :

Dr Hélène Barucq *[présidente]*	Inria (MAKUTU), UPPA, France
Dr Marc Bonnet	CNRS (POEMS), ENSTA Paris, France
Prof. Bruno Després *[rapporteur]*	Sorbonne Université, France
Prof. Victoria Dolean	TU Eindhoven, Pays-Bas
Prof. Patrick Le Tallec *[rapporteur]*	École Polytechnique, France
Prof. Gwénaël Gabard	Université du Mans, France
Prof. Martin Gander *[rapporteur]*	Université de Genève, Suisse
Dr Pierre Gosselet	CNRS (LaMcube), Université de Lille, France

Invité :

Prof. Christophe Geuzaine	Université de Liège, Belgique

Abstract

The numerical simulation of wave propagation phenomena is of paramount importance in many scientific and engineering disciplines. Many time-harmonic problems can be solved with finite elements in theory, but the computational cost is a strong constraint that limits the size of the problems and the accuracy of the solutions in practice. Ideally, solution techniques should provide the best accuracy at minimal computational cost for real-world problems. They should take advantage of the power of modern parallel computers, and they should be as easy as possible to use for the end user. In this HDR thesis, contributions are presented on three topics: the improvement of domain truncation techniques (i.e. high-order absorbing boundary conditions and perfectly matched layers), the acceleration of substructuring and preconditioning techniques based on domain decomposition methods (i.e. non-overlapping domain decomposition methods with interface conditions based on domain truncation techniques), and the design of a new hybridization approach for efficient discontinuous finite element solvers.

Remerciements / Acknowledgements

Je souhaite remercier l'ensemble des collègues avec lesquels j'ai eu l'opportunité de collaborer depuis mon arrivée au CNRS en 2016. Je remercie tout d'abord Xavier Antoine, Hadrien Bériot, Stéphanie Chaillat, Patrick Ciarlet et Christophe Geuzaine pour les premières collaborations, ainsi que Ruiyang Dai et Anthony Royer pour nos travaux en lien avec leurs thèses. Je suis très heureux des collaborations plus récentes avec Théophile Chaumont-Frelet, Victorita Dolean, Gwénaël Gabard et Pierre Marchand. Nos échanges et nos projets m'inspirent et me motivent énormément. Je remercie tout particulièrement mes doctorants (Damien Chicaud, Simone Pescuma et Timothée Raynaud) et mes post-doctorants (Rose-Cloé Meyer et Ari E. Rappaport) pour leur confiance et leur implication.

J'ai la grande chance de faire partie du laboratoire POEMS, au sein de l'Unité de Mathématiques Appliquées (UMA) de l'ENSTA Paris. L'environnement y est stimulant et bienveillant. Je salue et je remercie l'ensemble de mes collègues, qui contribuent à cet environnement, et dont la liste exhaustive serait longue et difficile à établir. Je souhaite remercier plus spécifiquement Anne-Sophie Bonnet-Ben Dhia, Frédéric Jean, Éliane Bécache et Corinne Chen, pour leur aide précieuse sur la gestion des projets, des missions et/ou des doctorants.

J'ai vu la rédaction et la soutenance de cette habilitation à diriger des recherches comme une opportunité de faire le point et de prendre un peu de recul sur mes travaux. Je suis très honoré d'avoir pu la soutenir devant Hélène Barucq, Marc Bonnet, Bruno Després, Victorita Dolean, Patrick Le Tallec, Gwénaël Gabard, Martin Gander et Pierre Gosselet. Je les remercie d'avoir accepté de faire partie du jury, et pour les échanges que ceci a permis. Je remercie tout particulièrement les trois rapporteurs.

Enfin, *last but not least*, je remercie Cédric pour son soutien et sa patience tout au long de la préparation de cette habilitation. Une aventure de plus qui se termine!

$\sim$

This work was supported in part by the ANR JCJC project WavesDG (research grant ANR-21-CE46-0010) and by the *Agence de l'Innovation de Défense* [AID] through *Centre Interdisciplinaire d'Etudes pour la Défense et la Sécurité* [CIEDS] (project 2022 ElectroMath).

Contents

Chapter 1

Context and statement

1.1 Scientific context

The numerical simulation of *wave propagation phenomena* is of paramount importance in many scientific and engineering disciplines. Aircraft noise reduction, medical imaging, electromagnetic compatibility study, non-destructive testing and seismic risk assessment are examples where reliable simulations play an essential role. In these examples, many physical phenomena are dictated by the frequency of waves. When the number of frequencies of interest is limited, frequency-domain procedures based on the numerical solution of *time-harmonic problems* are commonly used. The Helmholtz equation is a typical example. Such problems are solved to simulate wave propagation in the harmonic regime at a given frequency, whereas time-dependent problems are better suited to the study of transient phenomena.

To obtain reliable time-harmonic numerical solutions for real-world problems in reasonable time, numerical schemes must be accurate, robust and computationally efficient. Today, several approaches are well established, such as the asymptotic, collocation and boundary element methods based on *boundary integral equations* (BIEs), and the finite difference, finite volume and finite element methods based on *partial differential equations* (PDEs). The BIE-based methods naturally deal with wave propagation in unbounded domains, and the degrees of freedom are associated only with the interfaces/boundaries of the domain. Unfortunately, they rely on fundamental solutions that are generally known only for problems with homogeneous media. In contrast, complex material properties and more general physical problems can be treated with PDE-based methods. However, the degrees of freedom are associated with the entire mesh/grid of the domain, and the computational domain must be artificially truncated to simulate phenomena occurring in unbounded regions. All of these approaches are generally competitive for ranges of applications, not necessarily the same, and much effort is currently being invested to overcome their limitations and to improve the computational efficiency of each one of them.

In this work, we consider *finite element methods* (FEMs), which are a very popular family of numerical methods. They are widely used to solve real-world applications because of their ability to reliably represent complex geometric configurations and heterogeneous media. They are versatile thanks to formulations based on weak forms of the equations, the possibility of using unstructured meshes and high-order discretization techniques, and flexibility in the choice of the basis functions used to represent the numerical solutions. However, when solving large-scale time-harmonic problems, the two main difficulties inherent to the PDE-based methods remain (1) the artificial truncation of the computational domain, and (2) the computational cost required to solve the algebraic system arising from the discretization.

Efficient domain truncation techniques. Many wave propagation problems are naturally defined on large or infinite spatial domains, while the finite element solution procedures should be performed on computational domains as small as possible in order to limit the computational cost. In practice, the numerical solutions are computed with modified problems defined on *truncated domains* with artificial

boundaries. Although these boundaries are not physical, they must be carefully modeled in order to recover the solutions corresponding to the original physical problems. If the exterior problem can be simulated with a BIE-based method, the FEM solver can be coupled to that method. This approach is accurate, but results in significant additional cost due to the nonlocal nature of this type of method, which leads to dense matrix blocks in the discrete weak formulation. The cheapest approach is to use a Robin boundary condition, which is very easy but introduces modeling errors that can be significant in some cases. Alternative approaches, such as *high-order absorbing boundary conditions* (HABCs) and *perfectly matched layers* (PMLs), can provide better accuracy at a moderately higher computational cost. In practice, there is a trade-off between accuracy and computational cost when selecting and tuning a domain truncation technique. An efficient technique should be accurate, robust, easy to use and competitive from a computational cost perspective.

Large indefinite sparse algebraic system. Designing efficient computational solvers for time-harmonic problems using finite element methods is notoriously difficult because it involves solving large algebraic systems for which the matrices are sparse, complex and indefinite. The number of *degrees of freedom* (DOFs) can be very large because the mesh cells must be small enough to accurately represent the oscillations of waves, as well as any phenomena related to wave-structure interactions. Moreover, in the high-frequency regime, corresponding to situations where the wavelength is very small compared to the characteristic size of the structures, the pollution error requires the refinement of the mesh and/or the use of high-order basis functions, further increasing the size of the systems. Unfortunately, the standard algebraic methods are not very efficient for solving such linear systems. On the one hand, sparse direct methods exhibit poor scalability in terms of memory and computational time in parallel environments. On the other hand, most iterative methods that have proven successful for coercive problems become inefficient when applied to indefinite problems. General strategies based on *hp-adaptivity* and *static condensation* help to reduce the number of DOFs for a given accuracy, as well as the computational cost with both direct and iterative methods. However, they do not overcome the inherent limitations of the standard direct/iterative methods, and they do not lead to scalable solution methods.

Wave-specific strategies to speed up iterative procedures. Iterative methods can be accelerated by using, in one way or another, some knowledge about the time-harmonic problems. The resulting solvers can be very specific, but they can be much more efficient for the considered problems. Many complementary and competing approaches have been proposed over the last decades, and they are still intensively studied in the applied mathematics and computational engineering research communities. For example, substructuring and preconditioning techniques based on *domain decomposition methods* (DDMs) aim at reducing the number of iterations. They rely on using, at each iteration, of the solutions of local problems defined on subdomains in a partition of the physical domain. A first *wave-specific* strategy consists in using transmission operators based on domain truncation techniques at the interfaces between the subdomains. Another approach, called *sweeping* preconditioners, involves solving the local problems in a specific order that mimics the wave propagation across the domain partition. *Discontinuous finite element methods* offer flexibility in the choice of the basis functions, and several ways to weakly enforce the continuity of the solution at the interface between the elements. Examples of wave-specific strategies include the use of an *ultra-weak variational formulation* (UWVF) with interface conditions related to absorbing boundary operators.

Many time-harmonic problems can be solved with finite elements in theory, but the computational cost is a strong constraint that limits the size of the problems and the accuracy of the solutions in practice. The goal is to combine the best strategies for each specific case. Ideally, each combination should provide the best accuracy at minimal computational cost for real-world problems. It should take advantage of the power of modern computers, consisting of many-core processors and accelerators. It should be as easy to use as possible for the end user.

1.2 Context of this habilitation

Since the beginning of my career, I have been working on strategies to improve and accelerate finite element solvers for large-scale wave propagation problems in the perspective of real-world applications. This topic is at the intersection of engineering sciences, applied mathematics and high-performance computing, which are my areas of interest. In this manuscript, I present more specifically my contributions to *efficient time-harmonic finite element solvers*, on which I started working on shortly after being hired as a CNRS researcher. All these contributions have been obtained in the context of collaborations, which are listed in the next section.

I joined the POEMS laboratory (Palaiseau, France) as a CNRS researcher in October 2016, after a PhD in Belgium, and postdoctoral positions in Belgium and in the USA. POEMS is at the same time a research laboratory associated to the CNRS Section 09 (topics: solid mechanics, materials and structures, biomechanics, acoustics), a project team of the *Inria Saclay Center*, and a research team of the *Applied Mathematics Unit* of ENSTA Paris. The research activities of POEMS are mainly dedicated to the analysis and numerical simulation of wave propagation phenomena. The team is composed of about 15 permanent researchers and academics, who can be considered as applied mathematicians, mechanical engineers, or a blend of both profiles. I would place myself in the latter category.

While I had only worked on *time-dependent problems* during my PhD and postdoctoral studies, I decided to focus my activities on *time-harmonic problems* shortly after arriving at POEMS. From a computational point of view, designing efficient solvers for time-harmonic problems turned out to be much more challenging than for time-dependent problems, and I was glad to start working on these new challenges. I had, and I still have, the ambition to develop efficient GPU-accelerated finite element solvers for solving time-harmonic problems.

The contributions presented in this manuscript are grouped into three topics: the improvement of *domain truncation techniques*, the acceleration of substructuring and preconditioning techniques based on *domain decomposition methods*, and the design of a new hybridization approach for efficient *discontinuous finite element solvers*. These contributions are presented for time-harmonic scalar wave problems, but generalizations are discussed in the last chapter of the manuscript.

Three of my research projects are not covered in this manuscript: the analysis of time-harmonic electromagnetic problems with anisotropic/complex media (related to the PhD of D. Chicaud), the coupling of a discontinuous finite element method and a spectral method for time-dependent acoustic problems (related to the postdoctoral research of R.-C. Meyer) and the convergence analysis of Krylov's methods for solving time-harmonic problems with finite elements (related of the PhD of T. Raynaud). The first one is briefly summarized at end of Section 1.3, and the other two are in their early stages.

Organization of the manuscript. The remainder of this chapter contains a summary of my contributions (Section 1.3), and a list of my mentoring activities and funded research projects (Section 1.4). The main chapters of this manuscript are dedicated to a presentation of contributions organized by topic: domain truncation methods (Chapter 2), domain decomposition methods (Chapter 3), and discontinuous finite element solvers (Chapter 4). In these chapters, each section is either a general presentation of a topic, or a summary of a contribution. Open questions, ongoing works and future research directions are discussed in Chapter 5. The bibliography at the end of this manuscript is divided into works of which I am a co-author (references starting with the letter "A", e.g. [A1]) and other works (references without a letter, e.g. [1]).

1.3 Contributions, collaborations and positioning

In this section, I summarize my contributions with emphasis on the novelties and collaborative networks. All my contributions have been obtained in collaborations.

During my PhD studies with C. Geuzaine (ULiège, Belgium) and my postdoctoral research with T. Warburton (VirginiaTech, USA), I mainly worked on finite element solvers for *time-dependent problems*. More specifically, I improved domain truncation techniques [A5, A7, A8, A10, A11] and I accelerated discontinuous Galerkin finite element solvers thanks to GPU computing [A2, A13, A14, A5]. For the second topic, I had the opportunity to work with researchers from oil and gas companies, Shell and TotalEnergies, which gave me a taste for industrial collaborations. After arriving at POEMS in October 2016, I completed ongoing works related to my PhD and postdoctoral researches, and then I quickly started working on time-harmonic problems.

About domain truncation methods [Chapter 2]

When using a HABC at the artificial boundary of a truncated domain, modeling errors can be reduced by increasing the number of auxiliary fields in the HABC or by using higher order partial derivatives. Similarly, modeling errors due to PMLs can generally be reduced by increasing their thickness. In both cases, however, the computational cost increases. My contributions aimed at (1) improving the implementations to deal with convex truncated domains of general shape (providing geometric flexibility when choosing the shape of the domain) and (2) guiding the selection of the HABC or PML parameters. The ultimate goal of the practical challenges is to achieve the best accuracy at the lowest cost.

In collaboration with X. Antoine (Lorraine U., IECL) and C. Geuzaine, we have studied corner treatments for Padé-type HABCs for the finite element solution of Helmholtz problems with polygonal/polyhedral computational domains [A9]. To the best of our knowledge, only a few corner treatments for HABCs were available in the literature, and no extensive accuracy studies were proposed. We have developed and compared approaches based on (1) compatibility relations at the corners and (2) formulations for curved boundaries with numerical curvatures at the corners. The compatibility relations were obtained for corners with right angles. They work perfectly for these cases, and they can be used empirically as is for non-right angles. We have observed that the first approach is better for angles close to $\pi/2$, and the second one is better for configurations with very obtuse angles.

In collaboration with H. Bériot (SIEMENS, Belgium), we have studied a comprehensive PML implementation strategy for the finite element solution of acoustic scattering problems with convex truncated domains of general shape [A1]. The direct implementation of a standard PML formulation for convex domains requires the knowledge of geometric data in the layer, which are not always known. Our strategy requires only the knowledge of the mesh of the exterior boundary of the domain. The layer and the required geometric data are generated during an extrusion process. The PML is included in the scheme thanks to a specific modification of the reference Jacobian matrix in the element-wise finite element integrals. This approach can be considered as a specific finite element approximation of the *conformal PML* for domains with smooth boundaries, and it is an empirical technique for domains with corners. It has been implemented in a toolbox developed by SIEMENS for solving acoustic scattering problems. The end user has only to specify the thickness of the layer, the distance between the scattering object and the boundary of the computational domain.

About domain decomposition methods [Chapter 3]

I contributed to the design of a class of DDM solvers with non-overlapping subdomains and transmission conditions based on domain truncation methods. This approach finds its origin in a seminal work of Després [97, 99] on a DDM iterative scheme for the parallel solution of Helmholtz problems, which was related to works of Lions [215]. At each iteration of the scheme, the Helmholtz equation is solved on

each subdomain with Robin transmission conditions at the interfaces between the subdomains. Then, transmission data are exchanged between the subdomains. Over time, many extensions have been proposed, see e.g. [135, 137, 139]. For example, the Robin transmission condition can be replaced with more general conditions. Transmission conditions based on HABCs and PMLs have been used empirically to locally reproduce the transmission of waves at the interfaces between subdomains. The iteration can be combined with Krylov methods, and it can also be used as a preconditioner rather than as a solver.

I started working on this topic with X. Antoine and C. Geuzaine, after our collaboration on the corner treatments for HABC. This collaborative network has been extended to E. Béchet (ULiège, Belgium), R. Dai (UCLouvain, Belgium), J.-F. Remacle (UCLouvain, Belgium) and A. Royer (ULiège, Belgium).

In [A12, A15], we have extended non-overlapping DDM solvers with HABC and PML transmission conditions to deal with checkerboard domain partitions. Previous solvers using these conditions were only tailored for 1D domain partitions (e.g. partitions in layers or in onion skins), e.g. [52, 289, 281]. Checkerboard partitions have *interior cross-points* (i.e. interior points of the partition that belong to more than two subdomains) and *boundary cross-points* (i.e. points that belong to both the boundary of the physical domain and at least two subdomains), which require some care. If the *cross-points* are not handled carefully, the convergence of the DDM solvers can be deteriorated. For configurations where the HABC and PML are also used at the boundary of the computational domain, the DDM solvers may even converge to incorrect solutions. We have proposed and studied strategies where the HABC and PML are rewritten as Dirichlet-to-Neuman operators, and where the corner treatments used for these domain truncation techniques are adapted to provide cross-point treatments. The good convergence properties generally observed for 1D domain partitions are then recovered for checkerboard partitions.

Due to the local nature of the data transfers, the DDM solvers with HABC and PML transmission conditions cannot scale with the number of subdomains without an efficient preconditioning technique. In [A4], we have proposed and compared *multidirectional sweeping preconditioners*. Sweeping preconditioners involve solving the local problems associated with subdomains in specific orders, mimicking the wave propagation across the domain partition. Depending on the strategy, the problems can be solved forward, backward, or in both directions simultaneously. Several approaches have been studied for 1D domain partitions, e.g. [233, 270, 290, 138]. We have extended some of them for checkerboard domain partitions by combining sweeps in multiple directions (e.g. horizontal, vertical and diagonal), by using sequential and parallel sweeps, and by alternating the sweeps thanks to a flexible version of GMRES. These preconditioners provide an efficient way to quickly transfer information to the different regions of the computational domain, and then they accelerate the convergence of iterations.

In parallel to my collaboration with the *"belgian network"*, I started a collaboration with P. Ciarlet (ENSTA Paris, POEMS) on *time-harmonic electromagnetic problems* with complex anisotropic media. Our initial motivation was to extend and to analyze DDMs for a general class of material tensor fields, which first required a careful analysis of the PDE problems. We co-advised the PhD research of D. Chicaud (ENSTA Paris, POEMS) [69] on the mathematical analysis of these problems [A3], with preliminary results on DDMs. We have clarified the functional framework for material tensor fields that verify an ellipticity condition, and we have obtained preliminary theoretical results on the convergence of the DDM iterative scheme. We are continuing this work in the context of the CIEDS project *ElectroMath*, obtained with colleagues from POEMS and IDEFIX (the sibling Inria team of POEMS at ENSTA Paris). This research direction, which is still a work in progress, is presented in Chapter 5.

About discontinuous finite element methods [Chapter 4]

The finite element methods used to solve time-harmonic problems are generally conformal. The numerical solutions are represented by continuous basis functions belonging to the space of physical solutions, and *hp-adaptivity* and *static condensation* can be used to improve the accuracy and to reduce the number of DOFs, e.g. [40]. Several nonconformal approaches with discontinuous basis functions, which do not belong to the space of physical solutions, have been investigated in the last decades. In particular, the

hybridizable discontinuous Galerkin (HDG) methods, originally proposed for diffusion problems [80], have been applied and studied for time-harmonic problems e.g. in [229, 157, 65]. These methods are based on standard *discontinuous Galerkin* (DG) formulations, the definition of auxiliary variables associated with *numerical traces* on the faces of the elements, and the elimination of the physical unknowns from the system, leading to a *reduced system* or *hybrid system* associated only with the auxiliary variables.

In 2021, I received a ANR JCJC grant for the project *WavesDG* to work on accelerated DG finite element solvers for time-harmonic problems. In collaboration with T. Chaumont-Frelet (Inria, RAP-SODI), we have obtained promising first results for Helmholtz problems. In [A6], we have proposed and analyzed a new HDG method with auxiliary variables associated to *characteristic variables*. At the cost of increasing the memory required for the reduced system, this choice greatly improves its properties and makes it more suitable for iterative solution procedures. With the new method, called the CHDG method, the reduced system can be written in the form $(\mathrm{I} - \Pi\mathrm{S})g = b$, where I is the identity and the operator $\Pi\mathrm{S}$ is a strict contraction. This system can then be solved with the fixed-point iteration without relaxation. We have observed that the condition numbers of the global reduced matrix and the local element-wise matrices are always smaller with CHDG than with the standard HDG method. We have also observed that the convergence of the GMRES and CGNR iterations is always faster with CHDG than with the standard HDG method. This contribution is the first step of an ongoing work in the context of the ANR project *WavesDG*.

We are currently investigating extensions in the context of the PhD research project of S. Pescuma (ENSTA Paris, POEMS), which I supervised together with G. Gabard (Le Mans U., LAUM). With the ANR project *WavesDG*, my ultimate goal is to develop a FEM solver for time-harmonic problems that would be efficient on GPU clusters.

Other works

About the analysis of time-harmonic electromagnetic problems. The numerical simulation of time-harmonic electromagnetic problems with anisotropic/complex media is an important tool for the design of optical metamaterials/metasurfaces, and for the study of wave propagation in plasmas. The mathematical and numerical analysis of Maxwell problems with isotropic media is well known. Results exist for anisotropic media, but they are generally restricted to real symmetric (or complex Hermitian) positive definite material tensors, see e.g. [14]. In the context of the PhD research of D. Chicaud [A3, 69, 70], we have studied time-harmonic electromagnetic problems with *elliptic* material tensor fields, which are a general class of material coefficients. We have considered boundary value problems with Dirichlet, Neumann, and Robin boundary conditions. For each problem, we have derived an extended functional framework, we proved the well-posedness of a variational formulation, and we have obtained regularity estimates for the solution and its curl, generalizing well-known results. We have paid special attention to the functional spaces involved in the Robin boundary condition. Some of these tools have been used to study the DDM scheme described above, and they provide a solid foundation for further studies planned within the framework of the CIEDS project *ElectroMath*.

About accelerated discontinuous Galerkin solvers for time-dependent acoustic problems. In collaboration with H. Bériot, we obtained a funding from *France Relance*, supplemented with an industrial funding from SIEMENS (France), to work on accelerated DG solvers for time-dependent acoustic problems. The postdoctoral research position of R.-C. Meyer (ENSTA Paris, POEMS) was funded by this project. This project had two parts: acceleration thanks to GPU computing, and acceleration by coupling DG methods with spectral methods. A preprint on the second part is in preparation.

About the convergence of Krylov's methods for time-harmonic acoustic problems. My most recent collaboration concerns the PhD research of T. Raynaud, which I supervise together with P. Marchand (Inria, POEMS) and V. Dolean (TU/e, The Netherlands), funded by the CIEDS project *ElectroMath*. We aim to improve our understanding of the convergence of Krylov methods for solving time-harmonic problems, and then to improve preconditioning strategies.

1.4 List of research projects and mentorship activities

I am the principal investigator or co-principal investigator of the following research projects:

- Project *WavesDG* (2021/12 – 2025/12) funded by the ANR *(Agence Nationale pour la Recherche)* [Call 2021; JCJC; ANR-21-CE46-0010]; **Principal investigator**.
- Industrial project with SIEMENS (2022/01 – 2024/01) funded by *France Relance* and SIEMENS [Call 2021]; **Principal investigator**.
- Project *ElectroMath* (2022/10 – 2026/09) funded by the CIEDS *(Centre Interdisciplinaire d'Etudes pour la Défense et la Sécurité)* [Call 2022]; **Co-principal investigator** with Patrick Ciarlet (ENSTA Paris, POEMS).

I have been, or I am, the co-advisor or mentor of the following PhD students and postdoctoral researchers:

- Damien Chicaud (2018/10 – 2021/12), PhD student co-advised (50%) with Patrick Ciarlet (ENSTA Paris, POEMS) on *"Analysis of time-harmonic electromagnetic problems in elliptic anisotropic media"* [69] (defense 2021/12). Funded by the *Direction Générale de l'Armement (DGA)* and ENSTA Paris. Related publications [A3, 70].
- Rose-Cloé Meyer (2022/01 – 2024/01), postdoctoral researcher on *"Accelerated discontinuous Galerkin solvers for time-dependent acoustic problems"* in the context of an industrial project funded by *France Relance* and SIEMENS.
- Simone Pescuma (since 2022/10), PhD student co-advised (70%) with Gwénaël Gabard (Le Mans U., LAUM) on *hybridizable discontinuous Galerkin methods for time-harmonic problems*. Funded by the ANR project *WavesDG*.
- Timothée Raynaud (since 2023/10), PhD student co-advised (40%) with Pierre Marchand (Inria, POEMS) and Victorita Dolean (TU/e, The Netherlands) on *"Analysis and acceleration of Krylov iterative methods for the numerical solution of time-harmonic wave problems"*. Funded by the CIEDS project *ElectroMath*.
- Ari Rappaport (since 2023/04), postdoctoral researcher on *"Hybridizable discontinuous finite element method for time-harmonic electromagnetism in complex media"*. Funded by the CIEDS project *ElectroMath*.

I have contributed informally to the following doctoral works:

- Ruiyang Dai. PhD student of Chistophe Geuzaine (ULiège, Belgium) and Jean-François Remacle (UCLouvain, Belgium) on *"Generalized sweeping preconditioners for domain decomposition methods applied to Helmholtz problems"* [91] (defense 2021/10). Related publication [A4].
- Anthony Royer. PhD student of Chistophe Geuzaine (ULiège, Belgium) and Eric Béchet (ULiège, Belgium) on *"Efficient finite element methods for solving high-frequency time-harmonic acoustic wave problems in heterogeneous media"* [257] (defense 2023/04). Related publications [A12, A15].

I have been the scientific advisor or co-advisor for the internship of 7 students: Ningyuan Hu (2^{nd} year engineering student at ENSTA Paris, 2017), Damien Chicaud (3^{nd} year engineering student at ENSTA Paris and M2 student at Paris-Saclay U., 2018), María José Castellano (M2 student at Paris-Saclay U., 2018), Nassim Kesmia (M1 at Paris-Saclay U., 2019), Quentin Krempp (2^{nd} year engineering student at ENSTA Paris, 2020), Simone Pescuma (M2 student at Sorbonnes U. and *Laurea Magistrale* at Politecnico di Milano, 2022) and Timothée Raynaud (M2 student at Paris-Saclay U., 2023).

Chapter 2

Domain truncation methods

High-order absorbing boundary conditions (HABCs) and *perfectly matched layers* (PMLs) are two families of non-reflecting boundary treatments used to simulate wave propagation phenomena in large area with truncated computational domains. They can be considered as intermediate approaches between methods based on *boundary integral equations* (generally more accurate, but more expensive) and basic *absorbing boundary conditions* (cheaper, but generally less accurate). We look for methods that can handle real-world problems with general geometries and complex physical configurations, with the right trade-off between accuracy and computational cost.

To describe the methods, we consider a general Helmholtz problem defined in the unbounded domain $\mathbb{R}^d$ (with $d = 2$ or 3) with a region of interest $\Omega \subset \mathbb{R}^d$ that is bounded. We are looking for the field $u(\boldsymbol{x}) \in H^1_{\text{loc}}(\mathbb{R}^d)$ that verifies

$$\begin{cases} -\Delta u - \kappa^2 u = s, & \text{in } \mathbb{R}^d, \\ \lim\limits_{\|\boldsymbol{x}\|\to\infty} \|\boldsymbol{x}\|^{(d-1)/2} \left(\partial_{\|\boldsymbol{x}\|} - \imath\kappa\right) u = 0, \end{cases} \tag{2.0.1}$$

where the wavenumber $\kappa(\boldsymbol{x})$ is a positive real function that is constant outside Ω, and $s(\boldsymbol{x}) \in L^2(\Omega)$ is a given source function with compact support in Ω. The last equation is the Sommerfeld radiation condition[1], which ensures that the solution is bounded and unique, provided there is no resonance inside Ω. In practice, the finite element simulations are performed on the truncated domain Ω. The solution $u \in H^1(\Omega)$ is then computed by solving

$$\begin{cases} -\Delta u - \kappa^2 u = s, & \text{in } \Omega, \\ \textit{(boundary treatment)} & \text{on } \Gamma := \partial\Omega, \end{cases} \tag{2.0.2}$$

The solution of the modified problem (2.0.2) with domain truncation must be as close as possible to the solution of the original problem (2.0.1). The boundary treatment must represent the outward propagation of the waves, without reflection, at the artificial boundary Γ. Note that these methods can be extended to other physical problems, but it can be quite difficult, and similar methods can be developed for other categories of problems (e.g. waveguide problems). We take the convention that the time-dependence of the fields is $e^{-\imath\omega t}$, where ω is the angular frequency and t is the time.

A general presentation of HABCs and PMLs for Helmholtz problems are proposed in Sections 2.1 and 2.3, respectively. My contributions are described in Sections 2.2 and 2.4.

[1] This condition is motivated by physical considerations: *"The sources must be sources, not sinks, of energy. The energy which is radiated from the sources must scatter to infinity; no energy may be radiated from infinity into the prescribed singularities of the field."* [268]

2.1 Overview of HABCs for Helmholtz problems

Today, a complete review and comparison of *absorbing boundary conditions* (ABCs) for Helmholtz problems would be difficult. We could refer to some old articles of Givoli [145, 146, 147], Hagstrom [161] and Thompson [282]. In this section, we present an overview of HABCs for planar boundaries. We then discuss extensions to deal with curved boundaries, domains with corners and other physical problems. Note that many of the references cited in this section deal with boundary operators proposed for time-dependent problems, for on-surface radiation conditions, or for preconditioned BIE solvers. However, these boundary operators can be used directly to design HABCs for time-harmonic problems.

The simplest ABC for problem (2.0.1) is

$$\partial_n u - \imath\kappa u = 0, \quad \text{on } \Gamma,$$

where ∂_n is the exterior normal derivative. This boundary condition can be interpreted as taking the Sommerfeld condition at a finite distance, or as prescribing the incoming characteristic variable to zero, see e.g. [175]. It is exact in 1D, and it can be used as an approximate condition in 2D and 3D. For cases with more than one dimension, HABCs are generally obtained by using an exact representation of the solution in the exterior domain and/or by approximating an exact nonlocal boundary condition.

2.1.1 Exact planar ABC for the Helmholtz equation

We consider the Helmholtz equation in the unbounded domain $\mathbb{R}^3$, which is decomposed into the interior region $\Omega := \{\boldsymbol{x} = (x, y, z) \in \mathbb{R}^3 : x < 0\}$ and the exterior region $\Omega_{\text{ext}} := \{\boldsymbol{x} \in \mathbb{R}^3 : x > 0\}$ separated by the planar interface $\Gamma := \{x = 0\}$. The exterior medium is assumed to be homogeneous and free of sources. The boundary condition prescribed on Γ must represent the outward propagation of waves leaving Ω. The exact ABC is obtained by solving the exterior Helmholtz problem defined in Ω_{ext} for some Dirichlet data $\bar{u}$ given on Γ [110, 161]. Let $\boldsymbol{y}$ be the position in the tangent plane, such that $\boldsymbol{x} = (x, \boldsymbol{y})$. Applying the multidimensional Fourier transform $\mathcal{F}_{\boldsymbol{y}}$ in the transverse direction to the Helmholtz equation yields

$$\left(\partial_x^2 + \lambda_+\lambda_-\right) \mathcal{F}_{\boldsymbol{y}}[u](x, \boldsymbol{\xi}) = 0, \quad \text{for } x > 0,\ \boldsymbol{\xi} \in \mathbb{R}^2,$$

where $\boldsymbol{\xi}$ is the dual variable of $\boldsymbol{y}$ in the Fourier space, and the symbols λ_+ and λ_- are defined as

$$\lambda_\pm(\boldsymbol{\xi}) := \pm\imath\kappa\sqrt{1 - (\|\boldsymbol{\xi}\|/\kappa)^2}.$$

The only admissible solution reads

$$\mathcal{F}_{\boldsymbol{y}}[u](x, \boldsymbol{\xi}) = \mathcal{F}_{\boldsymbol{y}}[\bar{u}](\boldsymbol{\xi})\, e^{x\lambda_+(\boldsymbol{\xi})},$$

which corresponds to an outgoing propagating wave if $\kappa > \|\boldsymbol{\xi}\|$, a grazing wave if $\kappa = \|\boldsymbol{\xi}\|$ or an evanescent wave if $\kappa < \|\boldsymbol{\xi}\|$. Taking the derivative in x of this solution, applying the inverse Fourier transform $\mathcal{F}_{\boldsymbol{y}}^{-1}$ and taking the restriction on Γ give the exact ABC for the interior problem:

$$\partial_x u = \mathcal{B} u, \quad \text{on } \Gamma,$$

where $\mathcal{B}$ is the pseudo-differential *Dirichlet-to-Neumann* (DtN) operator defined as

$$\mathcal{B} := \mathcal{F}_{\boldsymbol{y}}^{-1}\left[\lambda_+(\boldsymbol{\xi})\, \mathcal{F}_{\boldsymbol{y}}\right] = \imath\kappa\sqrt{1 + \Delta_\Gamma/\kappa^2}, \tag{2.1.1}$$

with the Laplace-Beltrami operator $\Delta_\Gamma := \Delta - \partial_{xx}$. The boundary condition is nonlocal because of the square root in the symbol of $\mathcal{B}$.

2.1.2 Rational approximations of the square root $\sqrt{1+X}$

Local boundary conditions can be derived by approximating the square root in the symbol of the DtN operator (2.1.1). Let define the function $f(X) := \sqrt{1+X}$, where $X = -(\|\boldsymbol{\xi}\|/\kappa)^2$.

Padé approximation. In their seminal paper, Engquist and Majda [110] derived a family of HABCs by using the Padé approximation of the square root. The $(M-1)^{\text{th}}$-order Padé approximation, denoted $f_M^{\text{Padé}}(X)$, can be represented as the continued fraction provided by the sequence [111]

$$\begin{aligned} f_m^{\text{Padé}}(X) &= 1 + \frac{X}{1 + f_{m-1}^{\text{Padé}}(X)}, \qquad \text{with } m = 2, \dots, M, \\ f_1^{\text{Padé}}(X) &= 1, \end{aligned} \tag{2.1.2}$$

or, equivalently, as a sum of rationals [18, 158, 218, A9]

$$\begin{aligned} f_M^{\text{Padé}}(X) &= 1 + \frac{2}{M} \sum_{n=1}^{N} \frac{a_n X}{1 + b_n X} \\ &= 1 + \frac{2}{M} \sum_{n=1}^{N} c_n \left(1 - \frac{c_n + 1}{c_n + 1 + X} \right), \qquad \text{if } M = 2N+1 \text{ is odd}, \\ f_M^{\text{Padé}}(X) &= 1 + \frac{X}{M} + \frac{2}{M} \sum_{n=1}^{N} \frac{a_n X}{1 + b_n X} \\ &= 1 + \frac{X}{M} + \frac{2}{M} \sum_{n=1}^{N} c_n \left(1 - \frac{c_n + 1}{c_n + 1 + X} \right), \qquad \text{if } M = 2N+2 \text{ is even}, \end{aligned} \tag{2.1.3}$$

with $a_n = \sin^2(n\pi/M)$, $b_n = \cos^2(n\pi/M)$ and $c_n = \tan^2(n\pi/M)$. The Padé approximation can also be represented as a product of rationals [158, 218]. To the best of our knowledge, that representation has never been used to derive HABCs.

To study the accuracy of the HABC, we consider the reflection coefficient

$$R(X) = \left| \frac{f(X) - f^{\text{approx}}(X)}{f(X) + f^{\text{approx}}(X)} \right|,$$

where $f^{\text{approx}}(X)$ it the approximate square root, see e.g. [161]. In Figure 2.1, the reflection coefficient is plotted as a function of the decay factor $\rho(X) = \kappa\sqrt{-X-1}$ for evanescent modes (i.e. $X \in]-\infty, -1[$) and as a function of the angle of incidence $\theta(X) = \arcsin(\sqrt{-X})$ for propagating modes (i.e. $X \in]-1, 0[$).

The Padé approximation converges towards the exact value of the square root as M increases, expect when X is on the branch cut of the square root (i.e. $X \in]-\infty, -1[$). Therefore, conditions based on this approximation are perfectly reflective for evanescent modes. For propagating modes, the reflection depends on the angle of incidence. The reflection is small for nearly normal incidences (i.e. with $\|\boldsymbol{\xi}\| \approx 0$ or, equivalently, $\theta \approx 0°$) and large for nearly grazing modes (i.e. with $\|\boldsymbol{\xi}\| \approx \kappa$ or, equivalently, $\theta \approx 90°$).

Padé approximation with rotation of the branch cut. To deal with evanescent modes, the Padé approximation can be applied to the square root after a change of variable to rotate the branch cut by some angle ϕ. For the Padé approximation (2.1.3), we then have

$$f_M^{\phi}(X) = e^{\imath\phi/2}\, f_M^{\text{Padé}}(e^{-\imath\phi}(1+X) - 1) = e^{\imath\phi/2} \Big[1 + \frac{2}{M} \sum_{n=1}^{N} c_n \left(1 - \frac{e^{\imath\phi}(c_n+1)}{(e^{\imath\phi}c_n + 1) + X} \right) \Big].$$

This strategy was first proposed by Milinazzo et al. [228] for parabolic wave equations. The HABC can effectively deal with evanescent modes [10], but it increases the reflection of propagating modes, see Figure 2.1. The effect is more important as the rotating angle ϕ grows.

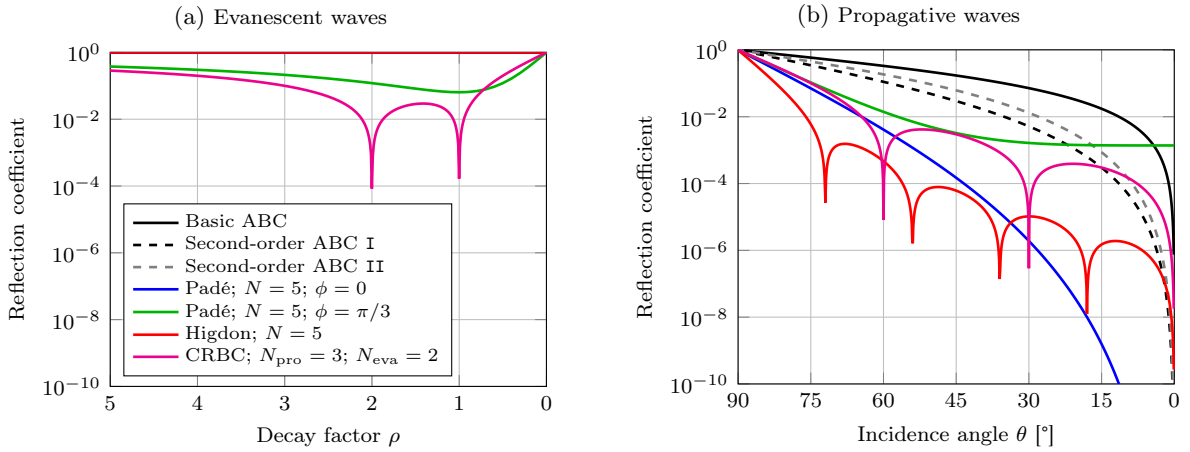

Figure 2.1: Reflection coefficient for evanescent waves *(left)* and propagating waves *(right)* with different approximations of the square root. Incidence angle $\theta = 0°$ corresponds to normal incidence. Grazing waves correspond to $\rho = 0$ and $\theta = 90°$. The second-order ABC `I` and `II` correspond to (2.1.6) and (2.1.8), respectively.

General rational approximations. More general approximations, leading to HABCs possibly more accurate thanks to a larger number of tuning parameters, have been proposed e.g. in [177, 171, 218, 168, 169, 262, 163]. In particular, HABCs proposed by Higdon [177] are exact for propagating waves with angles of incidences of a given set $\{\theta_m\}_{m=1\dots M}$, but they are inefficient for evanescent waves. The *complete radiation boundary conditions* (CRBCs) proposed by Hagstrom and Warburton [168] can deal with both propagating and evanescent modes. These general boundary conditions correspond to the rational approximation $f_M(X)$ provided by the sequence

$$f_m(X) = \alpha_m + \frac{X + 1 - \alpha_m^2}{\alpha_m + f_{m-1}(X)}, \qquad \text{for } m = 2 \dots M, \tag{2.1.4}$$
$$f_1(X) = \alpha_1,$$

where $\{\alpha_m\}_{m=1\dots M}$ are complex coefficients, e.g. [A9]. The real and imaginary parts of these coefficients attenuate respectively propagating and evanescent parts of waves. We have the following coefficients:

- Padé-type HABC without rotation of the branch cut [110, 111]: $\alpha_m = 1$;
- Padé-type HABC with ϕ-rotation of the branch cut [194]: $\alpha_m = e^{\imath\phi/2}$;
- Higdon-type HABC [177, 160, 167]: $\alpha_m = \cos\theta_m$, with $\theta_m \in [0, \pi/2[$;
- CRBC [168]: $\alpha_m = \cos\theta_m - \sigma_m/(\imath\kappa)$, with $\theta_m \in [0, \pi/2[$ and $\sigma_m > 0$.

In an alternative version of the CRBC, the coefficients are separated into a set of purely real parameters and a set of purely imaginary parameters [169, 163, 164].

2.1.3 Planar HABCs for the Helmholtz equation

Formulations with high-order partial derivatives. Early HABCs were written using high-order partial derivatives [110, 177]. In the seminal paper of Engquist and Majda [110], the 0^{th}, 1^{st} and 2^{nd}-order Padé approximations lead respectively to

$$\partial_x u - \imath\kappa u = 0, \quad \text{on } \Gamma, \tag{2.1.5}$$
$$\partial_x u - \imath\kappa u + \frac{1}{2\imath\kappa}\Delta_\Gamma u = 0, \quad \text{on } \Gamma, \tag{2.1.6}$$
$$\Big[1 + \frac{1}{4\kappa^2}\Delta_\Gamma\Big]\partial_x u - \imath\kappa u + \frac{3}{4\imath\kappa}\Delta_\Gamma u = 0, \quad \text{on } \Gamma, \tag{2.1.7}$$

corresponding to $M = 1$, 2 and 3. In fact, the general sequence (2.1.4) leads to

$$\left[\prod_{m=1}^{M} (\partial_x - \imath\kappa\alpha_m)\right] u = 0, \quad \text{on } \Gamma,$$

which is very easy to write, but requires the computation of high-order normal derivatives.

In practice, these formulations are only used at low orders, because the accurate discretization of high-order derivatives may be difficult. The first two conditions, equations (2.1.5) and (2.1.6) are also obtained with the 0^{th} and 1^{st}-order Taylor approximations, while the 2^{st}-order Taylor approximation lead to a condition different than equation (2.1.7). Even if it is obtained with the 1^{st}-order Padé or Taylor approximations, equation (2.1.6) is commonly called *"second-order ABC"* in the literature. Another second-order ABC is obtained by approximating the inverse square root [101],

$$\left[1 - \frac{1}{2\kappa^2}\Delta_\Gamma\right]\partial_x u - \imath\kappa u = 0, \quad \text{on } \Gamma. \tag{2.1.8}$$

Formulations with auxiliary fields defined on the boundary. Formulations with only low-order partial derivatives can be obtained by introducing auxiliary fields and auxiliary equations. This approach was first used by Lindman [214] and then by Renaut [254] and Collino [82, 83] to solve time-domain wave problems with finite differences. Subsequently, similar formulations were proposed for approximations of the square root written as sums of prime fractions [194, A5] or as continued fractions [149, 167, 287, 148, 165, 168, 169, 262], mainly for time-domain problems.

In the Padé case with $M = 2N + 1$ odd, the approximation written as a sum of rationals (2.1.3) lead to the HABC

$$\partial_x u - \imath\kappa u = \frac{2\imath\kappa}{M} \sum_{n=1}^{N} c_n \left(u + \varphi_n\right), \quad \text{on } \Gamma,$$

where $\{\varphi_n\}_{n=1,\dots,N}$ are N auxiliary fields defined only on Γ and governed by

$$-\Delta_\Gamma \varphi_n - \kappa^2 (c_n + 1)(u + \varphi_n) = 0, \quad \text{on } \Gamma, \quad \text{for } n = 1 \dots N.$$

Similarly, the approximation written with the continued fraction (2.1.2) lead to an alternative HABC with M auxiliary fields $\{\phi_m\}_{m=1,\dots,M}$,

$$\begin{aligned} \partial_x u - \imath\kappa u &= \phi_1, && \text{on } \Gamma, \\ \partial_x \phi_m - \imath\kappa \phi_n &= \phi_{m+1}, && \text{on } \Gamma, \quad \text{for } m = 1, \dots, M, \end{aligned} \tag{2.1.9}$$

with $\phi_{M+1} = 0$. With this formulation, the auxiliary equations are coupled in a recursive way, while the auxiliary fields are decoupled with the previous formulation. If M is even, this HABC can also be rewritten with N auxiliary fields $\{\vartheta_n\}_{n=1,\dots,N}$,

$$\begin{aligned} \partial_x u - \imath\kappa u &= \vartheta_1, && \text{on } \Gamma, \\ -\Delta_\Gamma(\vartheta_{n-1} + 2\vartheta_n + \vartheta_{n+1}) - 4\kappa^2 \vartheta_n &= 0, && \text{on } \Gamma, \quad \text{for } n = 1, \dots, N, \end{aligned} \tag{2.1.10}$$

with $\vartheta_{N+1} = 0$, see [167]. Similar formulations can be obtained for the other rational approximations.

Formulations with layers. For specific finite difference schemes [16, 105] and finite element schemes [160, 159, 262], HABCs based on continued fractions can be interpreted as absorbing layers, sometimes called *discrete perfectly matched layers* (DPMLs) by analogy with the PMLs. Note the similarity between the first term of the auxiliary equations (2.1.10) and the central finite difference of a second-order partial derivative. Each auxiliary field then corresponds to an additional layer of the DPML.

With the *double absorbing boundary* (DAB) technique [162, 201], the computational domain is ex-

tended with a layer. The auxiliary equations (2.1.9) are used both at the domain-layer interface and at the exterior boundary. The auxiliary fields $\{\phi_m\}_{m=1,\dots,M}$ are defined inside the layer, where they are governed by the Helmholtz equation. This approach is easy to use, but the auxiliary fields have to be computed in a layer rather than just on the boundary, which increases the computational cost.

2.1.4 Discussions and extensions

Dealing with curved boundaries. Many ABCs have been proposed for circular, elliptic, spherical and spheriodal domains, see e.g. [110, 29, 28, 150, 23, 24, 291, 264, 226]. Some of them have been extended to general convex domains with curved regular boundaries, see e.g. [191, 6, 8, 7, 280]. For example, we have the following ABCs for a general curved surface Γ,

$$\begin{aligned}
&\partial_n u = \imath\kappa u - \mathcal{H} u, && \text{on } \Gamma, && \text{(see e.g. [8])}\\
&\partial_n u = \imath\kappa u - \mathcal{H} u + \frac{1}{2\imath\kappa}(\mathcal{K} - \mathcal{H}^2)u - \frac{1}{2\imath\kappa}\Delta_\Gamma u, && \text{on } \Gamma, && \text{(see e.g. [8])}\\
&\partial_n u = \imath\kappa\sqrt{1 + \Delta_\Gamma/\kappa_\varepsilon^2}\, u, \qquad \text{with } \kappa_\varepsilon = \kappa + \imath\varepsilon \text{ and } \varepsilon > 0, && \text{on } \Gamma, && \text{(see [10])}\\
&\partial_n u = \imath\kappa\sqrt{1 + \Delta_\Gamma/\kappa_\varepsilon^2}\, u - \mathcal{H} u - \operatorname{div}_\Gamma\left(\frac{\mathcal{H}}{2\kappa^2}\nabla_\Gamma u\right), && \text{on } \Gamma, && (2.1.11)
\end{aligned}$$

where $\mathcal{H}$ and $\mathcal{K}$ are the mean and Gaussian curvatures of Γ, respectively. The first two conditions have been obtained by approximating an exact non-reflecting DtN operator for regular curved surfaces [8]. Unfortunately, these ABCs are not accurate for evanescent modes. To deal with evanescent modes, Antoine, Darbas and Lu [10] proposed using Padé-type approximations of the square-root operator with a complex wavenumber, which empirically accounts for curvature effects, and additional terms were suggested in [194]. These approaches lead to the last two conditions above.

Dealing with corners. Planar HABCs can be prescribed on the boundary of polygonal and polyhedral domains, but the direct application of these conditions without corner/edge treatments generates errors.

Corner conditions based on *compatibility relations*, which avoid any error, have been obtained for rectangular and cuboidal domains with right angles. They have been derived for time-dependent problems with a second-order ABC [19], Padé-type HABCs [82, 286, A5], a Higdon-type HABCs [167] and a CRBC [168]. Mathematical analyses of Helmholtz problems with a second-order ABC [190] and a CRBC [164] have been proposed, with corner conditions in both cases. The DPML and DAB techniques can handle corners and edges quite naturally, but this comes at the cost of a larger number of degrees of freedom.

It is difficult to deal with non-right angles. The corner conditions cited above are derived by using the fact that the normal vector at one edge of a rectangular domain is tangent to the adjacent edges. Corner conditions for non-right angles have been studied for the CRBC in [192] and for a second-order ABC [100]. The DPML has been applied to polygonal domains [159], but the error generated at the corners has not been clearly investigated. Alternatively, HABC formulations derived for regular curved boundaries can be prescribed at the boundary of polygonal domains with numerical curvatures to reproduce in a heuristic way any effect related to the corners [6]. The *half-space matching method* (HMM) [48], which is based on an alternative integral representation of the exterior problem, has been extended to truncated domain with non-right angles.

Dealing with other physical waves and media. The extension of HABCs to other physical waves and heterogeneous media is challenging. Padé-type HABCs have been proposed and studied for elastic waves [76, 111, 177, 178, 62, 224] and electromagnetic waves [108]. A first extension with smoothly-varying media has been recently proposed in [221] for time-harmonic acoustic problems. The HMM [48] offers an alternative approach to deal with heterogeneous media.

2.2 Corner treatments for Padé-type HABCs

The contribution is the result of a collaboration with X. Antoine and C. Geuzaine. It corresponds to the article [A9]. I obtained the numerical results by using `GetDP` scripts.

In this contribution, we aim to use Padé-type HABCs for truncated domains with non-regular boundaries. These HABCs are accurate and computationally efficient for planar and regular curved boundaries. However, applying these conditions to the boundaries of polygonal/polyhedral domains without specific corner/edge treatments generates errors.

As explained in Section 2.1.4, exact corner/edge treatments based on compatibility relations have been proposed for HABCs in settings with right angles. The treatment of non-right angles is challenging, regardless of the boundary truncation technique considered. Few corner treatments have been tested and, to the best of our knowledge, only in 2D with polygonal domains.

In [A9], we have proposed and studied two approaches for using Padé-type HABCs with truncated domains having right and non-right angles in 2D and 3D. These approaches are based on compatibility relations and boundary regularization.

2.2.1 Compatibility conditions for corners with right angles

We consider the Helmholtz equation on the quarter space $\Omega = \{(x,y) \in \mathbb{R}^2 : x < 0, y < 0\}$ with a Padé-type HABC with ϕ-rotation of the branch cut on each edge, i.e.

$$\begin{aligned}\partial_x u|_{\Gamma^x} &= \mathcal{L}(u|_{\Gamma^x}, \varphi_1^x, \dots, \varphi_N^x), \quad \text{on } \Gamma^x := \{(x,y) \in \mathbb{R}^2 : x = 0, y < 0\},\\ \partial_y u|_{\Gamma^y} &= \mathcal{L}(u|_{\Gamma^y}, \varphi_1^y, \dots, \varphi_N^y), \quad \text{on } \Gamma^y := \{(x,y) \in \mathbb{R}^2 : x < 0, y = 0\},\end{aligned}$$

with the multivariate function $\mathcal{L}$ defined as

$$\mathcal{L}(w, w_1, \dots, w_N) := \imath\kappa e^{\imath\phi/2}\Big[w + \frac{2}{M}\sum_{i=1}^{N} c_i\,(w + w_i)\Big],$$

where the sets of auxiliary fields $\{\varphi_i^x\}_i$ and $\{\varphi_j^y\}_j$ defined on Γ^x and Γ^y, respectively, are governed by

$$\partial_{yy}\varphi_i^x + \kappa^2\big((e^{\imath\phi}c_i + 1)\,\varphi_i^x + e^{\imath\phi}(c_i + 1)\,u|_{\Gamma^x}\big) = 0, \quad \text{for } i = 1\dots N, \quad \text{on } \Gamma^x, \tag{2.2.1}$$

$$\partial_{xx}\varphi_j^y + \kappa^2\big((e^{\imath\phi}c_j + 1)\,\varphi_j^y + e^{\imath\phi}(c_j + 1)\,u|_{\Gamma^y}\big) = 0, \quad \text{for } j = 1\dots N, \quad \text{on } \Gamma^y, \tag{2.2.2}$$

with $M = 2N + 1$ and $c_i = \tan^2(i\pi/M)$.

From a mathematical point of view, additional boundary conditions have to be prescribed on the auxiliary fields at the corner $P^{xy} = (0,0)$ because of the second-order spatial derivative in equations (2.2.1)-(2.2.2). From a modeling point of view, these additional conditions provide information about the exterior problem. If we are looking for a solution to the free space problem, the corner treatment should accurately represent the outward propagation of waves at the corner.

Our strategy relies on additional compatibility relations that provide the missing boundary conditions at the corners. In a nutshell, these relations are obtained by applying the HABC prescribed at one edge to the auxiliary fields defined at the other edge, and by defining new auxiliary variables at the corner (see justifications in [A9]). After some simplifications, we obtain the additional relations

$$\begin{aligned}\partial_x\varphi_j^y\big|_{P^{xy}} &= \mathcal{L}(\varphi_j^y|_{P^{xy}}, \varphi_{1j}^{xy}, \dots, \varphi_{Nj}^{xy}), \quad \text{for } j = 1\dots N, \quad \text{at } P^{xy},\\ \partial_y\varphi_i^x\big|_{P^{xy}} &= \mathcal{L}(\varphi_i^x|_{P^{xy}}, \varphi_{i1}^{xy}, \dots, \varphi_{iN}^{xy}), \quad \text{for } i = 1\dots N, \quad \text{at } P^{xy},\end{aligned}$$

with N^2 auxiliary variables $\{\varphi_{ij}^{xy}\}_{ij}$ defined at the corner and given by

$$\varphi_{ij}^{xy} = -\frac{(c_j+1)\,\varphi_i^x|_{P^{xy}} + (c_i+1)\,\varphi_j^y|_{P^{xy}}}{c_i+c_j+e^{-\imath\phi}}, \quad \text{for } i,j=1\dots N, \quad \text{at } P^{xy}.$$

The Padé-type HABC and the corner treatment are incorporated quite naturally in the variational form of the Helmholtz problem (2.0.2). Let us consider the Helmholtz equation on a rectangular domain Ω, the HABC on each edge Γ^f (with $f=1\dots4$), and the corner treatment at each corner $P^{fg}=\overline{\Gamma^f}\cap\overline{\Gamma^g}$ (where Γ^f and Γ^g are any adjacent edge). We introduce N auxiliary fields $\{\varphi_i^f\}_i$ on each edge Γ^f, and we define N^2 auxiliary variables $\{\varphi_{ij}^{fg}\}_{ij}$ as

$$\varphi_{ij}^{fg} := -\frac{(c_j+1)\,\varphi_i^f|_{P^{fg}} + (c_i+1)\,\varphi_j^g|_{P^{fg}}}{c_i+c_j+e^{-\imath\phi}}, \quad \text{for } i,j=1\dots N, \quad \text{at each corner } P^{fg}. \tag{2.2.3}$$

The variational formulation of the Helmholtz problem is:

> Find $u\in H^1(\Omega)$ and $\varphi_i^f\in H^1(\Gamma^f)$, with $f=1\dots4$ and $i=1\dots N$, such that
>
> $$\int_\Omega \Big[\nabla u\cdot\nabla v-\kappa^2 uv\Big]d\Omega - \sum_{f=1}^{4}\int_{\Gamma^f}\mathcal{L}\big(u|_{\Gamma^f},\varphi_1^f,\dots,\varphi_N^f\big)v\,d\Gamma = \int_\Omega sv\,d\Omega, \qquad \forall v\in H^1(\Omega),$$
>
> and
>
> $$\int_{\Gamma^f}\Big[\big(\partial_{\tau^f}\varphi_i^f\big)\,\big(\partial_{\tau^f}\rho^f\big) - \kappa^2\big((e^{\imath\phi}c_i+1)\,\varphi_i^f + e^{\imath\phi}(c_i+1)\,u|_{\Gamma^f}\big)\rho^f\Big]\,d\Gamma$$
> $$-\sum_g\Big[\mathcal{L}\big(\varphi_i^f|_{P^{fg}},\varphi_{i1}^{fg},\dots,\varphi_{iN}^{fg}\big)\rho^f\Big] = 0, \qquad \forall\rho^f\in H^1(\Gamma^f),$$
>
> for $f=1\dots4$ and $i=1\dots N$.

In the second equation, the index g corresponds to any edge Γ^g adjacent to Γ^f.

This approach is extended to 3D for cuboidal domains in [A9]. In this case, N 2D auxiliary fields are defined on each face, N^2 1D auxiliary fields are defined on each edge, and N^3 auxiliary variables are defined at the corners. Auxiliary differential equations similar to the 2D and 1D versions of the Helmholtz equation must be solved on the faces and the edges, respectively.

2.2.2 Numerical validation of the compatibility conditions

The compatibility conditions have been validated with 2D and 3D finite element simulations. We have considered the scattering of a plane wave by a disk in a square truncated domain (Figure 2.2a) and by a sphere in a cuboidal truncated domain (Figure 2.3a). These results have been obtained with the mesh generator `Gmsh` [142] and the finite element solver `GetDP` [106]. Repository: `https://gitlab.onelab.info/doc/models/-/tree/master/HelmholtzHABCwithCorners`.

A Padé-type HABC is prescribed on the edges of the square (or on the faces of the cube), and the compatibility relations are used at the corners of the square (or at the edges and corners of the cube). The real part of the error on the numerical solutions (with and without the rotating angle ϕ) compared to the reference free-space analytic solution are shown in Figures 2.2 and 2.3. This error takes into account both modeling errors due to the approximate boundary treatment and numerical errors due to the numerical approximations. With $\phi=0$, surface waves propagate along the artificial boundaries in both cases. In 2D, these spurious waves are canceled with $\phi=\pi/3$, and the numerical error due to the dispersion of the scheme dominates the global error. In 3D, the amplitude of these waves are reduced by taking $\phi=\pi/4$, and they disappear when increasing N from 2 to 3 (results not shown here).

In Figure 2.4, the L^2-norm of the error is plotted as a function of the mesh density for the 2D case

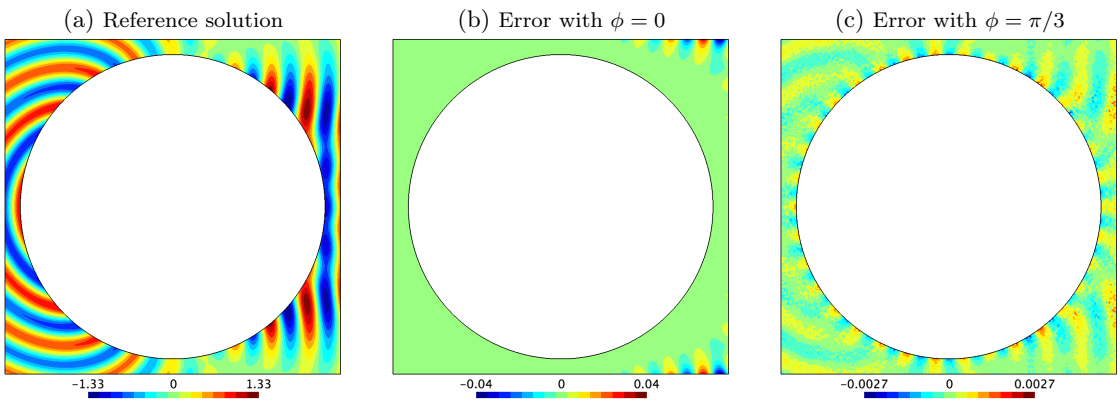

Figure 2.2: Square truncated domain: real part of the reference solution (a) and simulation error with a Padé-type HABC ($N = 4$ and either $\phi = 0$ (b) or $\phi = \pi/3$ (c)) and the corner compatibility conditions. *Parameters: domain* $\Omega = [-1.1, 1.1]^2$*, disk of radius* $R = 1$*, plane wave* $u^{\text{inc}}(\boldsymbol{x}) = e^{\imath\kappa x}$*, boundary condition on the disk* $\partial_n u = -\partial_n u^{\text{inc}}$*, wavenumber* $\kappa = 25$*, second-order curvilinear triangular elements, second-degree polynomial basis functions, mesh density* $n_\lambda \approx 10$. Reproduced from [A9].

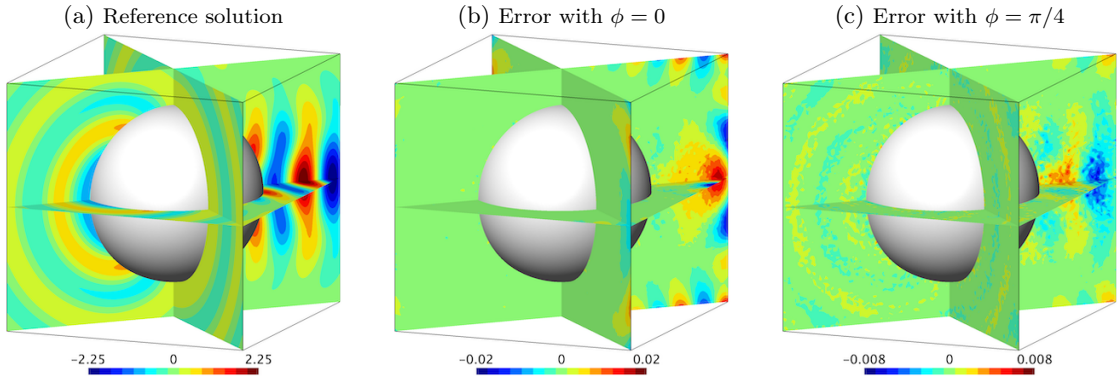

Figure 2.3: Cuboidal truncated domain: real part of the reference solution (a) and simulation error with a Padé-type HABC ($N = 2$ and either $\phi = 0$ (b) or $\phi = \pi/4$ (c)) and the corner/edge compatibility relations. *Parameters: domain* $\Omega = [-1.41, 1.41]^3$*, sphere of radius* $R = 1$*, plane wave* $u^{\text{inc}}(\boldsymbol{x}) = e^{\imath\kappa x}$*, boundary condition on the disk* $\partial_n u = -\partial_n u^{\text{inc}}$*, wavenumber* $\kappa = 10$*, second-order curvilinear triangular elements, second-degree polynomial basis functions, mesh density* $n_\lambda \approx 10$. Reproduced from [A9].

with different values of N and ϕ. The numerical solution is again compared to the reference free-space analytic solution. We also show the projection error between the reference solution and its L^2-projection onto the finite element space. By Céa's lemma, this is the smallest error that can be obtained, regardless of the boundary treatment.

For the coarsest meshes, the smallest error is reached with a few auxiliary fields N, both for $\phi = 0$ and $\phi = \pi/3$, but this error is significantly higher than the projection error. As the mesh is refined, the error decreases until it reaches a plateau, which corresponds to a modeling error due to the approximate boundary treatment. Increasing N decreases the level of the plateau, and using $\phi = \pi/3$ instead of $\phi = 0$ accelerates this decrease. For $N = 5$ and $\phi = \pi/3$, the error is very close to the projection error for the finest meshes. Therefore, the modeling error is negligible compared to the numerical error.

These results confirm the effectiveness of both the Padé-type HABC and the compatibility relations for simulating non-reflecting boundaries with rectangular and cuboidal truncated domains. Using the strategy with the rotating parameter ϕ is critical because it improves the quality of the solution at no additional computational cost. The optimal value of ϕ depends on the case, but $\pi/4$ and $\pi/3$ are frequently used. A numerical investigation is proposed in [A9].

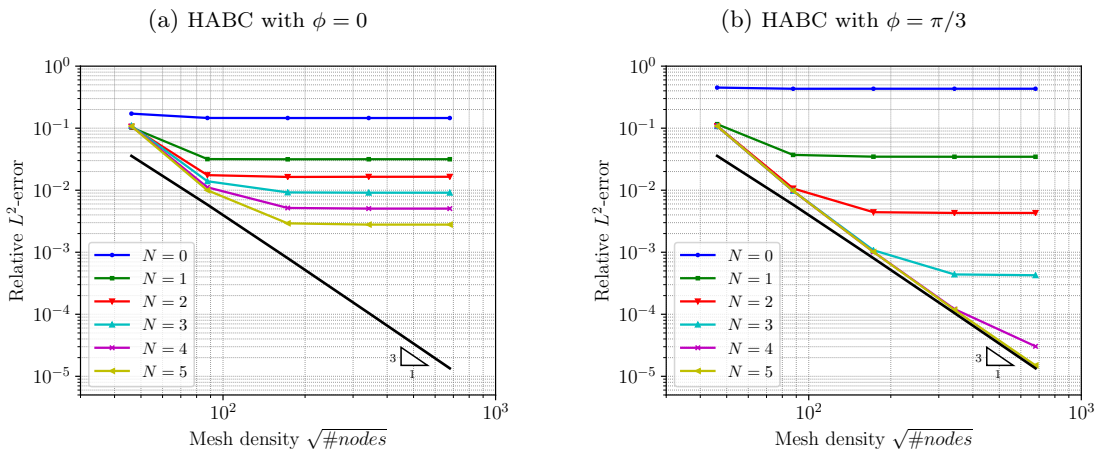

Figure 2.4: Square truncated domain: relative L^2-error as a function of the mesh density. The error takes into account both modeling errors due to the domain truncation and numerical errors due to the scheme. The black line corresponds to the relative projection L^2-error. The mesh density $\sqrt{\#\text{nodes}}$, is computed by using the total number of nodes in the mesh (6 nodes per triangle). Reproduced from [A9].

2.2.3 Approximate treatments for corners with non-right angles

The corner compatibility relations cannot be straightforwardly extended to configurations with non-right angles. Indeed, we used the fact that the normal derivative for one edge is a tangential derivative for the other edge, which does not hold for non-right angles. In [A9], we have tested approximate corner/edge treatments based on approximate conditions and regularization strategies.

To describe the corner treatments, we consider the Helmholtz equation on the infinite wedge domain $\Omega = \{(x, y) \in \mathbb{R}^2 : x^a < 0 \text{ and } y^b < 0\}$, where (x^a, y^a) and (x^b, y^b) are Cartesian coordinates associated with the edges Γ^a and Γ^b, respectively, see Figure 2.5a. The angle between the edges is denoted α. The Padé-type HABC is prescribed on each edge,

$$\begin{aligned} \partial_{x^a} u|_{\Gamma^a} &= \mathcal{L}(u|_{\Gamma^a}, \varphi_1^a, \dots, \varphi_N^a), \quad \text{on } \Gamma^a, \\ \partial_{y^b} u\big|_{\Gamma^b} &= \mathcal{L}(u|_{\Gamma^b}, \varphi_1^b, \dots, \varphi_N^b), \quad \text{on } \Gamma^b, \end{aligned}$$

with auxiliary fields $\{\varphi_i^a\}_i$ and $\{\varphi_j^b\}_j$ defined on Γ^a and Γ^b, respectively, and governed by

$$\begin{aligned} \partial^2_{y^a y^a} \varphi_i^a + \kappa^2 e^{\imath\phi}\big((c_i + e^{-\imath\phi})\, \varphi_i^a + (c_i + 1)\, u|_{\Gamma^a}\big) = 0, \quad \forall i, \quad \text{on } \Gamma^a, \\ \partial^2_{x^b x^b} \varphi_j^b + \kappa^2 e^{\imath\phi}\big((c_j + e^{-\imath\phi})\, \varphi_j^b + (c_j + 1)\, u|_{\Gamma^b}\big) = 0, \quad \forall j, \quad \text{on } \Gamma^b. \end{aligned}$$

We seek a treatment to prescribe at the corner $P = (0, 0)$ for any angle $\alpha \in]0, \pi]$,

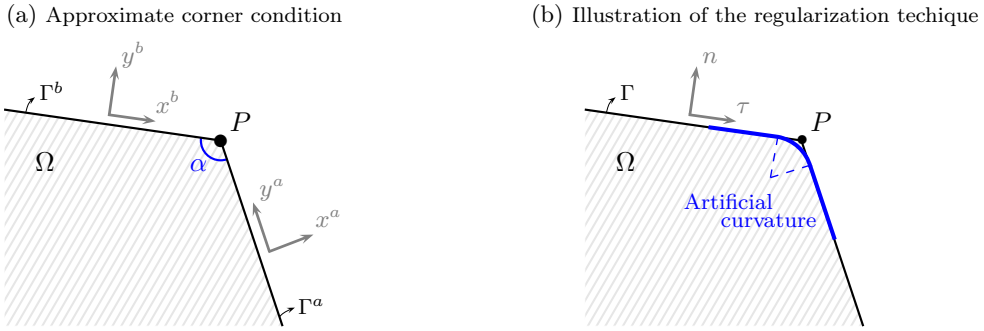

Figure 2.5: Coordinate systems for a corner with a non-right angle. Reproduced from [A9].

Approximate conditions at corners and edges. A first approach consists in applying the compatibility relations derived in the right-angle case to cases where $\alpha \neq \pi/2$, which makes sense if $\alpha \approx \pi/2$. A second approach consists in prescribing the basic ABC on the auxiliary fields, i.e.

$$\partial_{y^a}\varphi_i^a|_P = \imath\kappa\varphi_i^a|_P, \quad \text{for } i = 1\dots N, \quad \text{at } P,$$
$$\partial_{x^b}\varphi_j^b|_P = \imath\kappa\varphi_j^b|_P, \quad \text{for } j = 1\dots N, \quad \text{at } P.$$

This treatment is an approximation, even for $\alpha = \pi/2$, and the computational cost is small. In 3D, when using the HABC on the faces of polyhedral domains, supplementary boundary conditions must be prescribed at the edges for the auxiliary fields belonging to the faces. Similarly to the 2D case, we have tested several approximate conditions for settings with non-right angles [A9].

Treatment by regularization of boundary. Another approach consists in replacing the sharp corners with rounded corners, see Figure 2.5b, avoiding the need for corner conditions. The Padé-type HABC can be used with only one set of auxiliary fields that are continuous at the corner of the original mesh. This is obviously an approximation, which we have called a *hard regularization*.

To improve the treatment, a Padé-type HABC for curved boundaries (e.g. equation (2.1.11) in 3D) can be used with a numerical curvature, which should reproduce in a heuristic way the wave propagation at the corner. This approach is called a *soft regularization*. Selecting a numerical curvature γ_{num} (in 2D) or a numerical mean curvature $\mathcal{H}_{\text{num}}$ (in 3D) is tricky. In our approach, they are obtained by solving auxiliary problems on the boundary of the mesh, denoted with Γ_h, as a pre-processing step. First, the L^2-projection of $\boldsymbol{n}$ onto a finite element space defined on Γ_h is computed. Then, in 2D, the numerical curvature is computed by solving the following variational problem:

$$\left|\begin{array}{l}\text{Find } \gamma_{\text{num}} \in V_{h,\Gamma} \text{ such that} \quad \displaystyle\int_\Gamma (\gamma_{\text{num}} - \boldsymbol{t}\cdot\partial_\tau \boldsymbol{n}_{\text{proj}})\,\psi = 0, \quad \forall \psi \in V_{h,\Gamma},\end{array}\right.$$

where $V_{h,\Gamma}$ is a scalar finite element space on Γ_h. In 3D, the main curvature is computed by solving weakly the formula $2\mathcal{H} = -\nabla\cdot\tilde{\boldsymbol{n}}$, where $\tilde{\boldsymbol{n}}$ is an extension of $\boldsymbol{n}$ in a neighborhood of the surface [127]. The numerical evaluation of curvature and mean curvature is already used for simulations with domains having regular borders, see e.g. [2, 62, 108]. Using this approach for domains having corners was suggested in [6, 7]. However, to the best of our knowledge, the accuracy of the resulting schemes has never been studied. Let us mention that the curvature can also be defined with heuristic formula, see e.g. [7, 59, 220].

2.2.4 Numerical comparison of the approximate corner treatments

The corner treatments have been compared by using several 2D and 3D configurations in [A9]. Selected results are presented below. The benchmark is still the scattering of a plane wave by a disk or a sphere, but the truncated domain is polygonal or polyhedral. The HABC is prescribed on all the edges in 2D (resp. faces in 3D), and the same treatment is used for all the corners (resp. corners and edges).

Snapshots of the error are shown for a triangular domain with different corner treatments in Figure 2.6. In all cases, we observe errors similar to corner waves and grazing waves propagating along the edges. These errors are likely due to the corner treatment, since the error related to the HABC was negligible for a square domain with the same simulation parameters (see Figure 2.2). The error is smaller with the approximate corner conditions than with the regularization techniques.

In Figure 2.8, the relative L^2-error obtained with regular polygonal domains is plotted as a function of α for different corner treatments and two meshes. For the triangle (i.e. $\alpha = \pi/3$), both corner conditions give the smallest relative error. For the square (i.e. $\alpha = \pi/2$), the simulation error is very close to the projection error with the compatibility relations, and it is much larger with the other strategies. As α increases, the error increases with both corner conditions, and it decreases with the regularization techniques. For $\alpha > 2\pi/3$, the best result is always obtained with a soft regularization technique. The

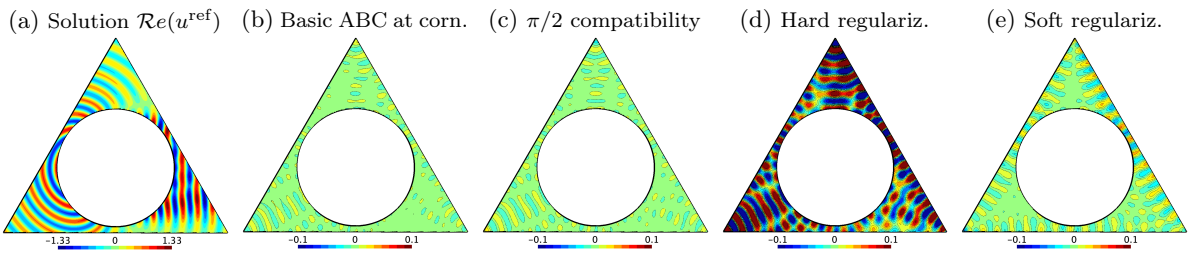

Figure 2.6: Triangular truncated domain: real part of the reference solution (a) and simulation error with a Padé-type HABC ($N = 4$ and $\phi = \pi/3$) and different corner treatments: approximate corner conditions (b)-(c) and regularization techniques (d)-(e). *Parameters: see caption of Figure 2.2.* Note that increasing N does not significantly change the results. Reproduced from [A9].

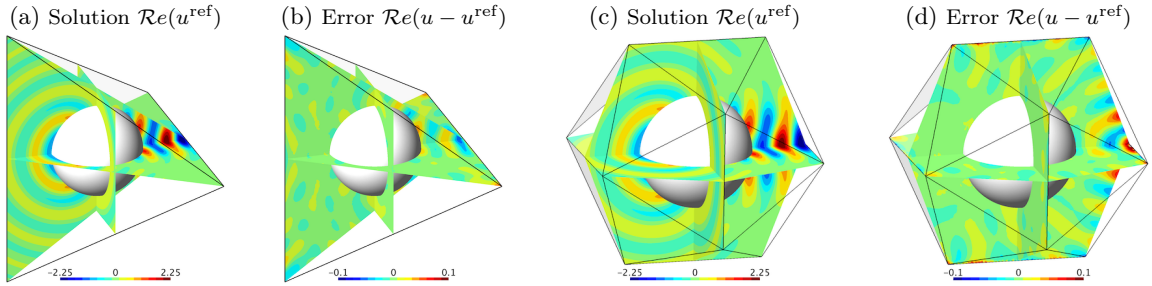

Figure 2.7: Polyhedral truncated domains: reference solution and simulation error with a Padé-type HABC ($N = 2$ and $\phi = \pi/4$) and approximate corner/edge conditions (for the tetrahedron (a)-(b)) or a soft regularization technique (for the icosahedron (c)-(d)). *Parameters: see caption of Figure 2.3.* Reproduced from [A9].

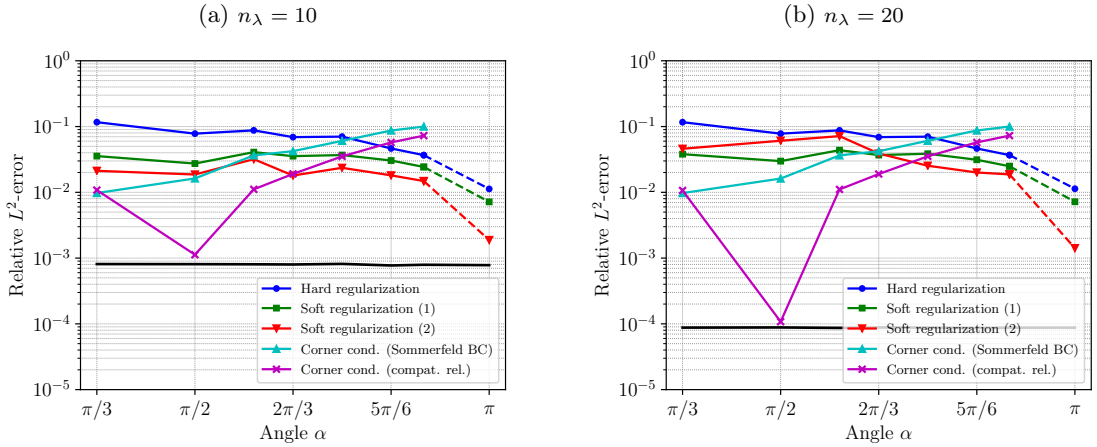

Figure 2.8: Polygonal truncated domains: relative L^2-error as a function of the angle α for different corner treatments and two meshes (numbers of vertices per wavelength $n_\lambda = 10$ or 20). The numerical solution is compared to the free-space analytic solution. For $\alpha = \pi$, the results have been obtained with a circular domain and the exact curvature. The black line corresponds to the relative L^2-projection error. *Parameters: see caption of Figure 2.2, polygonal domains with mid-radius* 1.65*, circular domain with radius* 1.65. Reproduced from [A9].

errors do not vary much when refining the mesh, which confirms that they are due to modeling errors, except for $\alpha = \pi/2$ with the compatibility relations. Similar results have been obtained with a truncated domain corresponding to the slice of a disk, and with regular polyhedra (see illustrations in Figure 2.7).

In summary, approximate corner conditions based on the $\pi/2$ compatibility relations are appropriate for configurations with $\alpha \approx \pi/2$. The soft regularization techniques are the bests for configurations with very obtuse angles. Dealing with angles far from $\pi/2$ and π is challenging, and the error can be only slightly reduced with the considered strategies.

2.3 Overview of PMLs for Helmholtz problems

The *perfectly matched layers* (PMLs) were introduced by Bérenger [38, 39] in the early 90's for solving time-dependent electromagnetic problems with finite differences and truncated rectangular/cubic domains. With Bérenger's approach, the truncated domain is extended by one layer in each Cartesian direction, each equation is split into the Cartesian directions, and directional damping terms are added in the split equations. The resulting PML medium is both *dissipative* and *perfectly matched* to the original medium. Therefore, with accurate discretization schemes, any outgoing wave leaving the truncated domains is perfectly transmitted to the layer, regardless of the angle of incidence, and it is damped inside the layer. This was not possible with the existing layer techniques, see e.g. [189, 181].

Because of its interesting properties, the PML was quickly applied to other physical and geometric configurations. In particular, the technique has found a convenient interpretation for time-harmonic problems: the PML equations are obtained by stretching the spatial coordinates in the complex plane [68, 251, 252]. This approach has been reinterpreted as a modification of the metric tensor [278, 207] and as a modification of the material properties [141, 261, 294]. These interpretations simplify the derivation and implementation of PMLs for truncated domains of general shape.

2.3.1 The Cartesian PML for the Helmholtz equation

We consider the modified Helmholtz problem (2.0.2) with a cuboid truncated domain $\Omega_{\text{dom}} =]-L, L[^3$. The domain is extended in each Cartesian direction by a layer of constant thickness δ_{pml}. The resulting layer is $\Omega_{\text{pml}} :=]-L-\delta_{\text{pml}}, L+\delta_{\text{pml}}[^3 \setminus [-L, L]^3$. The regions of this layer correspond to the faces, edges and corners of the truncated domain. In these regions, the waves must then be damped in one, two and three Cartesian directions, respectively.

Complex coordinate stretch. To derive a PML with a damping in the direction $\boldsymbol{e}_x$, corresponding to the regions with $x \in]-L-\delta_{\text{pml}}, -L[$ and $x \in]L, L+\delta_{\text{pml}}[$, the Helmholtz equation is first rewritten with the local coordinate $\xi_x(x) := L - |x| \in]0, \delta_{\text{pml}}[$. Then, this coordinate is replaced by the *stretched complex coordinate*

$$\tilde{\xi}_x(\xi_x) := \int_0^{\xi_x} s_x(\xi'_x)\, d\xi'_x, \qquad \text{with } s_x(\xi_x) := 1 - \sigma_x(\xi_x)/(\imath\kappa),$$

where $s_x(x)$ is the *stretching function* and $\sigma_x(\xi_x)$ is the *absorption function*. The absorption function is real and positive. The function $\tilde{\xi}_x(\xi_x)$ can be interpreted as a parameterization of a curve in the complex plane. In practice, the PML equation is obtained by replacing ∂_{ξ_x} by $\partial_{\tilde{\xi}_x} = s_x^{-1}\partial_{\xi_x}$, where we have used the chain rule to get back to the real coordinate. This is equivalent to replacing ∂_x with $\partial_{\tilde{x}} = s_x^{-1}\partial_x$.

This strategy is applied in multiple directions within the regions corresponding to the edges and corners of the truncated cuboid domain. For corner PML regions, the gradient operator is then replaced by a complex gradient operator,

$$\nabla_x := \begin{bmatrix}\partial_x & \partial_y & \partial_z\end{bmatrix}^\top \quad \longrightarrow \quad \nabla_{\tilde{x}} = \mathbf{J}_{\text{pml}}^{-1}\nabla_x,$$

where ∇_x is the gradient operator written in Cartesian coordinates, and $\mathbf{J}_{\text{pml}}$ is the Jacobian of the transformation from the Cartesian coordinates (x, y, z) to the stretched Cartesian coordinates $(\tilde{x}, \tilde{y}, \tilde{z})$,

$$\mathbf{J}_{\text{pml}} := \frac{\partial(\tilde{x}_1, \tilde{x}_2, \tilde{x}_3)}{\partial(x_1, x_2, x_3)} = \operatorname{diag}(s_x, s_y, s_z),$$

with the stretching functions $s_x(\xi_x)$, $s_y(\xi_y)$, $s_z(\xi_z)$, and the absorption functions $\sigma_x(\xi_x)$, $\sigma_y(\xi_y)$, $\sigma_z(\xi_z)$ corresponding to the three Cartesian directions. This approach can be interpreted as a change of the metric tensor, where s_x, s_y, s_z are the *scale factors* of the resulting metric tensor [141, 261, 275].

PML equations. Applying the complex coordinate stretches in the Cartesian directions in the Helmholtz equation, we obtain the PML equation

$$-\mathbf{J}_{\text{pml}}^{-1}\nabla_x \cdot (\mathbf{J}_{\text{pml}}^{-1}\nabla_x u) - \kappa^2 u = 0. \tag{2.3.1}$$

This equation can also be written as

$$-\nabla_x \cdot (\mathbf{\Lambda}_{\text{pml}}\nabla_x u) - \alpha_{\text{pml}}\kappa^2 u = 0, \tag{2.3.2}$$

with the complex material parameters

$$\alpha_{\text{pml}} := s_x s_y s_z \quad \text{and} \quad \mathbf{\Lambda}_{\text{pml}} := \text{diag}\left(\frac{s_y s_z}{s_x}, \frac{s_x s_z}{s_y}, \frac{s_x s_y}{s_z}\right).$$

The PML can then be interpreted as a complex anisotropic medium. This formulation is simply equivalent to using complex frequency-dependent anisotropic material parameters. It is very easy to use in practice, as it can be naturally incorporated into existing codes adapted for general material parameters.

Variational formulations. The resulting problem consists of solving the Helmholtz equation in the domain Ω_{dom}, the PML equation in the layer Ω_{pml}, continuity conditions at the interface Γ_{int} and a boundary condition at the exterior border Γ_{ext}. In practice, the homogeneous Neumann condition is often chosen. We introduce the region containing both the domain and the layer, $\Omega := \text{int}(\overline{\Omega_{\text{dom}} \cup \Omega_{\text{pml}}})$. The PML equations (2.3.1) and (2.3.2) lead to the variational formulations

$$\begin{aligned} &\text{Find } u \in H^1(\Omega) \text{ such that, } \forall v \in H^1(\Omega), \\ &\quad \int_{\Omega_{\text{dom}}} \left[\nabla_x u \cdot \nabla_x v - \kappa^2 uv\right] d\Omega \\ &\qquad + \int_{\Omega_{\text{pml}}} \left[(\mathbf{J}_{\text{pml}}^{-\top}\nabla_x u) \cdot (\mathbf{J}_{\text{pml}}^{-\top}\nabla_x v) - \kappa^2 uv\right] (\det \mathbf{J}_{\text{pml}})\, d\Omega = \int_{\Omega_{\text{dom}}} sv\, d\Omega \end{aligned} \tag{2.3.3}$$

and

$$\begin{aligned} &\text{Find } u \in H^1(\Omega) \text{ such that, } \forall v \in H^1(\Omega), \\ &\quad \int_{\Omega_{\text{dom}}} \left[\nabla_x u \cdot \nabla_x v - \kappa^2 uv\right] d\Omega \\ &\qquad + \int_{\Omega_{\text{pml}}} \left[(\mathbf{\Lambda}_{\text{pml}}\nabla_x u) \cdot \nabla_x v - \alpha_{\text{pml}}\, \kappa^2 uv\right] d\Omega = \int_{\Omega_{\text{dom}}} sv\, d\Omega, \end{aligned} \tag{2.3.4}$$

respectively. This first formulation can also be obtained by performing the complex coordinate stretches and the changes of variables directly on the classical sesquilinear form of the Helmholtz equation [225]. It emphasizes the important role of the Jacobian matrix $\mathbf{J}_{\text{pml}}$.

Reflection coefficient. An elementary plane-wave analysis shows that the PML is *perfectly matched*, i.e. any traveling wave is perfectly transmitted from the domain to the layer, regardless of its frequency and angle of incidence. For a PML of finite thickness, plane waves can be reflected by the exterior boundary of the layer, and they can re-enter the domain if they are not sufficiently damped. The *reflection coefficient* R associated with a layer of thickness δ_{pml} is

$$R = \exp\left[-2\cos\theta \int_0^{\delta_{\text{pml}}} \sigma(\xi')\, d\xi'\right], \tag{2.3.5}$$

where θ is the angle of incidence of the plane wave. If σ is unbounded, the reflection coefficient is zero, and the layer is *perfectly absorbing*.

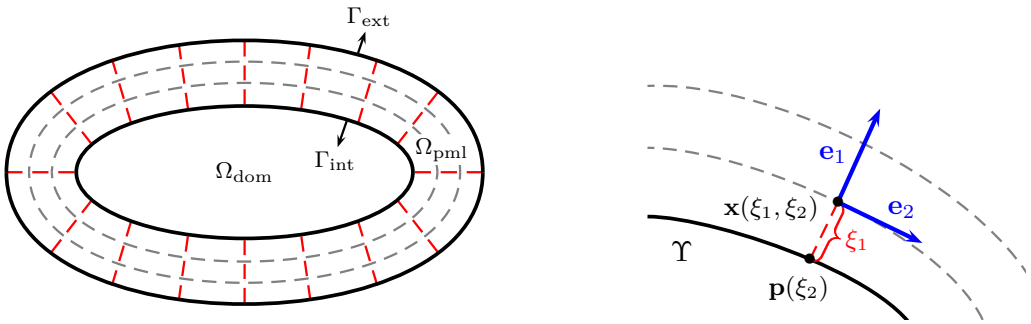

(a) Iso-value coordinate curves

(b) Orthogonal frame

Figure 2.9: Curvilinear coordinates and local frame associated with the boundary Γ_{int} in two dimensions. The curves of iso-value coordinates are represented in figure (a). Gray curves are parallel. Red lines are straight and perpendicular to Γ_{int}. Figure (b) shows the local frame and the radial coordinate ξ_1.

2.3.2 The conformal PML for the Helmholtz equation

The coordinate stretch can be used with other coordinate systems to derive PML formulations for truncated domains of other shapes, such as cylinders, spheres or ellipsoids, see e.g. [57, 86, 277]. However, this technique requires a global coordinate system associated with the interface between the domain and the PML, which can be complicated to use in practice for convex domains with more general shapes.

With the *conformal PML* technique [275, 276], the coordinate stretch is performed in a local curvilinear coordinate system based on surfaces parallel to the interface, see Figure 2.9a. To use this technique, the truncated domain must be convex with a sufficiently regular boundary, and the layer has a constant thickness δ_{pml}. The conformal PML was studied for the Helmholtz equation in [205, 207], and it has been applied to solve time-harmonic problems [109] and time-dependent problems [A11].

Local curvilinear coordinate system. The domain is assumed to be convex, and its boundary is sufficiently regular. Then, each point $\boldsymbol{x}$ of the layer Ω_{pml} can be represented as

$$\boldsymbol{x}(r, \boldsymbol{p}) = \boldsymbol{p} + r\boldsymbol{n}(\boldsymbol{p}), \tag{2.3.6}$$

where $\boldsymbol{p}$ is the closest point belonging to the interface Γ_{int}, $r = \|\boldsymbol{x} - \boldsymbol{p}\| \in]0, \delta_{\text{pml}}[$ is the distance between $\boldsymbol{x}$ and the interface Γ_{int}, and $\boldsymbol{n}(\boldsymbol{p})$ is the unit normal of Γ_{int} at $\boldsymbol{p}$ pointing towards the exterior of Ω_{dom}. The local curvilinear coordinate system (ξ_1, ξ_2, ξ_3) associated to Γ_{int} is defined as follows. For each point $\boldsymbol{x}(\xi_1, \xi_2, \xi_3)$ of the layer, the coordinate $\xi_1 = r$ is the distance function, and the coordinates ξ_2 and ξ_3 are provided by a local parametrization of Γ_{int}. The local parametrization is chosen in such a way that

$$\frac{\partial \boldsymbol{n}}{\partial \xi_i} = \kappa_i \boldsymbol{t}_i, \quad \text{with } \boldsymbol{t}_i = \frac{\partial \boldsymbol{p}}{\partial \xi_i}, \quad \text{for } i = 2, 3,$$

where $\boldsymbol{t}_2(\xi_2, \xi_3)$ and $\boldsymbol{t}_3(\xi_2, \xi_3)$ are the principal directions and $\kappa_2(\xi_2, \xi_3)$ and $\kappa_3(\xi_2, \xi_3)$ are the principal curvatures of the surface Γ_{int} at $\boldsymbol{p}(\xi_2, \xi_3)$, see e.g. [8, A11]. Equation (2.3.6) can then be rewritten as

$$\boldsymbol{x}(\xi_1, \xi_2, \xi_3) = \boldsymbol{p}(\xi_2, \xi_3) + \xi_1 \boldsymbol{n}(\xi_2, \xi_3).$$

The coordinates (ξ_1, ξ_2, ξ_3) form an orthogonal curvilinear coordinate system. The vectors $(\boldsymbol{e}_1, \boldsymbol{e}_2, \boldsymbol{e}_3) := (\boldsymbol{n}, \boldsymbol{t}_2, \boldsymbol{t}_3)$ form an orthonormal frame. The 2D version of this system is illustrated in Figure 2.9b.

Complex coordinate stretch, complex Jacobian matrix and complex material parameters. The PML equation is obtained by writing the Helmholtz equation in the local coordinate system, and then by stretching the real coordinate ξ_1 (i.e. the distance function) into the complex plane. The real

coordinate is replaced with the *stretch complex coordinate*

$$\tilde{\xi}_1(\xi_1) := \xi_1 - \frac{1}{\imath\kappa} f(\xi_1), \quad \text{with } f(\xi_1) := \int_0^{\xi_1} \sigma(\xi_1')\, d\xi_1', \quad \text{for } \xi_1 \in]0, \delta_{\text{pml}}[, \tag{2.3.7}$$

where $\sigma(\xi_1)$ is the *absorption function*.

For the practical implementation in finite element codes, it is convenient to have the PML equation and the variational formulation in Cartesian coordinates. In fact, the problem can be written with the same variational formulations as for the Cartesian case, i.e. equations (2.3.3) and (2.3.4), with the complex Jacobian matrix and the complex material parameters corresponding to the coordinate stretch (2.3.7). The complex Jacobian matrix corresponding to the transformation from the Cartesian coordinates (x_1, x_2, x_3) to the stretched coordinates $(\tilde{x}_1, \tilde{x}_2, \tilde{x}_3)$ can be factorized as

$$\mathbf{J}_{\text{pml}} = \frac{\partial(\tilde{x}_1, \tilde{x}_2, \tilde{x}_3)}{\partial(\tilde{\xi}_1, \tilde{\xi}_2, \tilde{\xi}_3)} \frac{\partial(\tilde{\xi}_1, \tilde{\xi}_2, \tilde{\xi}_3)}{\partial(\xi_1, \xi_2, \xi_3)} \frac{\partial(\xi_1, \xi_2, \xi_3)}{\partial(x_1, x_2, x_3)}.$$

This factorization emphasizes the successive changes of variables: the transformation from Cartesian coordinates to curvilinear coordinates in the complex space, the use of the complex coordinate stretch to come back in the real space, and the transformation from curvilinear coordinates to Cartesian coordinates in the real space. For the specific curvilinear coordinate system described above, we have

$$\mathbf{J}_{\text{pml}} = \mathbf{I} - \frac{1}{\imath\kappa} \left(\sigma(\xi_1)\, \mathbf{n}\mathbf{n}^\top + \frac{\kappa_2}{h_2} f(\xi_1)\, \mathbf{t}_2\mathbf{t}_2^\top + \frac{\kappa_3}{h_3} f(\xi_1)\, \mathbf{t}_3\mathbf{t}_3^\top \right), \tag{2.3.8}$$

where h_1, h_2, h_3 are the *scale factor* of the curvilinear coordinate system,

$$\begin{aligned} h_1 &= 1, \\ h_i &= 1 + \kappa_i(\xi_2, \xi_3)\, \xi_1, \quad \text{for } i = 2, 3, \end{aligned}$$

see e.g. [275, A11, A1]. The corresponding complex material parameters are

$$\begin{aligned} \mathbf{\Lambda}_{\text{pml}} &= (\det \mathbf{J}_{\text{pml}})\, \mathbf{J}_{\text{pml}}^{-1} \mathbf{J}_{\text{pml}}^{-\top}, \\ \alpha_{\text{pml}} &= \det \mathbf{J}_{\text{pml}}, \end{aligned}$$

see e.g. [225]. The complex Jacobian matrix $\mathbf{J}_{\text{pml}}$, and then the complex material parameters $\mathbf{\Lambda}_{\text{pml}}$ and α_{pml}, contain all the information related to the geometry and the complex coordinate stretch. They can be used in the variational formulations (2.3.3) and (2.3.4). If the surface is locally plane, then $\kappa_2 = \kappa_3 = 0$, and the Jacobian matrix of a Cartesian PML with damping in one direction is recovered.

2.3.3 Discussions and extensions

Parameter selection. The accuracy of PMLs depends on the absorption function σ, the thickness δ_{pml} and the spatial discretization. To some extent, increasing the thickness and refining the spatial discretization improve the accuracy. However, this comes at a higher computational cost. The absorption function, which controls the attenuation of waves inside the layer, must be carefully chosen. It should be large enough to sufficiently attenuate outgoing waves. However, it should not introduce a too sharp decay that would not be represented by the discrete scheme, as this would generate numerical reflections. For practical applications, the choice of σ is a critical issue that has been studied e.g. in [43, 71, 87, 173, A8].

Polynomial absorption functions that ensure a progressive damping are frequently used. In particular, the quadratic and cubic functions, i.e.

$$\sigma_{\text{quad}}(\xi) = \bar{\sigma}(\xi/\delta_{\text{pml}})^2 \qquad \text{and} \qquad \sigma_{\text{cub}}(\xi) = \bar{\sigma}(\xi/\delta_{\text{pml}})^3, \tag{2.3.9}$$

are very common choices, although an additional free parameter $\bar{\sigma}$ is introduced. One approach to choose $\bar{\sigma}$ is to set the reflection coefficient for outgoing waves with normal incidence, and then compute the value of the parameter with equation (2.3.5) [87]. For the cubic function, the parameter is $\bar{\sigma} = (2/\delta_{\text{pml}})(\ln R_0^{-1})$, where δ_{pml} and R_0 are given. Nevertheless, $\bar{\sigma}$ should not be too large to prevent any significant numerical reflection [87]. It has been shown in [43, 71, A8] that specific unbounded absorption functions provide high-fidelity solutions without requiring the tuning of parameters. In particular, the hyperbolic and shifted hyperbolic functions

$$\sigma_{\text{hyp}}(\xi) = \frac{1}{\delta_{\text{pml}} - \xi} \qquad \text{and} \qquad \sigma_{\text{sf}}(\xi) = \frac{1}{\delta_{\text{pml}} - \xi} - \frac{1}{\delta_{\text{pml}}} \tag{2.3.10}$$

are effective for finite element simulations. Nevertheless, the numerical approximation requires some care because this function is singular on the exterior border of the layer.

Mathematical analysis. The well-posedness of time-harmonic scattering problems with PML has been studied for several configurations: with a circular PML [42], a Cartesian PML [56, 195] and a conformal PML [206, 207]. Note that these papers make different assumptions about absorption functions.

Dealing with other physical waves. Bérenger's PML was initially introduced for time-dependent simulations of electromagnetic waves [38, 39]. It was then quickly applied and studied for other time-dependent wave equations, such as elastic wave equations [67, 174, 88, 199], Euler's equations [1, 184, 232, 273] and shallow water equations [93, 235]. Many alternative approaches and theoretical studies have been proposed to improve and ensure the stability of the formulations. In particular, anisotropic and dispersive media cause additional difficulties, see e.g. [32, 17, 33, 170] and the references cited in these articles. More general PML formulations have been derived by using a *complex frequency shifted* (CFS) stretch (see e.g. [200, 256, 34]), where both the real and imaginary parts of the coordinates are stretched.

The PML formulations used for time-dependent problems can be directly applied to time-harmonic problems. In fact, the formulations can be simplified for time-harmonic problems. For acoustic and electromagnetic problems, the PML equations can be written with the original equations and complex anisotropic material coefficients [261, 66, 294]. The same approach can be used for elastic problems, but important symmetries of the elastic tensor are lost [225]. Several finite element implementations have been proposed for elastic waves, see e.g. [26, 172, 126]. We refer to [225, 288] for a very useful clarification of the functional framework, and variational formulations suitable for several standard wave models. PML formulations for the convected Helmholtz equation, which is dispersive, have been proposed and studied in [30, 31, 222].

Related approaches. The PML has been implemented in Trefftz finite element method in [185]. The concept of complex scale has been combined with infinite element methods in [180, 230]. In [95], an alternative strategy has been proposed to derive PMLs for time-dependent anisotropic acoustics, and to deal with non-right angles.

2.4 A PML implementation for convex domains of general shape

This contribution is the result of a collaboration with H. Bériot. It corresponds to the article [A1]. The numerical results have been obtained with `MATLAB` and `Simcenter 3D` by H. Bériot.

We have investigated the practical use of the conformal PML for finite element simulations with convex domains of general shape. The conformal PML can be easily implemented with standard finite element methods, but it requires the knowledge of geometric data that may not be available in practice. In 3D, the principal curvatures κ_2, κ_3, the principal directions $\boldsymbol{t}_2$, $\boldsymbol{t}_3$, and the normal $\boldsymbol{n}$ of the interface must be known, as well as the distance r between any point of the layer and the interface, see equation (2.3.8). In addition, for some applications, only polygonal/polyhedral meshed domains are available, while the conformal PML is derived for convex domains with regular boundaries. A typical example is a circular domain meshed with straight-sided elements.

Few PML implementations have been studied for truncated domains of general shape. Zschiedrich et al. [295] proposed a 2D PML implementation for polygonal domains in which the complex coordinate stretch is performed in a local prismatoidal coordinate system. Ozgun and Kuzuoglu [240, 241] proposed a *locally-conformal* PML finite element implementation in which the distance r is estimated by solving a minimization problem, and the coordinate stretch is performed directly on the coordinates of the mesh nodes. This approach is flexible and easy to implement, since it does not require any further geometric data or any modification of the equations, but it involves additional approximations that introduce numerical errors, see [41].

In [A1], we proposed an approach, which we called the *automatically matched layer* (AML) implementation, to deal with convex domains of general shape with regular and non-regular boundaries. For domains with regular boundaries, it is a specific implementation of the conformal PML that requires less geometric data than the original formulation. In the AML approach, the layer is generated by extruding the surface mesh of the domain boundary, and geometric data recorded during the extrusion are extrapolated onto the mesh. The coordinate stretch is embedded into the finite element scheme by a simple modification of the Jacobian matrix in the element-wise integrals.

2.4.1 Description of the AML implementation

We consider the conformal mesh of a convex domain, denoted $\Omega_{\mathrm{dom},h}$. The nature of the elements inside $\Omega_{\mathrm{dom},h}$ does not matter to present our approach. The restriction of these elements on the exterior boundary, denoted $\Gamma_{\mathrm{int},h}$, gives a conformal surface mesh made of linear straight elements ($N_{\mathrm{geo}} = 1$) or quadratic curvilinear elements ($N_{\mathrm{geo}} = 2$), but our approach could be extended to more general elements.

Mesh extrusion and geometric data. The mesh of the layer, denoted $\Omega_{\mathrm{pml},h}$, is generated by extrusion. The vertices and the second-order nodes belonging to the surface mesh $\Gamma_{\mathrm{int},h}$ are extruded in a direction $\mathbf{n}_h$, which should correspond to the exterior normal of $\Gamma_{\mathrm{int},h}$. However, the definition of this normal is ambiguous if the surface is not regular. To define $\mathbf{n}_h$, we have followed empirical rules, which are illustrated in 2D in Figure 2.10. The extrusion is performed N_{pml} times with a constant extrusion distance h_{pml}. The resulting layer is structured and consists of quadrangular elements (in 2D) or prismatic and hexahedral elements (in 3D). The thickness of the layer is $\delta_{\mathrm{pml}} = N_{\mathrm{pml}} h_{\mathrm{pml}}$.

During the mesh extrusion, geometric data are recorded at the extruded nodes. For a node generated at the n^{th} extrusion, the numerical distance r_h is equal to $n h_{\mathrm{pml}}$, the extrusion direction $\mathbf{n}_h$ is the same as for the initial node belonging to the interface, and the closest point $\mathbf{p}_h$ belonging to the interface corresponds to the initial node. The nodal values are then extrapolated on each element by using the finite element shape functions. The distance field obtained using this strategy is illustrated in Figure 2.10.

Let us consider a hexahedral element D^e of the layer. The reference coordinates associated to the reference element $\mathrm{D}_{\mathrm{ref}} = [-1, 1]^3$ are denoted (u_1, u_2, u_3). If the coordinate u_1 is aligned with the

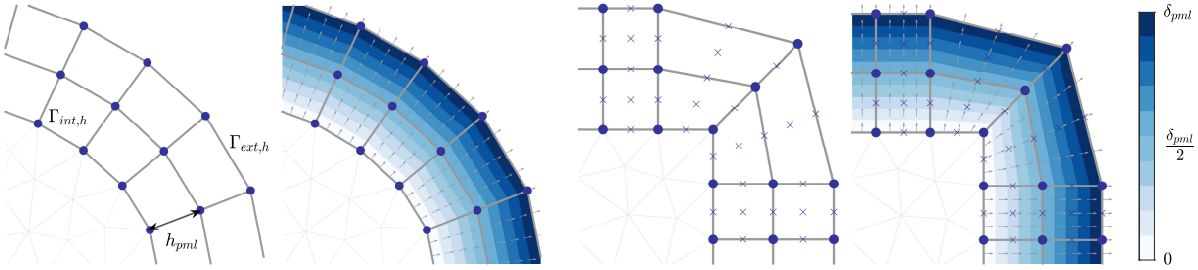

Figure 2.10: Illustration of the mesh extrusion with $N_{\text{pml}} = 2$ for 2D configurations with linear elements *(left)* and quadratic curvilinear elements *(right)*. The mesh vertices and the second-order nodes are shown, as well as the interpolated distance field $r_h \in [0, \delta_{\text{pml}}]$ *(in blue)* and the extrusion directions $\mathbf{n}_h$. Reproduced from [A1].

stretching direction, the position vector can then be written as

$$\mathbf{x}^e(u_1, u_2, u_3) = \mathbf{p}^e(u_2, u_3) + r^e(u_1)\, \mathbf{n}^e(u_2, u_3), \tag{2.4.1}$$

where r^e, $\mathbf{n}^e$ and $\mathbf{p}^e$ are the extrapolated fields.

Local coordinate system and complex coordinate stretch. The complex coordinate stretch is performed in the extrusion direction $\mathbf{n}_h$. In contrast to the continuous case (see Section 2.3.2), the interface $\Gamma_{\text{int},h}$ can be irregular and $\mathbf{n}_h$ is an interpolated field.

On each element D^e of the layer, we define a local coordinate system $(\eta_1^e, \eta_2^e, \eta_3^e)$. The first coordinate is the numerical distance, i.e. $\eta_1^e(u_1) = r^e(u_1)$. The second and third local coordinates are the second and third reference coordinates, i.e. $\eta_2^e(u_2) = u_2$ and $\eta_3^e(u_3) = u_3$, which constitute a local parametrization of $\Gamma_{\text{int},h}$. The coordinate η_1^e is then replaced with $\tilde{\eta}^e(\eta_1^e) := \eta_1^e - f(\eta_1^e)/\imath\kappa$, which is equivalent to replacing $r^e(u_1)$ with $\tilde{r}^e(u_1) = r^e(u_1) - f(r^e(u_1))/\imath\kappa$. The stretched position vector then reads

$$\tilde{\mathbf{x}}^e(u_1, u_2, u_3) := \mathbf{p}^e(u_2, u_3) + \tilde{r}^e(u_1)\, \mathbf{n}^e(u_2, u_3) = \mathbf{x}^e(u_1, u_2, u_3) - \frac{1}{\imath\kappa} f(r^e(u_1))\, \mathbf{n}^e(u_2, u_3). \tag{2.4.2}$$

Thanks to these formulas, we can derive Jacobian matrices to switch between the Cartesian coordinates, the reference coordinates, and the curvilinear coordinates in both real and complex spaces.

Practical computation of the element-wise integrals. The variational formulation (2.3.3) can be used with the Jacobian matrix of the PML transformation, i.e. $\mathbf{J}_{\text{pml}}^e := \partial(\tilde{x}_1^e, \tilde{x}_2^e, \tilde{x}_3^e)/\partial(x_1^e, x_2^e, x_3^e)$, which can be explicitly derived thanks to equations (2.4.1) and (2.4.2). Nevertheless, in practice, the implementation is simplified if $\mathbf{J}_{\text{pml}}^e$ is combined with the Jacobian matrix of the mapping with the reference element, i.e. $\mathbf{J}_{\text{ref}}^e := \partial(x_1^e, x_2^e, x_3^e)/\partial(u_1, u_2, u_3)$.

Let us consider an entry (A, B) of the global matrix of the discrete system obtained with the variational formulation (2.3.3). The element-wise integral corresponding to an element $\mathrm{D}^e \subset \Omega_{\text{pml},h}$ reads

$$\int_{\mathrm{D}^e} \left[([\mathbf{J}_{\text{pml}}^e]^{-\top} \nabla_x \Psi_A) \cdot ([\mathbf{J}_{\text{pml}}^e]^{-\top} \nabla_x \Psi_B) - \kappa^2 \Psi_A \Psi_B \right] (\det \mathbf{J}_{\text{pml}}^e)\, d\mathrm{D}^e,$$

where Ψ_A and Ψ_B are global basis functions. By using the mapping between the physical coordinates (x_1^e, x_2^e, x_3^e) and the reference coordinates (u_1, u_2, u_3), this term can be rewritten as

$$\int_{\mathrm{D}_{\text{ref}}} \left[([\mathbf{J}_{\text{pml}}^e]^{-\top} [\mathbf{J}_{\text{ref}}^e]^{-\top} \nabla_u \psi_a) \cdot ([\mathbf{J}_{\text{pml}}^e]^{-\top} [\mathbf{J}_{\text{ref}}^e]^{-\top} \nabla_u \psi_b) - \kappa^2 \psi_a \psi_b \right] (\det \mathbf{J}_{\text{pml}}^e)\, (\det \mathbf{J}_{\text{ref}}^e)\, d\mathrm{D}_{\text{ref}},$$

where ψ_a and ψ_b are local basis functions defined on D_{ref}, $\nabla_u = [\partial_{u_1}\ \partial_{u_2}\ \partial_{u_3}]^\top$ is the gradient in the reference coordinate system, and a and b are the local indices associated to the global indices A and B.

Combining the Jacobian matrices gives

$$\int_{\mathrm{D}_{\mathrm{ref}}} \left[([\mathbf{J}^e]^{-\top} \nabla_u \psi_a) \cdot ([\mathbf{J}^e]^{-\top} \nabla_u \psi_b) - \kappa^2 \psi_a \psi_b \right] (\det \mathbf{J}^e)\, d\mathrm{D}_{\mathrm{ref}}$$

with the combined Jacobian matrix $\mathbf{J}^e$ that can be written as

$$\mathbf{J}^e := \mathbf{J}^e_{\mathrm{pml}} \mathbf{J}^e_{\mathrm{ref}} = \frac{\partial(\tilde{x}_1^e, \tilde{x}_2^e, \tilde{x}_3^e)}{\partial(u_1, u_2, u_3)} = \mathbf{J}^e_{\mathrm{ref}} - \frac{1}{\imath\kappa} \begin{bmatrix} (\partial_{u_1} r^e)\, \sigma(r^e)\, \mathbf{n}^e & f(r^e)\, \partial_{u_2} \mathbf{n}^e & f(r^e)\, \partial_{u_3} \mathbf{n}^e \end{bmatrix}, \quad (2.4.3)$$

thanks equation (2.4.2).

In a nutshell, the AML implementation consists of adding an imaginary part to the Jacobian matrix used in the element-wise integrals, see equation (2.4.3). It requires only a distance function $r^e(u_1)$ and an extrusion direction $\mathbf{n}^e(u_2, u_3)$, which are obtained by extrapolating nodal values on the mesh.

Discussion and comparison. If the interface is smooth, the AML implementation can be seen as a conformal PML with approximate geometric parameters. Indeed, if $\mathbf{n}^e$ is an accurate approximation of $\mathbf{n}$, then the matrix (2.4.3) is recovered by combining the matrix (2.3.8) of the conformal PML transformation and the Jacobian matrix $\mathbf{J}^e_{\mathrm{ref}}$ associated to the mapping with the reference element. For non-smooth interfaces, the AML is an approximate conformal PML with empirical parameters.

The LC-PML implementation proposed by Ozgun and Kuzuoglu in [240, 241] consists in replacing the coordinates of the mesh nodes with the stretched coordinates, which leads to the Jacobian matrix

$$\mathbf{J}^e = \begin{bmatrix} \partial_{u_1} \tilde{\mathbf{x}}^e & \partial_{u_2} \tilde{\mathbf{x}}^e & \partial_{u_3} \tilde{\mathbf{x}}^e \end{bmatrix}, \quad (2.4.4)$$

where $\tilde{\mathbf{x}}^e$ is a polynomial representation of the stretched coordinates. In fact, the real part of this matrix is identical with the AML (i.e. with equation (2.4.3)), but the imaginary part is different. The LC-PML approach is a priori simpler, but it involves additional numerical approximations. Indeed, the stretched coordinates are interpolated with polynomial shape functions, and the resulting functions are differentiated numerically in equation (2.4.4). By contrast, with the AML, the absorbing function $\sigma(r^e)$ and the integrated function $f(r^e)$ are evaluated exactly in the Jacobian matrix without any polynomial interpolation and numerical differentiation.

Unbounded absorbing functions, such as the hyperbolic function σ_{hyp} (2.3.10), can be used efficiently with the AML, while local instabilities can appear with the LC-PML, see [41]. In our numerical results, we have used σ_{hyp} with the Gauss-Legendre quadrature without any difficulty, despite the singularity of σ_{hyp} at the exterior boundary of the layer.

Strategies to address non-right angles have been proposed for absorbing layers that are defined differently [160, 159, 95]. Nevertheless, these strategies do not apply to standard PML formulations, and they involve specific modifications of the computational scheme at the corners. By contrast, the implementations considered here correspond to the standard PML on the regular parts of the domain boundary, with a corner treatment implicitly embedded in the coordinate stretch based on the mesh extrusion.

2.4.2 Numerical results: validation, comparison and illustration

The AML implementation has been compared to the direct implementation of the conformal PML, and to the LC-PML implementation. Selected representative 2D results and a 3D illustration with a commercial code are presented below, see [A1] for more results.

The reference benchmark corresponds to the scattering of a plane wave by a sound-hard disk. The solutions obtained with circular and pentagonal truncated domains are shown in Figure 2.11. The default parameters are written in the caption of the figure. The domain is meshed with `Gmsh` [142], and the layer is generated by extrusion at run time by the solver, which is a `MATLAB` code.

In preliminary comparisons (not shown), we have observed that the performance of the hyperbolic

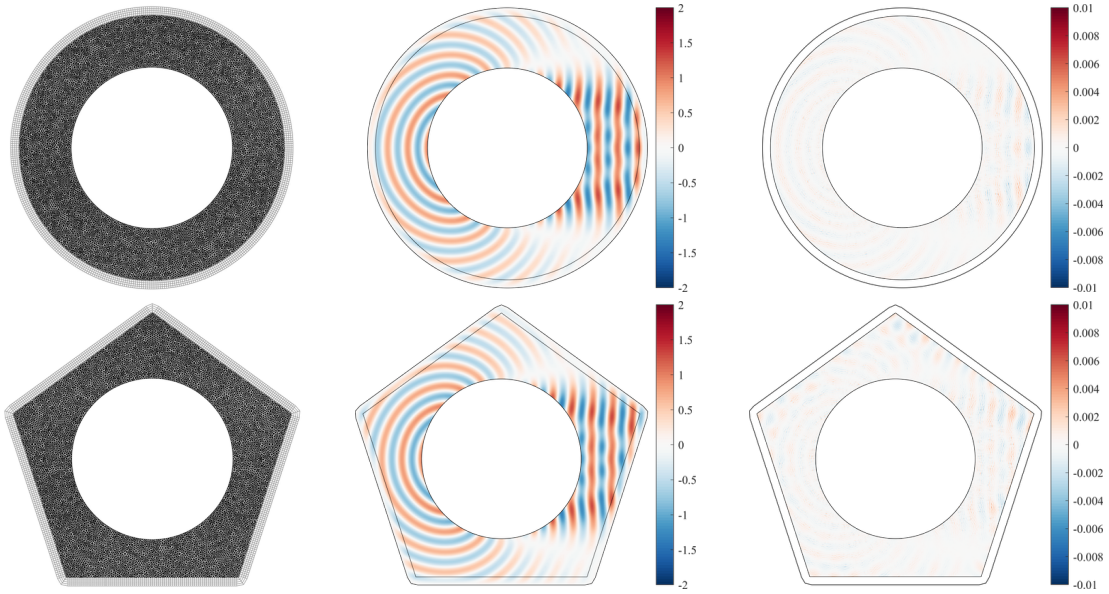

Figure 2.11: Circular/pentagonal truncated domain: mesh *(left)*, real part of the numerical solution *(center)* and error distribution *(right)* obtained with the AML implementation. *Parameters: circular domain of radius* 1.65*, pentagonal domain of midradius* 1.65*, scattering disk of radius* 1*, wavenumber* $\kappa = 25$*, plane wave* $u_{\text{inc}}(\boldsymbol{x}) = e^{\imath\kappa x}$*,* $\partial_n u = -\partial_n u_{\text{inc}}$ *on* Γ_{sca}*,* $\partial_n u = 0$ *on* Γ_{ext}*, second-order curvilinear triangles in* Ω_{dom}*, second-order curvilinear quadrangles in* Ω_{pml}*, second-order polynomial basis functions, characteristic size of a mesh cell* $h \approx 1/25$*, number of extrusions* $N_{\text{pml}} = 4$*, layer thickness* $\delta_{\text{pml}} = N_{\text{pml}} h$*, hyperbolic absorbing function* σ_{hyp}. Reproduced from [A1].

function σ_{hyp} (2.3.10) and the cubic function σ_{cub} (2.3.9) for layers with several cells is similar if the parameter $\bar{\sigma}$ of σ_{cub} is well-chosen. The function σ_{cub} is slightly outperformed by σ_{hyp} for layers with one or two mesh cells. It is rather clear that using σ_{hyp} is advantageous, especially for small layers. Here, σ_{cub} is used with the empirical rule $\bar{\sigma} = (2/\delta)(\ln R_0^{-1})$ and $R_0 = 10^{-6}$.

Cases with a circular domain. The scattering disk of radius 1 is placed in the center of a circular truncated domain of radius 1.1. Figure 2.12 shows the relative L^2-error as a function of the numbers of extrusions N_{pml}, for polynomial shape functions with the degrees $p = 1$, 2 and 3, and both functions σ_{hyp} and σ_{cub}. The numerical solution u_{num} is compared to the reference free-space analytic solution u_{ref} inside the truncated domain.

The AML implementation and the direct implementation of the conformal PML give identical results in all the cases, which is expected for truncated domains with regular boundaries. The LC-PML implementation did not give satisfactory results with σ_{hyp} (i.e. the solution blows up, results not shown). It can be used with σ_{cub}, but, for thin layers, the errors are always smaller with the AML (Figure 2.12b). Recall that the LC-PML approach introduces approximation errors due to the interpolation of complex coordinates on the finite element mesh.

Cases with polygonal domains. The scattering disk of radius 1 is placed in the middle of polygonal domains of midradius 1.65, and in the middle of a circular domain of radius 1.65, see Figure 2.11. Figure 2.13 shows the relative L^2-error as a function of N_{pml} obtained with the AML implementation (with σ_{hyp}) and the LC-PML implementation (with σ_{cub} and $R_0 = 10^{-6}$). As a reference, the Cartesian PML is tested with both absorbing functions for the configurations with the square domain. The relative projection error has nearly the same value for all the computational domains.

Both AML and LC-PML implementation are equivalent for thick layers, i.e. with $N_{\text{pml}} \geq 5$. The results are satisfactory, except for the triangular case, where the angles are acute. For thin layers, which allow for a reduction of the computational cost, combining the AML with σ_{hyp} is the most efficient approach. The 3D results discussed in [A1] lead to a similar conclusion.

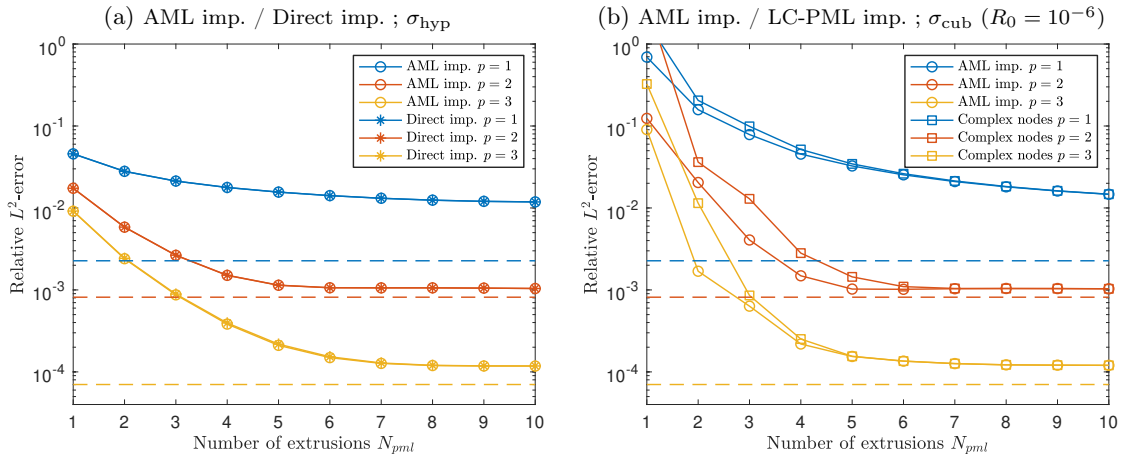

Figure 2.12: Circular truncated domain: L^2-error in the truncated domain as a function of N_{pml} with different PML implementations and two absorbing functions. The LC-PML did not give satisfactory results with σ_{hyp}. The results of the AML and the direct implementation of the conformal PML were identical with σ_{cub}. The dashed lines correspond to the best interpolation error. *Parameters: wavenumber* $\kappa = 25$, *characteristic size of the mesh cells* $h = p\lambda/d_\lambda$, *wavelength* $\lambda = 2\pi/\kappa$, *resolution rate* $d_\lambda = 20$. Reproduced from [A1].

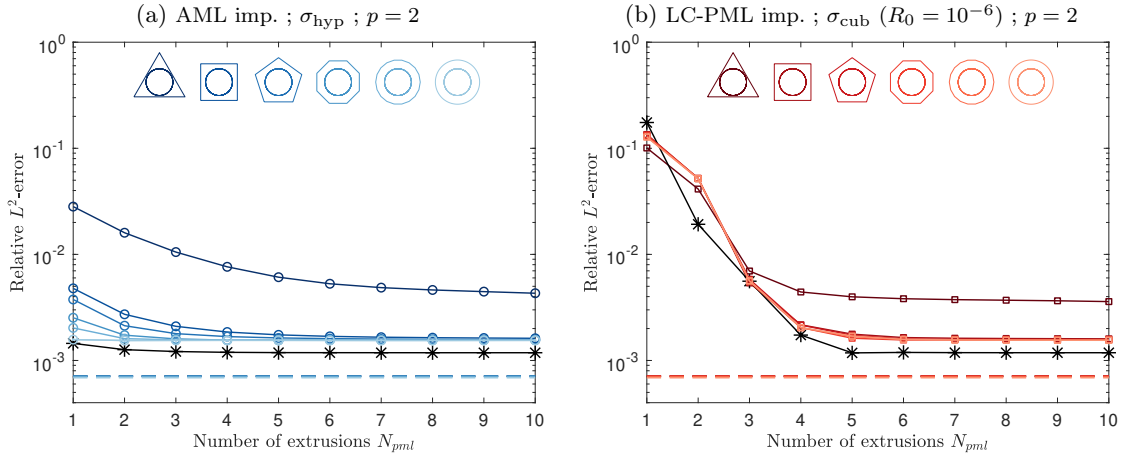

Figure 2.13: Polygonal truncated domain: L^2-error in the truncated domain as a function of N_{pml} with the AML equipped with σ_{hyp} *(left)* and the LC-PML equipped with σ_{cub} *(right)*. Light and dark colors correspond to polygonal domains with many and few edges, respectively. The black lines correspond to the results with the standard Cartesian PML for the square domain. The dashed lines correspond to the best interpolation error. *Parameters: wavenumber* $\kappa = 25$, *polynomial degree* $p = 2$, *resolution rate* $d_\lambda = 20$. Reproduced from [A1].

Illustration of application. To illustrate the interest of the AML for 3D realistic cases, we consider the scattering of a plane wave by a *shark* submarine (Figure 2.14a). To minimize the number of degrees of freedom, the exterior surface of the truncated domain is automatically generated by using a convex hull algorithm based on [20] (Figure 2.14b). Then, the mesh of this surface is extruded to generate the layer. The final model was set up and run by H. Bériot (Siemens, Belgium) using the simulation package `Simcenter 3D` [266] developed by Siemens Industry Software.

The numerical solution obtained with $N_{\text{pml}} = 5$ is shown in Figure 2.14c. To study the influence of the PML on the accuracy, the directivity of the scattered field on a circle of radius 2 in the xz-plane is shown in Figure 2.14d for $N_{\text{pml}} = 1$, 5 and 10. The results obtained with the different thicknesses are very close. A thin absorbing layer, with a thickness of only few mesh cells, is sufficient to get accurate results, although the interface between the domain and the layer is very close to the submarine.

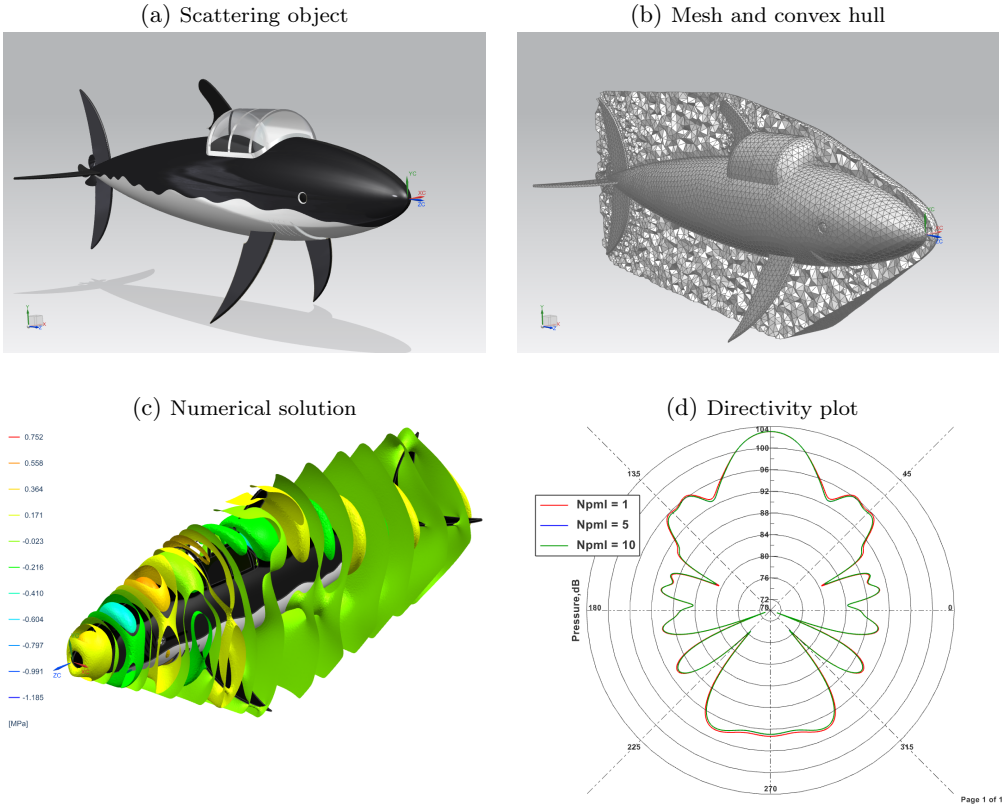

Figure 2.14: Illustration of application: (a) original CAD model of unit length; (b) mesh and convex exterior surface generated at the minimal distance $2h$ from the submarine; (c) real part of the scattered field; (d) directivity plot of the scattered field on a circle or radius $a = 2$, in the zx-plane, centered at $z = 0.5a$, with several thicknesses of PML. *Parameters: incidence vector* $\boldsymbol{\kappa}_{inc} = [0, 0, -1]^\top$, *wavenumber* $\kappa = 40$, *characteristic length* $h = 15{\times}10^{-3}$, *quadratic elements, polynomial degree* $p = 2$, *resolution rate* $d_\lambda = 20$. Reproduced from [A1].

Table 2.1: Illustration of application: characteristics for truncated domains with different shapes. The distance between the interface and the submarine is equal to $2h$ and an extruded layer with $N_{\text{pml}} = 5$ is generated.

Shape of domain	Volume of domain	# Elements		# DoFs			Memory for facto.
		Domain	Ext. layer	Domain	Ext. layer	Total	
Convex envelope	$6.8e^{-2}$	302 803	109 670	439 884	438 700	878 584	11.6 Gb
Cuboid	$19.7e^{-2}$	546 837	151 020	773 064	604 100	1 377 164	23.5 Gb
Cylinder	$21.1e^{-2}$	608 502	146 140	854 097	584 580	1 438 677	28.3 Gb

In the solution process, the most computationally intensive operation was solving the linear discrete system, which was done with a LU factorization. The computational cost, in terms of runtime and memory storage, is directly related to the total number of degrees of freedom, and then to the volume of the domain. Using the convex hull algorithm to define the domain, instead of a more standard geometry, reduces the size of the domain. To illustrate this, we have generated cuboidal and cylindrical domains that are aligned with the main axis of the submarine. For each geometry, the minimal distance between the exterior boundary and the submarine is equal to $2h$, and the exterior surface mesh is extruded to generate a layer with $N_{\text{pml}} = 5$. The characteristics of the resulting models are compiled in Table 2.1.

The use of a convex envelope allows to reduce the size of the resulting global system by about 40% as compared to a canonical truncation. This results in a significant memory footprint reduction of 60% (resp. 50%) compared to the cylindrical (resp. cuboidal) case. It is important to limit the volume of the domain and the thickness of the layer to control the computational cost, especially in 3D. This advocates using the AML with an efficient unbounded absorbing functions, such as the hyperbolic one.

Chapter 3

Domain decomposition methods

In this chapter, we aim to accelerate the iterative solution of time-harmonic problems discretized with finite elements by using *domain decomposition methods* (DDMs). This family of methods actually covers a wide range of computational strategies. They are all based on a partition of the computational domain into subdomains, and the definition of local problems on these subdomains. These local problems are solved at each step of a global iterative process, and the local solutions are used in one way or another to speed up the convergence of the process.

This research topic is very active and benefits from a large community. Most of the methods proposed for elliptic problems have been studied mainly for coercive problems. Unfortunately, the classical methods do not work so well for time-harmonic problems, which are generally indefinite, and tailored approaches are required, see e.g. [117, 138]. For example, the convergence of the global iterative process can be accelerated by using transmission conditions based on domain truncation techniques at the interfaces between the subdomains, which improves the representation of the waves propagating across these interfaces. In sweeping preconditioners, the local problems are solved in a certain order to *sweep* the partition, which mimics the wave propagation in the global domain. Several other approaches are described below.

I have contributed to non-overlapping DDMs with transmission conditions based on HABC and PML for checkerboard domain partitions. These domain partitions have *cross-points*, which are points shared by more than two subdomains, or points shared by at least two subdomains and belonging to the exterior boundary of the computation domains. If the presence of cross-points is not taken into account in the construction of a DDM, the efficiency of this method can be reduced and, in the worst cases, it can even converge to a wrong solution.

This chapter is structured as follows. After a brief review of standard and current approaches (Section 3.1), three contributions are presented: two substructuring methods with HABC and PML transmission for checkerboard domain partitions (Sections 3.2 and 3.3, respectively), and a family of sweeping preconditioners adapted to these partitions (Section 3.4).

3.1 Overview of DDMs for Helmholtz problems

In this section, we briefly present and review of *domain decomposition domains* (DDMs) that have been applied or specifically developed for time-harmonic problems discretized with finite elements. For general presentations of DDMs for finite element solvers, see e.g. the reference books [250, 285, 223, 244, 103] and the review article [154]. The parallel solution of time-harmonic problems is discussed in more detail e.g. in [223, chapter 18], [103, chapter 2] and [202]. We also refer to the recent reviews [138, 139].

To describe the methods, we consider the Helmholtz equation on a 2D computational domain Ω with an ABC on the exterior boundary $\Gamma_{\text{ext}} := \partial\Omega$. The problem reads:

$$\left|\begin{array}{l} \text{Find } u \in H^1(\Omega) \text{ such that} \\ \quad \begin{cases} -\Delta u - \kappa^2 u = s, & \text{in } \Omega, \\ \partial_n u - \imath\kappa u = 0, & \text{on } \Gamma_{\text{ext}}, \end{cases} \end{array}\right. \tag{3.1.1}$$

with a strictly positive wavenumber $\kappa(\boldsymbol{x})$, the exterior normal derivative ∂_n, and a source term $s(\boldsymbol{x})$.

3.1.1 A first convergent domain decomposition algorithm

In the early 90', Després [97, 99, 35] proposed a non-overlapping domain decomposition algorithm for the finite element solution of Helmholtz problems. This algorithm was adapted from the non-overlapping Schwarz algorithm studied shortly before by Lions [215] for Laplace and coercive problems. It this method, the local problems are coupled with Robin (or impedance) transmission conditions. Després [97] proved that the iterative process is convergent for Helmholtz problems with specific impedance coefficients.

We consider a partition of the domain Ω into *non-overlapping subdomains* $\{\Omega_I\}_{I=1\dots N_{\text{dom}}}$. We have $\overline{\Omega} = \cup_I \overline{\Omega_I}$ and $\Omega_I \cap \Omega_J = \emptyset$ if $I \neq J$. The *exterior boundary* of a subdomain Ω_I is denoted by $\Gamma_{\text{ext},I} := \partial\Omega_I \cap \Gamma_{\text{ext}}$. The *interface* with a neighboring subdomain Ω_J is denoted by $\Gamma_{IJ} := \partial\Omega_I \cap \partial\Omega_J$.

The iterative process starts with an initial local solution u_I^0 on each Ω_I. Then, at each step $\ell \geq 0$, an updated local solution $u_I^{\ell+1}$ is computed on each Ω_I by solving

$$\left|\begin{array}{l} \text{Find } u_I^{\ell+1} \in H^1(\Omega_I) \text{ such that} \\ \quad \begin{cases} -\Delta u_I^{\ell+1} - \kappa^2 u_I^{\ell+1} = s, & \text{in } \Omega_I, \\ \partial_{n_I} u_I^{\ell+1} - \imath\kappa u_I^{\ell+1} = 0, & \text{on } \Gamma_{\text{ext},I}, \\ \partial_{n_I} u_I^{\ell+1} - \imath\kappa u_I^{\ell+1} = g_{IJ}^{\ell}, & \text{on each } \Gamma_{IJ}, \end{cases} \end{array}\right. \tag{3.1.2}$$

with the exterior normal derivative ∂_{n_I} and the transmission variable g_{IJ}^{ℓ} defined as

$$g_{IJ}^{\ell} := \partial_{n_I} u_J^{\ell} - \imath\kappa u_J^{\ell},$$

where u_J is the local solution associated to the neighboring subdomain Ω_J. The transmission variable g_{IJ}^{ℓ} can be interpreted as information transferred from Ω_J to Ω_I. Note that $\Gamma_{IJ} = \Gamma_{JI}$, $\partial_{n_I} = -\partial_{n_J}$ and $g_{IJ}^{\ell} \neq g_{JI}^{\ell}$. Since a local problem similar to system (3.1.2) is defined on Ω_J, we have the transmission condition $\partial_{n_J} u_J^{\ell} - \imath\kappa u_J^{\ell} = g_{JI}^{\ell-1}$ on Γ_{IJ}. Combining this condition with the definition of g_{IJ}^{ℓ} gives

$$g_{IJ}^{\ell} = -g_{JI}^{\ell-1} - 2\imath\kappa u_J^{\ell-1}.$$

This formula is convenient for updating the transmission variables because it does not require the Neumann trace of the local solution, which can be difficult to obtain in practice in finite element schemes.

3.1.2 Substructuring techniques

The reduced problem. The non-overlapping domain decomposition algorithm of Després [97] can be rewritten in a compact form, which is useful for studying or proposing DDMs. Let us recast all the transmission variables in the *set of all transmission variables* $g^\ell \in \mathcal{G}$. By using the linearity of the problem and eliminating the local solutions from the algorithm, the global process can be rewritten as

$$g^{\ell+1} = \mathrm{T} g^\ell + b \tag{3.1.3}$$

where $\mathrm{T} : \mathcal{G} \to \mathcal{G}$ is an iteration operator and $b \in \mathcal{G}$ depends on the source term s. This process can be seen as a fixed-point iteration applied to linear system

$$\mathrm{F} g := (\mathrm{I} - \mathrm{T}) g = b, \tag{3.1.4}$$

which is called the *substructured problem*, the *interface problem* or the *reduced problem*. This problem can be solved with Krylov-type iterations instead of the fixed-point iteration, and preconditioning techniques can be used to speed up the iterative process.

The operator T can be rewritten as the successive application of a *scattering operator* S and an *exchange operator* Π [99, 84], i.e. $\mathrm{T} = \Pi\mathrm{S}$. The operator S acts as an *"incoming to outgoing"* operator for each subdomain. It requires the solution of the local problem with *incoming* transmission variables, and it computes *outgoing* data to send to the neighboring subdomains. The operator Π exchanges the data at the interfaces between the subdomains. The problem then reads

$$(\mathrm{I} - \Pi\mathrm{S}) g = b, \tag{3.1.5}$$

with the identity operator I.

Transmission conditions based on domain truncation techniques. The convergence of the non-overlapping DDMs strongly depends on the transmission conditions enforced at the interfaces between the subdomains. In the local problem (3.1.2), the transmission conditions can be replaced with

$$\partial_{n_I} u_I^{\ell+1} - \mathcal{T}_{IJ} u_I^{\ell+1} = g_{IJ}^\ell, \qquad \text{on each } \Gamma_{IJ},$$

where $\mathcal{T}_{IJ}$ is a *transmission operator*. The optimal operator corresponds to the non-local Dirichlet-to-Neumann (DtN) map related to the complement of each subdomain, which is a Schur complement at the discrete level. Since the computation of the exact DtN is prohibitive, strategies based on approximate DtN operators started to be investigated in the late 80's and early 90's, see e.g. [166, 234]. This question is closely related to the development of domain truncation techniques, where boundary operators are used to represent the outward propagation of waves. Here, transmission operators should represent the transmission of waves at the interfaces.

The transmission operator corresponds to the basic ABC operator in [97] and to the standard 2^{nd} order ABC operator in [249]: $\mathcal{T} u = \imath\kappa u$ and $\mathcal{T} u = \imath\kappa u - \Delta_\Gamma u/(2\imath\kappa)$. General 0^{th} and 2^{nd} order operators with optimized parameters were proposed in [135]: $\mathcal{T} u = \alpha u$ and $\mathcal{T} u = \alpha u + \beta\Delta_\Gamma u$. Two-sided transmission conditions were studied in [132]. More sophisticated transmission conditions are based on HABC operators [52, 54, 196], PML operators [263, 270, 289] and integral operators [84, 272, 209, 208, 85]. These operators speed up the convergence of the iterative process (up to a certain point) with an extra cost per iteration. The cost is related to the order of the HABC, the thickness of the PML, and the kind of the integral operator. Note that the interfaces between the subdomains must be regular to use these approaches, and the cross-points require some care, see below. For a more detailed review of DDMs with domain truncation techniques, we refer to the survey of Gander and Zhang [139].

Cross-point issues and strategies. Most of the DDMs with 2^{nd} order, HABC, PML and non-local operators were initially studied and tested for configurations with 1D domain partitions, such as partitions

in layers or in onion skins. Such partitions do not have *interior cross-points*, which are points where more than two subdomains meet. However, for large 2D and 3D applications, the amount of data to be transferred can be much smaller with multidimensional partitions, such as Cartesian and checkerboard partitions, or general mesh partitions with irregular interfaces. For such partitions, the interior cross-points may require some care at the continuous level, the discrete level, at both. Additional difficulties arise when a HABC, a PML or an integral equation is prescribed on the exterior boundary of the global domain. In these cases, the *boundary cross-points* that belong to both the exterior boundary and two subdomains also require some care.

The convergence of the iterative process (3.1.3) with the transmission operator $\mathcal{T} = \imath\kappa$ has been proved at the continuous level for a general domain partition, possibly with cross-points, see [97]. The method works perfectly after discretization with a mixed finite element method, but the direct discretization of the reduced system with a nodal finite element method leads to an underdetermined problem. In fact, the discrete equations associated to the interior cross-points are linearly dependent. This issue is not limited to Helmholtz problems, see e.g. [250, 285, 103], and can be treated in different ways. The reduced system can be solved with a preconditioned Krylov-type methods, which can solve underdetermined system. This approach is used in the FETI [94] and FETI-H [120, 121] methods[1]. In the FETI-DPH method [118], a global problem is associated to the discrete physical unknowns defined on the cross-points, and the reduced system associated to the interface unknowns is build in such a way that it is solvable. In a strategy proposed in [53, 36], the discrete physical unknowns defined at the cross-points are kept in the reduced system. These approaches improve the convergence, but they require global communication between the subdomains to solve a reduced system. In the context of elliptic problems, several cross-point techniques have been proposed and studied in [133, 134, 216, 136].

For 2^{nd} order, HABC, PML and non-local operators, difficulties already appear when defining the algorithm at the continuous level. Cross-point treatments have recently been investigated for 2^{nd} order operators [239, 100, 101, 131]. Strategies have also been proposed for HABC and PML transmission conditions in [A12] and [210, A15], respectively, for checkerboard domains partitions. The contributions [A12] and [A15] are presented in Sections 3.2 and 3.3, respectively. The FEM-BEM coupling with domain decomposition has been investigated e.g. in [204, 37, 45].

In a promising approach recently investigated in a series of works by Claeys et al. [242, 72, 75, 74, 73], the reduced system (3.1.5) is written with a more general definition of the exchange operator, which naturally accommodates the presence of cross-points for general mesh partitions.

3.1.3 Preconditioning techniques

Preconditioning strategies have been developed for both the global problem and the reduced problem to speed up the iterative solution procedures. Let $\mathbf{Au} = \mathbf{b}$ be the algebraic system resulting from the finite element discretization of the global problem (3.1.1). The *left* and *right preconditioned systems* of this problem are $(\mathbf{P}^{-1}\mathbf{A})\mathbf{u} = (\mathbf{P}^{-1}\mathbf{b})$ and $(\mathbf{AP}^{-1})(\mathbf{Pu}) = \mathbf{b}$ with a *preconditioner* $\mathbf{P}$. The matrix $\mathbf{P}$ must be chosen such that applying its inverse on any vector is affordable, and solving the preconditioned system is faster than solving the original system.

Several preconditioning strategies not related to DDMs have been proposed, see e.g. [113]. For example, in [27], the matrix resulting from the discretization of a Laplace problem is used to precondition the Helmholtz problem. In the *complex shifted Laplace* (CSL) *preconditioner* proposed in [116], a complex scalar term is added to the Laplace operator. The CSL preconditioner has been studied and combined with multigrid and/or deflation strategies in [115, 130, 203, 107]. *Multilevel preconditioning* consists in applying successively two or more preconditioners, corresponding to the different preconditioning strategies, or to the same strategy with different parameters at each level, see e.g. [114, 265].

[1] Note that, in the FETI-H method, only one ABC transmission condition is prescribed at each interface, and the additional interface condition enforce the continuity of the Dirichlet traces.

Schwarz preconditioners. The *Schwarz preconditioners* are defined by using local problems posed on the subdomains of a domain partition. They are used on the system associated to the global problem. There are many variants, generally with overlapping subdomains, see e.g. [269, 129, 103].

The *restricted additive Schwarz* (RAS) preconditioner [269] is given by

$$\mathbf{P}^{-1} = \sum_I \mathbf{R}_I^T \mathbf{D}_I \mathbf{A}_I^{-1} \mathbf{R}_I,$$

where $\mathbf{R}_I$ is the *restriction matrix* that selects the entries of the input vector that belong to the subdomain Ω_I, $\mathbf{D}_I$ is a *partition unity matrix* such that $\mathbf{I} = \sum_I \mathbf{R}_I^T \mathbf{D}_I \mathbf{R}_I$ is the identity matrix, and $\mathbf{A}_I = \mathbf{R}_I \mathbf{A} \mathbf{R}_I^T$ is a local finite element matrix associated to a local problem defined on Ω_I. This method is related to the block Jacobi method and the original parallel Schwarz algorithm, where the local problem can be solved in parallel. In the *multiplicative Schwarz* (MS) method, the local problems are solved sequentially, allowing information transfer across the entire domain partition at each iteration. This approach is related to the alternating Schwarz algorithm, the block Gauss-Seidel method and the sweeping methods (see below).

To speed up the convergence, each matrix $\mathbf{A}_I$ can be modified such that a Robin boundary condition or a domain truncation technique is prescribed at the boundary of Ω_I. This approach leads to the *optimized restricted additive Schwarz* (ORAS) and *optimized multiplicative Schwarz* (OMS) methods. The ORAS method has been studied for Helmholtz problems with optimized 0^{th} and 2^{nd} order operators in [137]. In [284, 49], a PML is used at the boundary of each subdomain. The convergence of Schwarz preconditioners for Helmholtz problems with and without absorption has been studied in [155, 156, 151, 51, 152].

Sweeping methods. In the sweeping methods, local problems associated with the subdomains are solved sequentially in a certain order to *sweep* the partition at each iteration. The principle is the same as for the MS method, but this point of view is more general. It leads to domain decomposition algorithms and to preconditioning techniques for both the global problem (3.1.1) and the reduced problem (3.1.5).

For 1D domain partitions, the matrices of the global and reduced systems can be rewritten as block tridiagonal matrices if the subdomains are numbered in a consecutive order. Sweeping methods based on the Gauss-Seidel algorithm consist of forward and backward sweeps, which are performed sequentially or in parallel, depending on the algorithm. In the context of Helmholtz problems, these sweeps follow the natural propagation of waves in the domain.

These methods were first proposed and studied in the 90's for convection-diffusion problems [231, 233]. They have attracted much interest for Helmholtz problems, promising a number of iterations that is quasi independent of the number of subdomains, see e.g. [58, 112, 270, 289, 271, 290, 55]. They are very efficient for waveguide and open cavity configurations, which have a unique natural direction in which information is transferred. More recently, multidimensional sweeping preconditioners for checkerboard domain partitions have been proposed in [292, 293, 274, 210, 211, A4]. The contribution [A4] is presented in section 3.4. See [138, 55] for more detailed reviews and comparisons of sweeping preconditioners.

DDM with multilevel preconditioning. The DDMs involving only local communications between the subdomains, such as ORAS, cannot scalable with respect to the number of subdomains. The sweeping and OMS methods can scalable, but they require sequential operations that reduce the parallel performance. With a second preconditioning level, the DDM is enriched by using a coarse problem defined on the entire domain partition. The coarse problem must be cheap to solve, and it introduces global exchanges. The combination of a coarse space method with a substructuring or preconditioning DDM is generally referred to as a *two-level DDM*.

The design of robust coarse space methods for Helmholtz problems is very challenging, and several approaches have been (and are still being) investigated in the community. Several *coarse* preconditioning matrices have been tested for the reduced system of the FETI and FETI-like methods, see e.g. [94, 120, 118, 15]. In [197, 89, 46, 140, 50], several coarse spaces are combined with the RAS and ORAS methods, which correspond to *two-level Schwarz preconditioners*.

3.2 DDM with HABC transmission and cross-point treatment

This contribution is the result of a collaboration with X. Antoine, C. Geuzaine and A. Royer. It corresponds to the article [A12]. I obtained the numerical results using `GetDDM` scripts.

In the contribution, we consider a non-overlapping domain decomposition substructuring method with high-order transmission conditions proposed by Boubendir, Antoine and Geuzaine [52]. In that work, no specific cross-point treatment was used, and only low-order exterior ABCs were considered.

We have proposed a cross-point treatment for checkerboard domain partitions when the Padé-type HABC operator is used in the transmission condition, in the exterior condition, or in both. For a complete definition of the local problems defined on the subdomains, additional conditions are required at the interior corners of the subdomains. In our approach, appropriate corner conditions based on [A9] are introduced, and additional transmission variables are defined at the cross-points.

The proposed cross-point treatment speeds up the convergence of the DDM. If the exterior boundary condition is a HABC, the method cannot converge without the cross-point treatment. While this approach is designed for regular checkerboard domain partitions (i.e. with only parallel and perpendicular interfaces) and homogeneous media, we have observed that it gives good results with distorted partitions and smoothly varying heterogeneous media.

3.2.1 Description of the substructuring method

Global problem. We consider the Helmholtz equation on a rectangular domain Ω, with Padé-type HABCs on the edges (denoted Γ_f for $f = 1 \dots 4$), and compatibility relations at the corners (denoted $C_{ff'}$ for any adjacent edges Γ_f and $\Gamma_{f'}$). The problem reads as follows.

- An unknown field u defined on Ω is governed by

$$\begin{cases} -\Delta u - \kappa^2 u = s, & \text{in } \Omega, \\ \partial_{n_f} u - \mathcal{L}\big(u, \{\varphi_{f,i}\}_{i=1\dots N}\big) = 0, & \text{on each } \Gamma_f. \end{cases} \tag{3.2.1}$$

- On each edge Γ_f, auxiliary fields $\{\varphi_{f,i}\}_{i=1\dots N}$ are governed by

$$\begin{cases} -\partial_{\tau_f\tau_f}\varphi_{f,i} - \kappa^2\big((e^{\imath\phi}c_i + 1)\varphi_{f,i} + e^{\imath\phi}(c_i+1)u\big) = 0, & \text{on } \Gamma_f. \\ \partial_{\tau_f}\varphi_{f,i} - \mathcal{L}\big(\varphi_{f,i}, \{\psi_{ff',ii'}\}_{i'=1\dots N}\big) = 0, & \text{on each } C_{ff'}, \end{cases}$$

  for $i = 1 \dots N$, where $\Gamma_{f'}$ corresponds to any adjacent edge of Γ_f.
- At each corner $C_{ff'}$, auxiliary variables $\{\psi_{ff',ii'}\}_{i,i'=1\dots N}$ are defined by compatibility relations similar to equation (2.2.3).

In these equations, the wavenumber κ is a strictly positive real constant, $s(\boldsymbol{x})$ is a source term, N is the number of auxiliary fields, and ϕ is a rotating angle of the Padé-type HABC. For each Γ_f, ∂_{n_f} is the exterior normal derivative, and ∂_{τ_f} is the tangential derivative. The function $\mathcal{L}$ is defined as

$$\mathcal{L}\big(w, \{w_i\}_{i=1\dots N}\big) := \imath\kappa e^{\imath\phi/2}\Big[w + \frac{2}{M}\sum_{i=1}^{N} c_i(w + w_i)\Big],$$

with $M = 2N + 1$ and $c_i = \tan^2(i\pi/M)$.

DDM with HABC transmission conditions for checkerboard domain partition. We consider a partition of Ω into a grid of rectangular non-overlapping subdomains Ω_I (with $I = 1 \dots N_{\text{dom}}$). Each edge $\Gamma_{I,f}$ (with $f = 1 \dots 4$) of Ω_I is either an *interior edge* if it is shared by two subdomains (i.e. $\Gamma_{I,f} \not\subset \partial\Omega$) or a *boundary edge* otherwise (i.e. $\Gamma_{I,f} \subset \partial\Omega$). Two types of points deserve attention: the *interior*

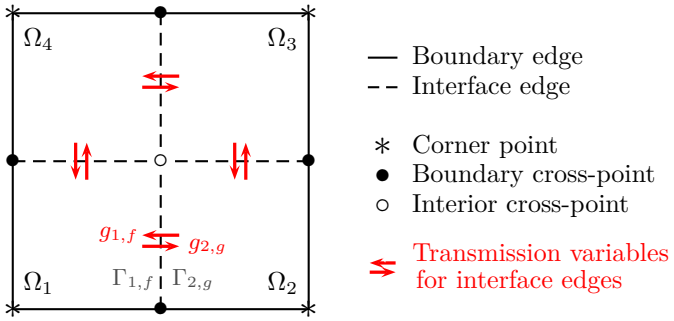

Figure 3.1: Terminology and notations. In this example, the continuity of the local solution u_1 and u_2 on the interior edge $\Gamma_{1,f} = \Gamma_{2,g}$ is ensured thanks to the transmission variables $g_{1,f}$ and $g_{2,g}$. Reproduced from [A12].

cross-points that do not touch the boundary of the global domain, and the *boundary cross-points* that touch the boundary of the global domain. See illustration in Figure 3.1 for a 2×2 partition.

The global problem (3.2.1) is decomposed into local problems defined on the subdomains, with transmission conditions based on Padé-type HABC operators. For the sake of simplicity, we assume that the parameters of the HABC operators are identical to those used for the exterior condition (i.e. N and ϕ). However, more general parameters could be used with some rules to maintain consistency, see [A12]. For each subdomain Ω_I, the local problem reads as follows.

- An unknown field u_I defined on Ω_I is governed by

$$\begin{cases} -\Delta u_I - \kappa^2 u_I = s, & \text{in } \Omega_I, \\ \partial_{n_{I,f}} u_I - \mathcal{L}\big(u_I, \{\varphi_{I,f,i}\}_{i=1\dots N}\big) = g_{I,f}, & \text{on each } \Gamma_{I,f}, \end{cases} \tag{3.2.2}$$

  where $g_{I,f}$ is a transmission variable.
- On each edge $\Gamma_{I,f}$, auxiliary fields $\{\varphi_{I,f,i}\}_{i=1\dots N}$ are governed by

$$-\partial_{\tau_{I,f}\tau_{I,f}}\varphi_{I,f,i} - \kappa^2\big((e^{\imath\phi}c_i + 1)\varphi_{I,f,i} + e^{\imath\phi}(c_i+1)u_I\big) = 0, \quad \text{on } \Gamma_{I,f}, \tag{3.2.3}$$

  for $i = 1 \dots N$.

If $\Gamma_{I,f}$ is a boundary edge, the second equation of system (3.2.2) is an exterior boundary condition, and $g_{I,f}$ is set to zero. If $\Gamma_{I,f}$ is an interior edge, the equation is a transmission condition, and the transmission variable is defined as $g_{I,f} := \partial_{n_{I,f}} u_J - \mathcal{L}\big(u_J, \{\varphi_{J,g,i}\}_{i=1\dots N}\big)$, where Ω_J is the neighboring subdomain, $\Gamma_{J,g} = \Gamma_{I,f}$ is the shared edge, u_J is the local solution on Ω_J, and $\{\varphi_{J,g,j}\}_{j=1\dots N}$ are the auxiliary fields on $\Gamma_{J,g}$. Since a problem similar to system (3.2.2) is defined on Ω_J, the transmission condition $\partial_{n_{J,g}} u_J - \mathcal{L}\big(u_J, \{\varphi_{J,g,j}\}_{j=1\dots N}\big) = g_{J,g}$ is prescribed on $\Gamma_{J,g}$. Therefore, $g_{I,f}$ can be written as

$$g_{I,f} = \begin{cases} 0, & \text{if } \Gamma_{I,f} \subset \partial\Omega, \\ -g_{J,g} - 2\mathcal{L}\big(u_J, \{\varphi_{J,g,j}\}_{j=1\dots N}\big), & \text{if } \Gamma_{I,f} \not\subset \partial\Omega. \end{cases} \tag{3.2.4}$$

Because of the second-order partial derivative in equation (3.2.3), boundary conditions must be prescribed on the auxiliary fields at the extremities of the edges. These extremities are the corners of the subdomains, which are interior/boundary cross-points or corners of the global domain. At the corners of Ω, the corner treatment based on compatibility relations must be applied for consistency with the global problem. At the cross-points, the missing conditions are provided by the treatment described below.

Cross-point treatment. The treatment is based on the following principles. The corner conditions described in Section 2.2.1 are prescribed at the corners of each subdomain. A corner condition can become a transmission condition by adding a transmission variable in the right-hand side. Therefore, at

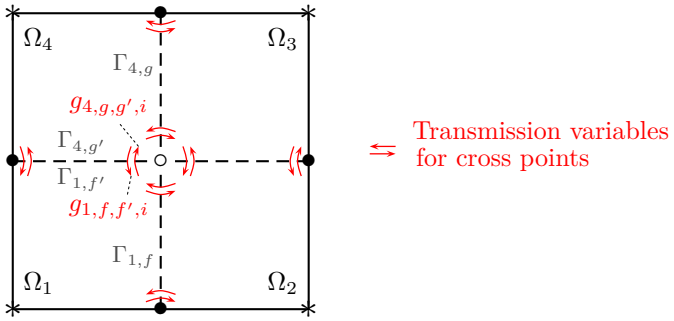

Figure 3.2: Transmission variables across the boundary and interior cross-points, if the HABC operator is used both in the exterior boundary condition and in the interface conditions. In the example, the continuity of the auxiliary fields $\varphi_{1,f,i}$ and $\varphi_{4,g,i}$ (defined on the aligned edges $\Gamma_{1,f}$ and $\Gamma_{4,g}$) at the interior cross-point $C_{1,ff'} = C_{4,gg'}$ is ensured thanks to the transmission variables $g_{1,ff',i}$ and $g_{4,gg',i}$. Reproduced from [A12].

each extremity of each edge $\Gamma_{I,f}$, a boundary or transmission condition is prescribed on the auxiliary fields. It is a boundary condition if the adjacent edge $\Gamma_{I,f'}$ is a boundary edge, and it is a transmission condition if the adjacent edge is an interior edge. In the latter case, the transmission condition ensures the continuity of the auxiliary fields that are on the same line of the domain partition.

Following these principles, the description of the formulation with domain decomposition can be completed. For each edge $\Gamma_{I,f}$, the auxiliary fields $\{\varphi_{I,f,i}\}_{i=1\dots N}$ defined on $\Gamma_{I,f}$ are governed by

$$\begin{cases} -\partial_{\tau_{I,f}\tau_{I,f}}\varphi_{I,f,i} - \kappa^2\big((e^{\imath\phi}c_i+1)\varphi_{I,f,i} + e^{\imath\phi}(c_i+1)u_I\big) = 0, & \text{on } \Gamma_{I,f}, \\ \partial_{n_{I,f'}}\varphi_{I,f,i} - \mathcal{L}\big(\varphi_{I,f,i}, \{\psi_{I,ff',ii'}\}_{i'=1\dots N}\big) = g_{I,ff',i}, & \text{on each } C_{I,ff'}, \end{cases} \tag{3.2.5}$$

where $C_{I,ff'}$ is any corner shared by $\Gamma_{I,f}$ and an adjacent edge $\Gamma_{I,f'}$. If $\Gamma_{I,f'}$ is a boundary edge, the second equation is a boundary condition, and the transmission variables are set to zero. If $\Gamma_{I,f'}$ is an interior edge, the second equation is a transmission condition, and the transmission variables depend on the solution of the other side of $\Gamma_{I,f'}$. On each $C_{I,ff'}$, the transmission variables $\{g_{I,ff',i}\}_{i=1\dots N}$ verify

$$g_{I,ff',i} = \begin{cases} 0, & \text{if } \Gamma_{I,f'} \subset \partial\Omega, \\ -g_{J,gg',i} - 2\mathcal{L}\big(\varphi_{J,g,i}, \{\psi_{J,gg',ii'}\}_{i'=1\dots N}\big), & \text{if } \Gamma_{I,f'} \not\subset \partial\Omega, \end{cases} \tag{3.2.6}$$

for $i = 1 \dots N$. In the latter case, the indices are chosen in such a way that Ω_J is the neighboring subdomain on the other side of $\Gamma_{I,f'}$, $\Gamma_{J,g'} = \Gamma_{I,f'}$ is the shared edge, and $\Gamma_{J,g}$ is aligned with $\Gamma_{I,f}$, see Figure 3.2. The transmission conditions enforce the continuity of $\varphi_{I,f,i}$ and $\varphi_{J,g,i}$ at the cross point. The variables $\psi_{I,ff',ii'}$ and $\psi_{J,gg',ii'}$ are defined by compatibility similarly to equation (2.2.3).

Global solution procedure. With the fixed-point iteration, each step of the global solution procedure consists of solving a local problem on each subdomain, and updating the transmission variables at both edges and cross-points. The procedure starts with initial values for the transmission variables. At each iteration ℓ, the solution $u_I^{(\ell)}$ and the auxiliary fields $\{\varphi_{I,f,i}^{(\ell)}\}_{f,i}$ are updated by solving equation (3.2.2) and equation (3.2.5) for each subdomain Ω_I. Then, the interface and cross-point transmission variables are updated by using relations based on equations (3.2.4) and (3.2.6).

The global process can be recast as one application of an iterative operator $\mathcal{A} : \mathcal{G} \to \mathcal{G}$ defined by $g^{(\ell+1)} = \mathcal{A}g^{(\ell)} + b$, where $g^{(\ell)} \subset \mathcal{G}$ is the set of transmission data, and b depends on the source term s. This can be seen as a fixed-point iteration to solve the linear system $(\mathcal{I} - \mathcal{A})g = b$, where $\mathcal{I}$ is the identity operator. This system can be solved by using a Krylov iterative solvers. Here, by contrast with most of the approaches, transmission data are associated to both interfaces and cross-points.

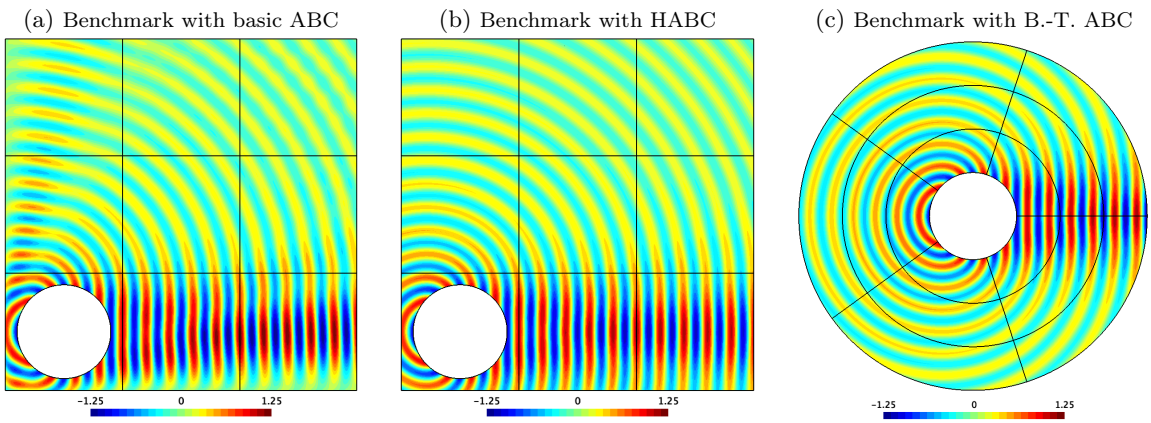

Figure 3.3: Real part of the reference numerical solution for three configurations. The basic ABC, the Padé-type HABC ($N = 6$ and $\phi = 0.3\pi$) and the second-order Bayliss–Turkel ABC are set on the exterior border Γ_{ext}. *Parameters: scattering disk of radius* 1*, square subdomains of size* 2.5×2.5*, plane wave* $u_{\text{inc}}(\boldsymbol{x}) = e^{\imath\kappa x}$*, boundary condition* $u = -u_{\text{inc}}$ *on* Γ_{sca}*, wavenumber* $\kappa = 4\pi$*, number of vertices per wave length* $n_\lambda = 10$*, second-order curvilinear triangular elements, second-degree polynomial basis functions.* Reproduced from [A12].

3.2.2 Computational results

To validate and study our approach, we have considered reference benchmarks that represent the scattering of a plane wave by a sound-soft circular obstacle. The simulations are performed on a square domain with a 3×3 checkerboard domain partition. Either a basic ABC (Figure 3.3a) or a Padé-type HABC with corner conditions (Figure 3.3b) is prescribed on the exterior boundary. The relative L^2-errors of the numerical solutions compared to the reference free space analytic solution are 2.2×10^{-1} and 2.4×10^{-3}, respectively. See [A12] for results with a circular domain (Figure 3.3c).

The DDM procedure with the GMRES iteration, the HABC transmission condition, and the cross-point treatment. The same HABC parameters N and ϕ are used for all the interior edges, but they can be different from the parameters of the HABC on the boundary edges. The results have been obtained with the mesh generator `Gmsh` [142], the solver `GetDP` [106], and the interface `GetDDM` [281]. Repository: `https://gitlab.onelab.info/doc/models/-/tree/master/HelmholtzDDMwithCrosspoints`.

Convergence history. The relative residual and the relative L^2-error are plotted as functions of the number of iterations in Figure 3.4. The L^2-error is computed by comparing the local solution obtained in each subdomain with the global solution computed on the same mesh without domain decomposition. The dotted lines correspond to results without the cross-point treatment, i.e. the associated terms are removed from the formulation, which is equivalent to a homogeneous Neumann boundary condition on the auxiliary fields at the cross-points.

When the basic ABC is prescribed on $\partial\Omega$, the residual and the error decrease during the iterations in all the cases (Figures 3.4a and 3.4b). The decay is faster when the cross-point treatment is enabled. It can be accelerated further, up to a certain point, by taking N sufficiently large. When the HABC is prescribed on $\partial\Omega$, the impact of the cross-point treatment is more important. Note that, if the cross-point treatment is not enabled, the residuals decrease with the iterations (Figure 3.4c), but the relative errors reach a plateau and stagnate at 10^{-1} (Figure 3.4d). This can be explained by noting that auxiliary fields are defined on the edges of the domain Ω, and the continuity of these auxiliary fields must be ensured at the boundary cross-points. Without the cross-point treatment, the problem with domain decomposition is not compatible with the original problem, and the iterations converge towards a wrong solution.

With the cross-point treatment, the residual and the error drop between the 3^{rd} and 4^{th} iterations in all the cases. This can be interpreted by looking at the solution after each iteration (Figure 3.5). Initially, only the subdomain containing the scattering object has a non-zero numerical solution. This

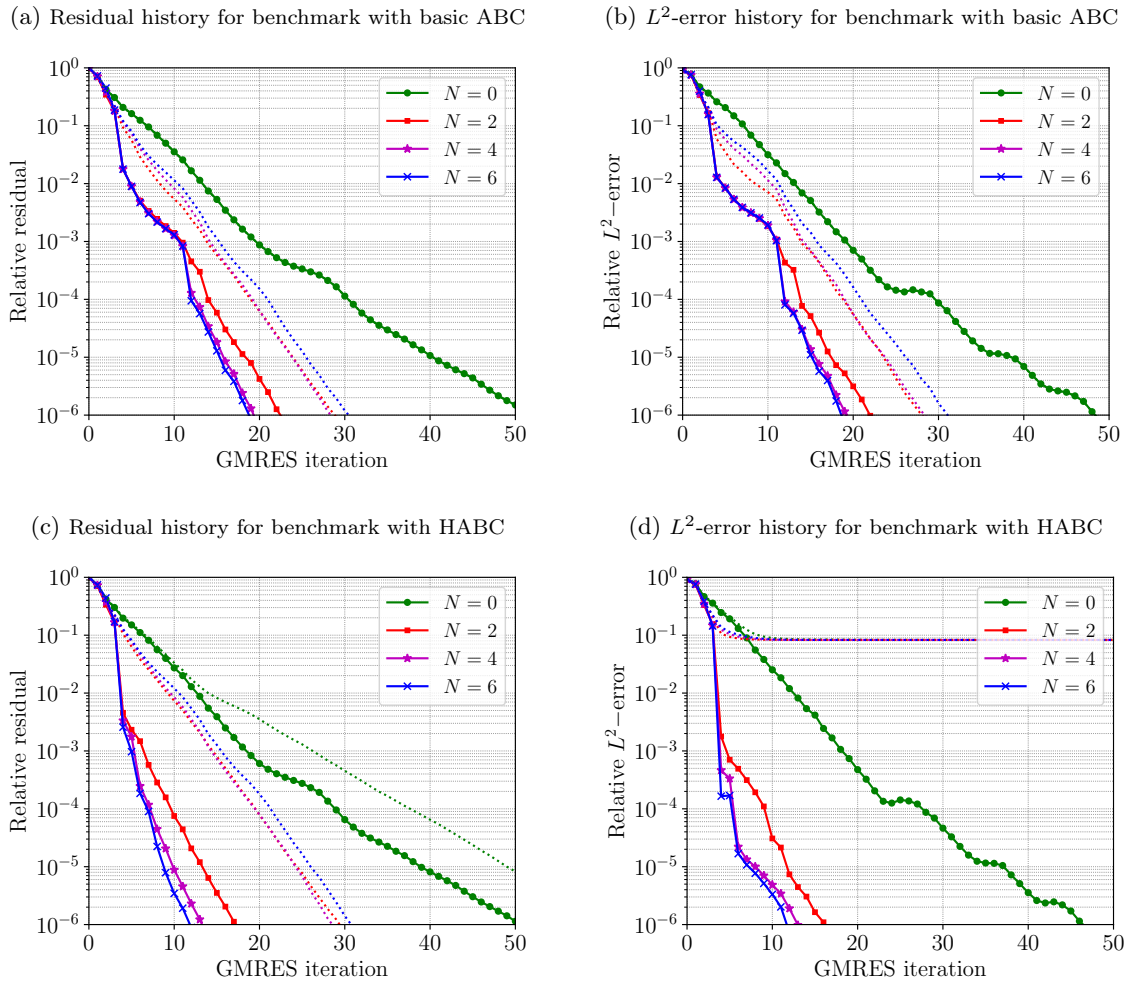

Figure 3.4: Evolution of relative residual *(left)* and relative L^2-error *(right)* during the GMRES iterations. The L^2-error is computed by comparing the numerical solution to the reference numerical solution obtained without domain decomposition. HABC transmission conditions with $N = 0, 2, 4, 6$ auxiliary fields and $\phi = 0.3\pi$ are used. The dotted lines correspond to the results obtained when the cross-point treatment is not used (only for $N = 2, 4, 6$). Handling the cross-point procedure is represented by continuous lines. Reproduced from [A12].

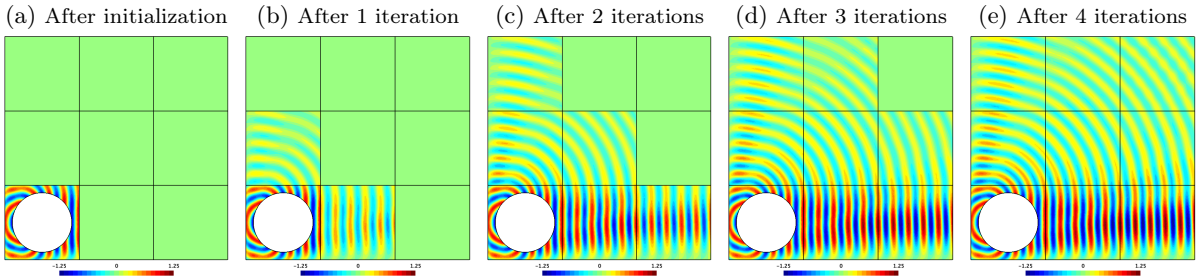

Figure 3.5: Evolution of the solution during the GMRES iterations for configuration 1 and the HABC-based transmission condition with $N = 4$ and $\phi = 0.3\pi$. The first picture is obtained after initialization of the right-hand side of the transmission system. Reproduced from [A12].

solution is already quite accurate since the transmission condition acts as a HABC, and the cross-point treatment behaves as the appropriate corner treatment. The signal is then propagated from subdomain to subdomain during the iterations, and it reaches the last subdomain in the 4^{th} iteration.

(a) Influence of the wavenumber κ (with $n_\lambda = 10$)

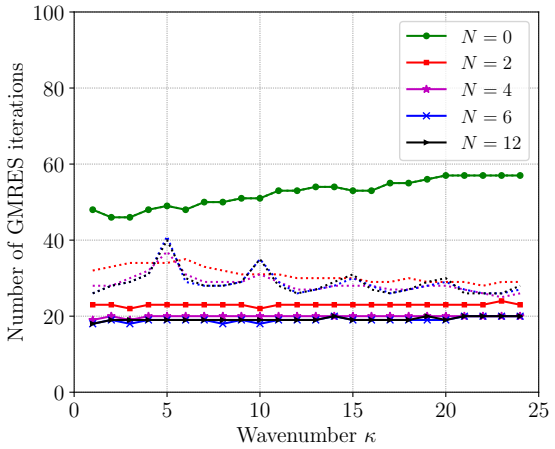

(b) Influence of the mesh density n_λ (with $\kappa = 4\pi$)

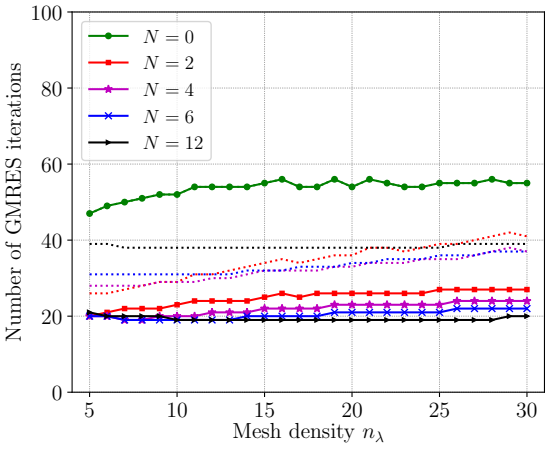

(c) Influence of the number of auxiliary fields N and the rotating angle ϕ in the HABC transmission condition

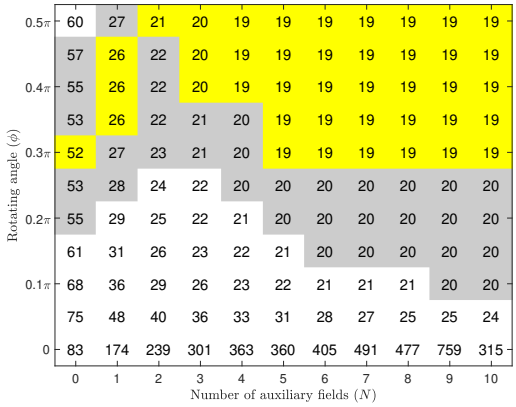

(d) Influence of the number of subdomains per direction

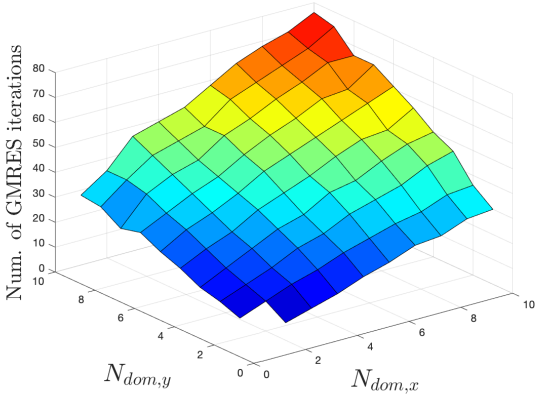

Figure 3.6: Influence of the parameters on the number of GMRES iterations to reach the relative residual 10^{-6}. In Figures (a) and (b), the dotted lines correspond to the results obtained when the cross-point treatment is not used. In Figure (c), the yellow cells correspond to the smallest number of iterations for each N. Figure (d) corresponds to a weak scaling analysis where the size of the size of the domain increases with the number of subdomains. *Parameters:* $\kappa = 4\pi$, $n_\lambda = 10$, $N = 6$, $\phi = 0.3\pi$, $N_{\mathrm{dom},x} \times N_{\mathrm{dom},y} = 3 \times 3$. Reproduced from [A12].

Influence of the parameters. The number of GMRES iterations to reach the relative residual 10^{-6} is computed by modifying the parameters of the problem/method one by one. We consider only the problem with the basic ABC on the exterior boundary, and the cross-point treatment at every cross-point.

Influence of the wavenumber κ and the mesh density n_λ (Figures 3.6a and 3.6b). High frequency simulations are challenging because they require fine meshes with high mesh densities to avoid the pollution effect. The efficiency of the method for large values of κ and n_λ is therefore an important issue. For $N = 0$, the number of iterations slowly increases with respect to κ. By contrast, for higher values of N, the convergence does not change significantly with κ when the cross-point treatment is used. For all the values of N, the number of iterations increases with the mesh density n_λ. Fortunately, with the cross-point treatment, the number of iterations can be kept constant when increasing n_λ by taking N larger, and a convergence independent of the mesh density can be achieved provided that N is sufficiently large. This was already observed in [52] on configurations without interior cross-points. These results indicate that the method is well-adapted to high-frequency problems with high density meshes.

Influence of the parameters of the HABC transmission condition (Figure 3.6c). We observe that the Padé case (i.e. rotating angle $\phi = 0$) gives the worst result whatever the number of auxiliary fields N,

(a) Velocity model

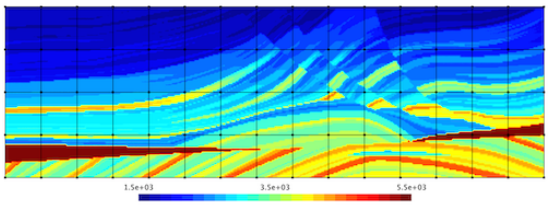

(b) Real part of the solution

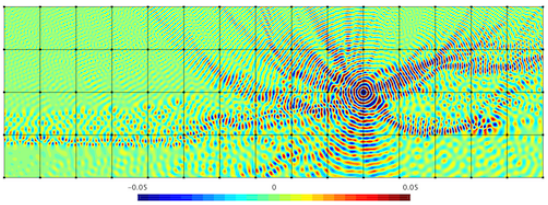

(c) Number of iterations without cross-point treatment

$\phi \rightarrow$	0	0.1π	0.2π	0.3π	0.4π	0.5π
$N = 0$	120	94	88	91	103	123
$N = 1$	>200	56	51	48	48	49
$N = 2$	>200	51	47	47	47	48
$N = 3$	>200	51	47	47	47	47

(d) Number of iterations with cross-point treatment

$\phi \rightarrow$	0	0.1π	0.2π	0.3π	0.4π	0.5π
$N = 0$	120	94	88	91	103	123
$N = 1$	>200	54	49	47	46	48
$N = 2$	>200	47	45	44	44	44
$N = 3$	>200	45	43	43	44	44

Figure 3.7: Marmousi benchmark: Pictures of the spatially varying medium (a) and the real part of the solution (b) with the domain partition. Numbers of GMRES iterations to reach the relative residual 10^{-4} without/with cross-point treatment (c)-(d). Reproduced from [A12].

and it should be avoided. For any given $\phi > 0$, increasing N accelerates the convergence, up to a certain limit. Unfortunately, increasing N leads to a higher computational cost and a slightly larger amount of communication. By contrast, the selection of the parameter ϕ can accelerate the convergence of the iterative process at no additional cost. The optimal value of ϕ depends on N, which makes the choice of the parameter rather tricky. Fortunately, the number of iterations is not very sensitive to ϕ as soon as ϕ is sufficiently large. Here, we always use $\phi = 0.3\pi$, which is a nearly-optimal value in all the cases.

Influence of the number of subdomains (Figure 3.6d). The simulation is performed by increasing the number of subdomains in both Cartesian directions (i.e. $N_{\text{dom},x}$ and $N_{\text{dom},y}$), and by increasing the size of the main domain accordingly. We observe that the number of iterations increases linearly with the number of subdomains in each direction. This is expected, because the transmission of information from subdomain to subdomain is local. The method could be combined with a preconditioning technique with global communications between the subdomains, e.g. sweeping or coarse spaces techniques.

Experiments with heterogeneous media or non-right angles The proposed DDM is a priori only suitable for wave propagation in homogeneous media and domain partitions with right angles. However, it can be used as an empirical approach with heterogeneous media and partitions with non-right angles.

Heterogeneous medium. We consider a rectangular domain partitioned into 4×15 rectangular subdomains with a velocity map $c(\boldsymbol{x})$ representing a geological structure (Figure 3.7a) and a Dirac source on an interior cross-point (Figure 3.7b). The spatially varying $\kappa(\boldsymbol{x}) = \omega/c$ is used as is in the equations, which were originally derived for a constant κ. The number of GMRES iterations to reach the relative residual 10^{-4} is given in Tables 3.7c and 3.7d for configurations without/with cross-point treatment, respectively. The lowest number of iterations is obtained by using the HABC transmission condition with the cross-point treatment, and taking $N \geq 1$ and $\phi > 0$. However, the speedup rapidly stagnates as N is increased, and using $N = 1$ or 2 is sufficient. Nevertheless, this approach provides a significant speedup in comparison with the basic impedance condition, with a moderate supplementary computational cost, and the cross-point treatment remains effective.

Non-right angles. The scattering benchmarks considered above were tested with distorted partitions: the cross-points are moved, creating acute and obtuse angles in the partitions. In the numerical results (not shown for brevity), we have observed that the method with the cross-point treatment converges to the correct solution, even with a significant distortion of the partition. In almost all the cases, the number of GMRES iterations increases when the distortion of the partitions is increased, but using the HABC transmission condition and the cross-point treatment still speeds up the convergence.

3.3 DDM with PML transmission and cross-point treatment

This contribution is the result of a collaboration with E. Béchet, C. Geuzaine and A. Royer, in the framework of the doctoral research of A. Royer. It corresponds to the article [A15]. The numerical results have been obtained by A. Royer with the libraries `GmshFEM` and `GmshDDM`.

In this contribution, we have proposed a non-overlapping DDM with PML transmission conditions for checkerboard domain partitions. It is similar to the one presented in Section 3.2, but the difficulties are different. The domain is partitioned into subdomains, and each subdomain is extended with a Cartesian PML. To define properly the DDM, the continuity of the solution at the interface between the PML regions and the subdomain is enforced only weakly by using Lagrange multipliers. These multipliers can be interpreted as Neumann traces of the solution at the interfaces. We have considered two different discretization techniques for these multipliers.

Interior and boundary cross-points are considered in a rather natural way. The numerical results and the conclusions are similar to those for the DDM with HABC transmission conditions presented in Section 3.2.

3.3.1 Description of the substructuring method

We consider the 2D Helmholtz equation on a rectangular domain Ω surrounded by a Cartesian PML Ω_{pml}. A homogeneous Neumann boundary condition is prescribed on the exterior boundary of the PML. Denoting the union of the domain and the PML by Ω_{all}, the problem reads as follows:

$$\begin{aligned}&\text{Find } u_{\text{all}} \in H^1(\Omega_{\text{all}}) \text{ such that, for all } v_{\text{all}} \in H^1(\Omega_{\text{all}}),\\ &\quad\int_{\Omega_{\text{dom}}} \Big[\nabla u_{\text{all}} \cdot \nabla v_{\text{all}} - \kappa^2 u_{\text{all}} v_{\text{all}}\Big]\, d\Omega\\ &\qquad + \int_{\Omega_{\text{pml}}} \Big[(\boldsymbol{\Lambda}_{\text{pml}} \nabla u_{\text{all}}) \cdot \nabla v_{\text{all}} - \alpha_{\text{pml}}\, \kappa^2 u_{\text{all}} v_{\text{all}}\Big]\, d\Omega = \int_{\Omega_{\text{dom}}} s v_{\text{all}}\, d\Omega,\end{aligned} \tag{3.3.1}$$

where the wavenumber κ is a strictly positive real constant, the tensor field $\boldsymbol{\Lambda}_{\text{pml}}(\boldsymbol{x})$ and the scalar field $\alpha_{\text{pml}}(\boldsymbol{x})$ are complex material parameters defined in Section 2.3.1, and $s(\boldsymbol{x})$ is a source term which the support is compact on Ω.

Variational formulation of the global problem with Lagrange multipliers. The Cartesian PML is partitioned into *edge PMLs* and *corner PMLs* associated, respectively, to the edges and the corners of the domain, see Figure 3.8. The edges of the domain are denoted by Γ_f (with $f = 1 \dots 4$), and its corners are denoted by $C_{ff'}$ (where Γ_f and $\Gamma_{f'}$ are any adjacent edges). The edge PML and corner PML corresponding to Γ_f and $C_{ff'}$ are denoted by Ω_f and $\Omega_{ff'}$, respectively. The interface between an edge PML Ω_f and a corner PML $\Omega_{ff'}$ is denoted by $\Gamma_{ff'}$. Let us note that $\Omega_{ff'} = \Omega_{f'f}$, but $\Gamma_{ff'} \neq \Gamma_{f'f}$.

The global problem (3.3.1) is rewritten as the coupling of local problems associated to the domain and the edge/corner PMLs. The corresponding local solutions are denoted by u, u_f and $u_{ff'}$, for Ω, Ω_f and $\Omega_{ff'}$, respectively. The continuity of the local solutions on the interfaces are enforced weakly by using Lagrange multipliers. We introduce an *edge Lagrange multiplier* λ_f on each Γ_f, and a *corner Lagrange multiplier* $\lambda_{ff'}$ on each $\Gamma_{ff'}$. Let us note that $u_{ff'} = u_{f'f}$, but $\lambda_{ff'} \neq \lambda_{f'f}$.

The collections of local solutions and Lagrange multipliers are denoted by u_{all} and λ_{all}, respectively. They belong to the following functional spaces:

$$\begin{aligned}\mathcal{U}_{\text{all}} &:= H^1(\Omega) \oplus \Big[\bigoplus\nolimits_{\Omega_f} H^1(\Omega_f)\Big] \oplus \Big[\bigoplus\nolimits_{\Omega_{ff'}} H^1(\Omega_{ff'})\Big],\\ \mathcal{L}_{\text{all}} &:= \Big[\bigoplus\nolimits_{\Gamma_f} H^{-1/2}(\Gamma_f)\Big] \oplus \Big[\bigoplus\nolimits_{\Gamma_{ff'}} H^{-1/2}(\Gamma_{ff'})\Big].\end{aligned}$$

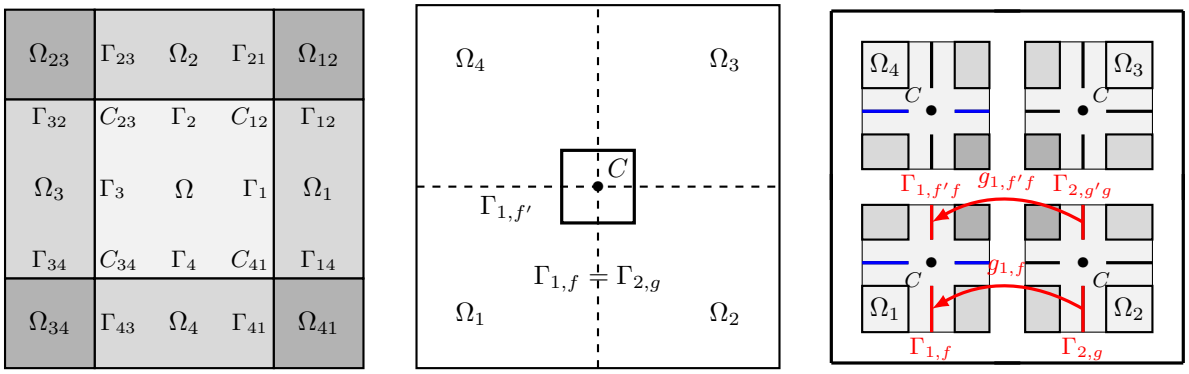

(a) Global domain Ω and the associated edge/corner PMLs.

(b) Partition of the global domain Ω into 2×2 subdomains.

(c) Data exchanges between the subdomains Ω_1 and Ω_2.

Figure 3.8: Notations for the global domain Ω (a), notations for the domain partition (b) and illustration of the data exchange at the interface between two subdomains (c). The black box on (a) corresponds to a zoom on the black bock on figure (b). Adapted from [A15].

The variational formulation of the problem then reads:

$$
\begin{aligned}
&\text{Find } (u_{\text{all}}, \lambda_{\text{all}}) \in \mathcal{U}_{\text{all}} \times \mathcal{L}_{\text{all}} \text{ such that, for all } (v_{\text{all}}, \mu_{\text{all}}) \in \mathcal{U}_{\text{all}} \times \mathcal{L}_{\text{all}}, \\
&\int_\Omega \Big[\nabla u \cdot \nabla v - \kappa^2 u v\Big]\, d\Omega \\
&\quad + \sum_{\Omega_f} \int_{\Omega_f} \Big[(\boldsymbol{\Lambda}_{\text{pml}} \nabla u_f \cdot \nabla v_f - \alpha_{\text{pml}}\, \kappa^2 u_f v_f\Big]\, d\Omega \\
&\quad + \sum_{\Omega_{ff'}} \int_{\Omega_{ff'}} \Big[(\boldsymbol{\Lambda}_{\text{pml}} \nabla u_{ff'} \cdot \nabla v_{ff'} - \alpha_{\text{pml}}\, \kappa^2 u_{ff'} v_{ff'}\Big]\, d\Omega \\
&\quad + \sum_{\Gamma_f} \int_{\Gamma_f} \lambda_f (v_f - v)\, d\Gamma + \sum_{\Gamma_{ff'}} \int_{\Gamma_{ff'}} \lambda_{ff'} (v_{ff'} - v_f)\, d\Gamma = \int_\Omega s v\, d\Omega, \\
&\sum_{\Gamma_f} \int_{\Gamma_f} (u_f - u) \mu_i\, d\Gamma + \sum_{\Gamma_{ff'}} \int_{\Gamma_{ff'}} (u_{ff'} - u_f) \mu_{ff'}\, d\Gamma = 0.
\end{aligned}
\tag{3.3.2}
$$

In this formulation, the Lagrange multipliers can be interpreted as Neumann traces of the fields at the interfaces, i.e.

$$
\begin{aligned}
\lambda_f &= \boldsymbol{n} \cdot \nabla u = -\boldsymbol{n} \cdot (\boldsymbol{\Lambda}_{\text{pml}} \nabla u_f) && \text{on each } \Gamma_f, \\
\lambda_{ff'} &= \boldsymbol{n}_f \cdot (\boldsymbol{\Lambda}_{\text{pml}} \nabla u_f) = -\boldsymbol{n}_f \cdot (\boldsymbol{\Lambda}_{\text{pml}} \nabla u_{ff'}) && \text{on each } \Gamma_{ff'},
\end{aligned}
$$

where $\boldsymbol{n}$ and $\boldsymbol{n}_f$ are the external unit normal vectors relative to Ω and Ω_f, respectively.

DDM with PML transmission conditions for checkerboard domain partition. The domain Ω is partitioned into N_{dom} non-overlapping rectangular subdomains Ω_I (with $I = 1 \dots N_{\text{dom}}$) on a 2D grid, see illustration on Figure 3.8. The edges of each subdomain Ω_I are denoted by $\Gamma_{I,f}$ (with $f = 1 \dots 4$). An edge can be either a *boundary edge* if $\Gamma_{I,f} \subset \partial\Omega$ or an *interior edge* if $\Gamma_{I,f} \not\subset \partial\Omega$.

Each subdomain is extended with a Cartesian PML. The PML is used as a DtN operator thanks to the strategies developed in the previous section. To write the local problem associated to subdomain Ω_I, we introduce the sets of physical fields and Lagrange multipliers, denoted by $u_{I,\text{all}}$ and $\lambda_{I,\text{all}}$, respectively, for the subdomain Ω_I, the surrounding PML regions (denoted by $\Omega_{I,f}$ and $\Omega_{I,ff'}$) and the interfaces (denoted by $\Gamma_{I,f}$ and $\Gamma_{I,ff'}$). The corresponding functional spaces are denoted by $\mathcal{U}_{I,\text{all}}$ and $\mathcal{L}_{I,\text{all}}$.

A variational formulation similar to formulation (3.3.2) is used for every subdomain, but terms with transmission variables are added in the right-hand side of the first equation in order to enforce the

coupling between the local problems. For each subdomain Ω_I, the variational formulation reads:

$$
\begin{aligned}
&\text{Find } (u_{I,\text{all}}, \lambda_{I,\text{all}}) \in \mathcal{U}_{I,\text{all}} \times \mathcal{L}_{I,\text{all}} \text{ such that, } \forall (v_{I,\text{all}}, \mu_{I,\text{all}}) \in \mathcal{U}_{I,\text{all}} \times \mathcal{L}_{I,\text{all}},\\
&\int_{\Omega_I} \left[\nabla u_I \cdot \nabla v_I - \kappa^2 u_I v_I\right] d\Omega\\
&\quad + \sum_{\Omega_{I,f}} \int_{\Omega_{I,f}} \left[(\boldsymbol{\Lambda}_{I,\text{pml}} \nabla u_{I,f}) \cdot \nabla v_{I,f} - \alpha_{I,\text{pml}}\, \kappa^2 u_{I,f} v_{I,f}\right] d\Omega\\
&\quad + \sum_{\Omega_{I,ff'}} \int_{\Omega_{I,ff'}} \left[(\boldsymbol{\Lambda}_{I,\text{pml}} \nabla u_{I,ff'}) \cdot \nabla v_{I,ff'} - \alpha_{I,\text{pml}}\, \kappa^2 u_{I,ff'} v_{I,ff'}\right] d\Omega\\
&\quad + \sum_{\Gamma_{I,f}} \int_{\Gamma_{I,f}} \lambda_{I,f}(v_{I,f} - v_I)\, d\Gamma + \sum_{\Gamma_{I,ff'}} \int_{\Gamma_{I,ff'}} \lambda_{I,ff'}(v_{I,ff'} - v_f)\, d\Gamma\\
&\qquad = \int_{\Omega_I} s v_I\, d\Omega + \sum_{\Gamma_{I,f} \not\subset \Gamma_f} \int_{\Gamma_{I,f}} g_{I,f} v_I\, d\Gamma + \sum_{\Gamma_{I,ff'} \not\subset \Gamma_{ff'}} \int_{\Gamma_{I,ff'}} g_{I,ff'} v_{I,f}\, d\Gamma,\\
&\sum_{\Gamma_{I,f}} \int_{\Gamma_f} (u_{I,f} - u_I)\mu_{I,f}\, d\Gamma + \sum_{\Gamma_{I,ff'}} \int_{\Gamma_{I,ff'}} (u_{I,ff'} - u_{I,f})\mu_{I,ff'}\, d\Gamma = 0.
\end{aligned}
$$

The terms in blue introduce couplings at the interfaces *"subdomain/edges PML"* and *"edge PML/corner PML"* for neighboring subdomains. These couplings are illustrated in Figure 3.8c.

The variables $g_{I,f}$ and $g_{I,f,j}$ can be considered as *edge transmission variables* and *corner transmission variables*, respectively. At each step ℓ of the iterative solution procedure, these variables are updated using the relations

$$
\begin{aligned}
g_{I,f}^{(\ell+1)} &= -g_{J,g}^{(\ell)} + 2\lambda_{J,g}^{(\ell)} \qquad &&\text{on each } \Gamma_{I,f} \not\subset \Gamma_f\\
g_{I,ff'}^{(\ell+1)} &= -g_{J,gg'}^{(\ell)} + 2\lambda_{J,gg'}^{(\ell)} \qquad &&\text{on each } \Gamma_{I,ff'} \not\subset \Gamma_{ff'},
\end{aligned}
$$

where the Lagrange multipliers $\lambda_{J,g}$ and $\lambda_{J,gg'}$ are computed in the local problem associated to the neighboring subdomain Ω_J. This version of the DDM takes into account cross-points through the definition of the corner transmission variables.

Finite element discretization. The physical fields and the Lagrange multipliers are approximated by using finite elements. After discretization, formulation (3.3.2) leads to the saddle point problem

$$
\begin{bmatrix} \mathbf{U} & \mathbf{L}^\top \\ \mathbf{L} & 0 \end{bmatrix} \begin{bmatrix} \mathbf{u}_{\text{all}} \\ \boldsymbol{\lambda}_{\text{all}} \end{bmatrix} = \begin{bmatrix} \mathbf{s} \\ 0 \end{bmatrix}, \tag{3.3.3}
$$

where $\mathbf{u}_{\text{all}}$ and $\boldsymbol{\lambda}_{\text{all}}$ correspond to the discrete unknowns associated with the physical fields and the Lagrange multipliers, respectively, and $\mathbf{s}$ corresponds to the source term. The matrix $\mathbf{U}$ corresponds to the interactions between the physical fields, the matrix $\mathbf{L}$ corresponds to the terms with the Lagrange multipliers. The saddle point problem (3.3.3) has a unique solution if and only if (1) $\mathbf{L}$ is surjective and (2) the projection of $\mathbf{U}$ in the kernel of $\mathbf{L}$ is surjective.

The discretization strategies influence the properties of the system. The physical fields defined on the domain and the PMLs are discretized by using standard continuous finite elements with hierarchical polynomial basis functions, see e.g. [267]. For the Lagrange multipliers defined on the interfaces, we have considered two techniques.

Continuous Lagrange multipliers. In the first approach, the multipliers are discretized by using continuous finite elements with Lobatto polynomial basis functions. The multipliers are continuous over each interface. If the same polynomial degree is used for the physical fields and the multipliers, then the basis functions of the multipliers correspond to the restriction of the basis functions of the physical fields. Unfortunately, at each cross-point, the relations involving the nodal value of the Lagrange multipliers are

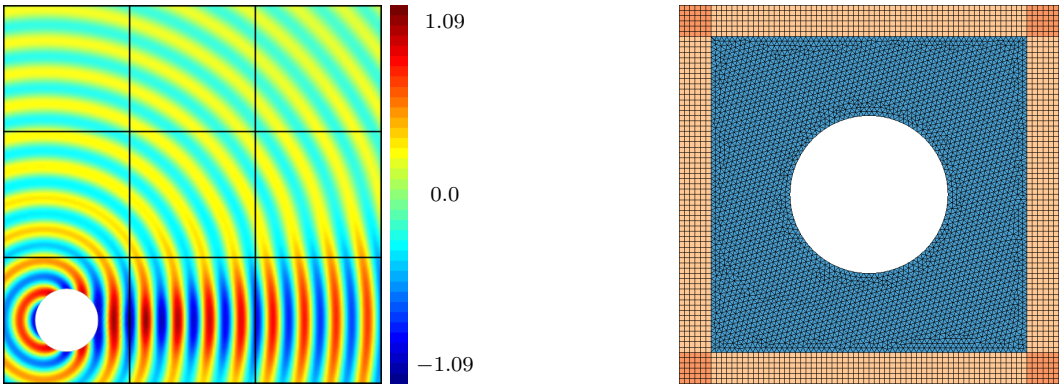

(a) Numerical solution and domain partition

(b) Mesh of one subdomain with the extruded PMLs

Figure 3.9: Reference benchmark: scattering of a plane wave by a disk in a square domain with a 3×3 domain partition. *Default parameters: size of a subdomain* 2×2*, radius of disk* $R = 0.5$*, wavenumber* $\kappa = 4\pi$*, characteristic mesh size* $h \approx 1/30$*, straight geometric finite elements, second-degree polynomial basis functions, shifted hyperbolic absorbing function* σ_{sh}*, layer thickness* $\delta_{\text{pml}} = hN_{\text{pml}}$ *with* $N_{\text{pml}} = 6$. Reproduced from [A15].

linearly dependent. Then, $\mathbf{L}$ is not surjective, and problem (3.3.3) is not solvable. To remove the linear dependence, an additional constraint has been introduced by using an additional Lagrange multiplier. A similar strategy was used by Peng and Lee [245] to improve a DDM for time-harmonic electromagnetic problems.

Discontinuous Lagrange multipliers. In the second approach, the multipliers are discretized by using discontinuous finite elements with Legendre polynomial basis functions. The continuity of the multipliers is not ensured at the interface between the elements. If the polynomial degree for the multipliers is lower than the polynomial degree of the physical fields, i.e. $\text{degree}(\lambda_{\text{all}}) < \text{degree}(u_{\text{all}})$, then the system is underdetermined, and the continuity of the physical fields at the interfaces is not ensured. In contrast, the continuity is ensured if $\text{degree}(\lambda_{\text{all}}) \geq \text{degree}(u_{\text{all}})$, but the system is overdetermined, and it is not solvable because $\mathbf{L}$ is not surjective. To overcome this issue, we have tested a penalization strategy, where a mass matrix is added in system (3.3.3),

$$\begin{bmatrix} \mathbf{U} & \mathbf{L}^\top \\ \mathbf{L} & \tau\mathbf{M} \end{bmatrix} \begin{bmatrix} \mathbf{u}_{\text{all}} \\ \boldsymbol{\lambda}_{\text{all}} \end{bmatrix} = \begin{bmatrix} \mathbf{s} \\ 0 \end{bmatrix},$$

where τ is a penalization parameter to be tuned and $\mathbf{M}$ is the mass matrix associated to the Lagrange multipliers, see e.g. [44]. Because of the penalization, the continuity of the discrete solution is not ensured, but it can be controlled thanks to τ. We have observed that the best approach corresponds to $\text{degree}(\lambda_{\text{all}}) = \text{degree}(u_{\text{all}})$ with the penalization strategy, see [A15].

In this manuscript, we consider either the continuous discretization with the additional constraint, or the discontinuous discretization with the penalization strategy. In both cases, $\text{degree}(\lambda_{\text{all}}) = \text{degree}(u_{\text{all}})$. Several alternative strategies have been studied in [A15].

3.3.2 Computational results

Description of the benchmark. We consider the scattering of a plane wave $u_{\text{inc}}(\boldsymbol{x}) = e^{i\kappa x}$ by a sound-soft disk. The finite element simulations are performed on a square domain surrounded by PMLs with a 3×3 checkerboard domain partition, and the disk is placed in the middle of the lower left subdomain, see Figure 3.9a. Every subdomain is meshed with triangular elements, and the surrounding PMLs are generated with extruded square elements, see Figure 3.9b.

The problem is solved by using the DDM procedure with the GMRES iteration. The absorbing function σ and the layer thickness $\delta_{\text{pml}} = hN_{\text{pml}}$ can be different for the PML transmission conditions

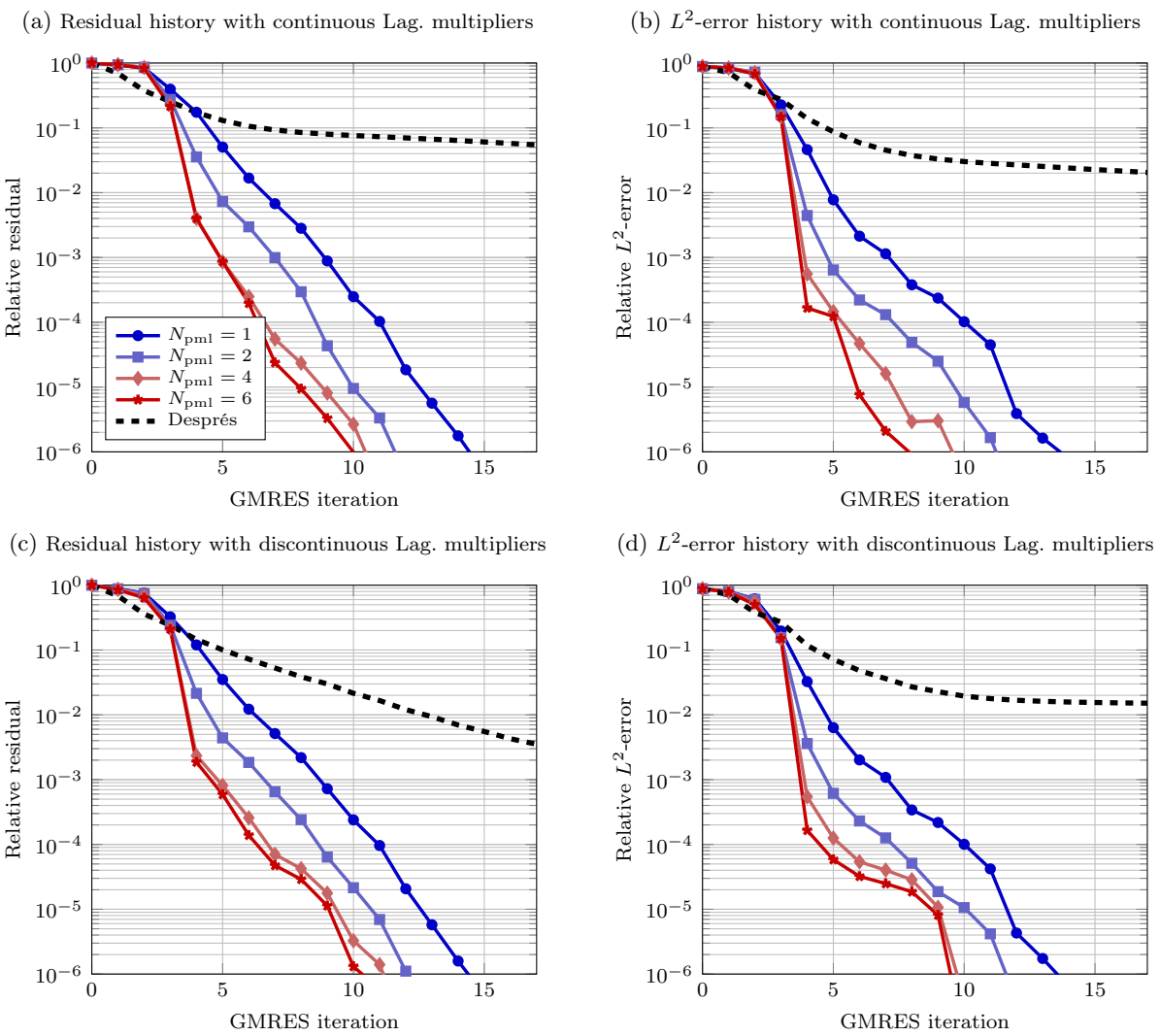

Figure 3.10: Relative GMRES residual *(left)* and the relative L_2-error *(right)* obtained with PML transmission conditions (for different layer thicknesses) and the standard impedance transmission condition. In all the cases, the exterior PML is used with a thickness of $N_{\text{pml}} = 6$ mesh cells. Adapted from [A15].

(i.e. for interior edges) and the PML exterior condition (i.e. for boundary edges). For the exterior condition, $N_{\text{pml}} = 6$ and the shifted hyperbolic function σ_{sh} (2.3.10) are used. By default, we consider second-degree polynomial basis functions for both physical fields and Lagrange multipliers. The results have been obtained by A. Royer with `GmshDDM`, a dedicated `C++` code based on the open-source finite element solver `GmshFEM` [258] and the mesh generator `Gmsh` [142].

Convergence history. In Figure 3.10, the relative residuals and the relative L_2-errors are plotted as functions of the number of iterations for both discretization techniques of the Lagrange multipliers. The relative L_2-error is computed by comparing the local solution obtained in each subdomain with a reference numerical solution computed on the same mesh without domain decomposition. Because the same discretization technique is used for multipliers corresponding to interior and boundary edges, the reference numerical solution depends on the considered discretization. In both case, the relative error between the reference numerical solution and the (free space) analytic solution is equal to 6.8×10^{-3}.

We observe that both the residual and the L_2-error decrease with the number of iterations in all the cases, and they have approximately the same order of magnitude at each iteration. The decay is faster with the one-cell PML transmission condition than with the basic impedance transmission condition.

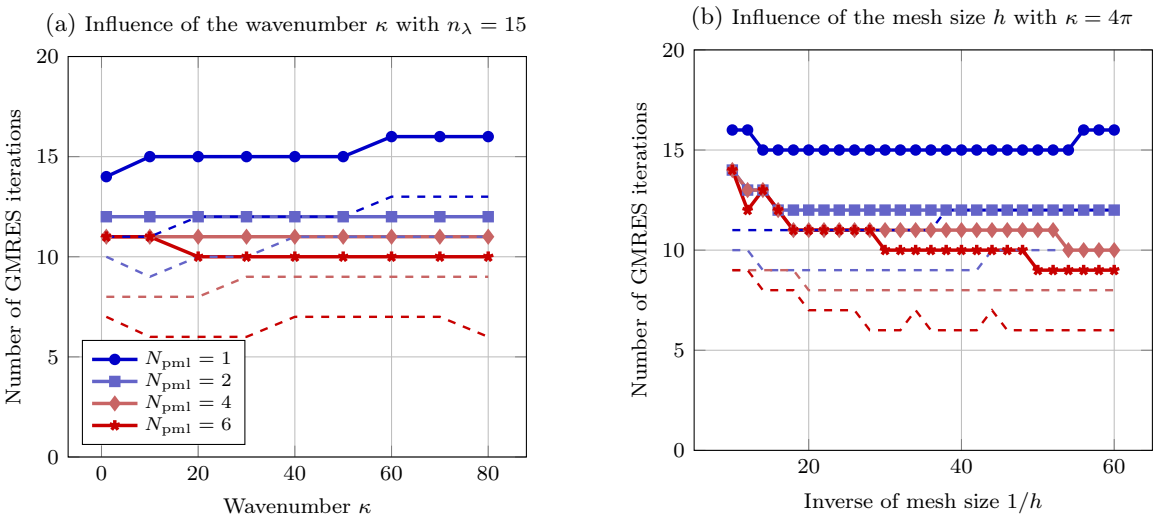

Figure 3.11: Number of GMRES iterations required to reach the relative residual 10^{-6} as a function of the wavenumber κ with a constant number of point by wavelength $n_\lambda = 15$ (a) and as a function of the inverse of the characteristic mesh size $1/h$ with a fixed wavenumber $\kappa = 4\pi$ (b) Different number of layers in the PML transmission conditions have been considered with P2 elements (bold lines) and P4 elements (thin lines). Adapted from [A15].

Increasing the PML thickness in the transmission conditions accelerates the convergence of the DDM process up to a particular point where it does not change the convergence anymore.

With both discretization techniques, there is a sharp decay of the residual and the L_2-error between the 3^{rd} and the 4^{th} iterations. This can be interpreted by considering that, at each iteration, information are transferred only between neighboring subdomains. Given the position of the source in the domain partition, four iterations are required to propagate the signal across all the subdomains. Because PML transmission conditions are particularly well-suited for this benchmark, the DDM solution is very close to the physical solution after only four iterations. These results are very similar to those obtained with the HABC transmission conditions and the cross-point treatment presented in Section 3.2.

The results obtained with the continuous and discontinuous Lagrange multipliers are similar. From the point of view of the number of DOFs, the discontinuous discretization is slightly more expensive. In the remaining of this section, we only consider the continuous discretization.

Influence of the simulation parameters. The influence of the different parameters of the simulation have been studied by modifying them one by one. We have done the following observations.

Influence of the wavenumber κ and the finite element discretization. The PML transmission conditions are efficient for high-frequency problems, as soon as the layers are sufficiently thick. Indeed, we observe on Figure 3.11 that the number of iterations slightly increases with the κ and $1/h$ for very thin PMLs (i.e. with only one or two mesh cells in the thickness), but it remains very stable for thick PMLs. The results are similar for second and fourth degree basis functions.

Influence of the absorbing function of the PML transmission conditions. When the PML is used at the exterior boundary of a truncated domain, the accuracy of the solution depends on the absorbing function. In [A15], we have compared PML transmission conditions with the quadratic function σ_{q}, the hyperbolic function σ_{h} and the shifted hyperbolic function σ_{hs} as absorbing function. We have observed that the convergence is faster with σ_{h} and σ_{sh} than with σ_{q} for one-cell PMLs (for the selected parameter σ_{q}), and the different absorbing functions provide similar results for thick PMLs.

Influence of the number of subdomains. The weak scaling of the method has been studied in [A15] by increasing the number of subdomains in each Cartesian direction. We have observed that the number of iterations increases linearly with the number of subdomains in each direction, which is expected for a

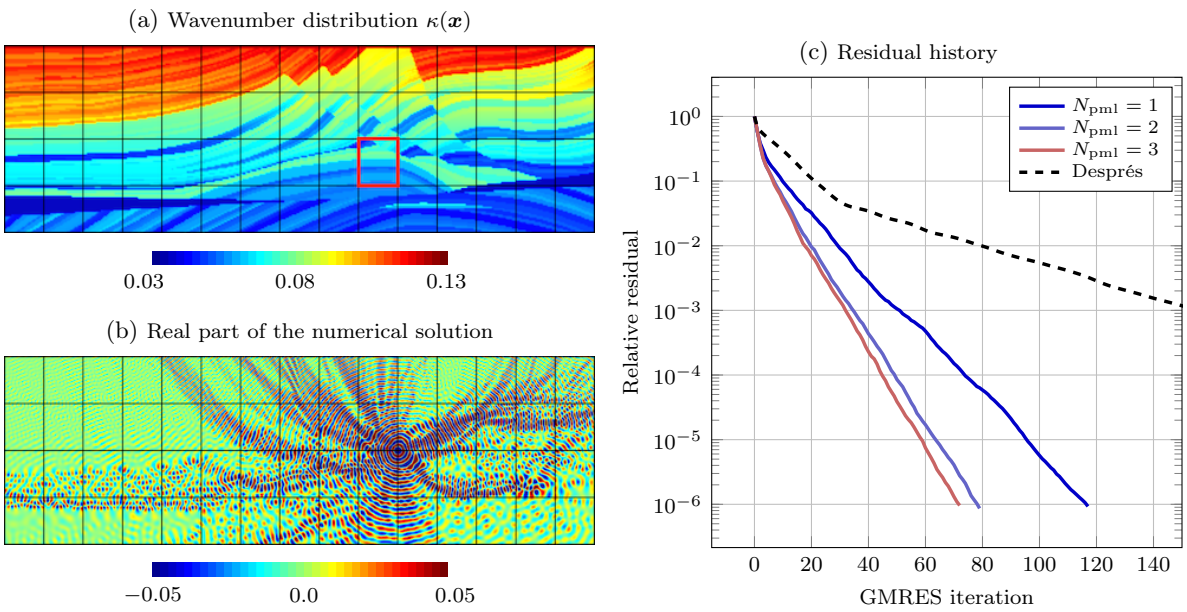

Figure 3.12: Marmousi benchmark: (a) wavenumber distribution, (b) numerical solution and (c) residual history. *Parameters: frequency $f = 30$Hz, rectangular finite elements with first-degree polynomial basis functions, characteristic mesh size $h \approx 10$ m.* Adapted from [A15].

DDM without global exchange.

Experiments with heterogeneous media. The DDM procedure with PML transmission conditions has been tested with a spatially varying medium, though it is a priori designed for problems with a constant wavenumber. We have considered the Marmousi model (Figure 3.12a) on a rectangular domain Ω is surrounded with PMLs. The spatially varying wavenumber is given by $\kappa(\boldsymbol{x}) = 2\pi f/\nu(\boldsymbol{x})$ with the velocity map $\nu(\boldsymbol{x})$ and the frequency f. The equation $-\Delta u - \kappa(\boldsymbol{x})^2 u = \delta(\boldsymbol{x} - \boldsymbol{x}_{\text{s}})$ is solved on Ω, where δ is the Dirac delta function and $\boldsymbol{x}_{\text{s}}$ is the position of a source point.

The domain is partitioned into a checkerboard grid of 15×4 subdomains (Figure 3.12a), and the finite element solution is computed by using a structured mesh of rectangular elements with first-degree polynomial basis functions on each subdomain. The source term is placed at a cross-point (Figure 3.12b). The method is tested with PML thicknesses equal to $N_{\text{pml}} = 1$, 2 and 3 mesh cells in the transmission conditions, and equal to $N_{\text{pml}} = 6$ for the exterior boundary condition. Because the wavenumber is not constant, a strategy must be chosen to define the wavenumber in the PMLs. Inside the edge PMLs, the value of the wavenumber is simply extruded from the interface with the subdomain, then it does not vary in the normal direction. Inside the corner PMLs, the wavenumber is constant, equal to the value at the corresponding corner of the subdomain.

The convergence history for the relative residual is shown on Figure 3.12c. In all the cases, the final relative L^2-error between the DDM solution and the reference numerical solution is close to 10^{-6}. As for the cases with a constant κ, we observe that the convergence if the iterative procedure is faster with the PML transmission conditions than with the standard impedance transmission conditions. Increasing the thickness of the PML accelerate the convergence, but the efficiency is not much better when increasing the thickness from $N_{\text{pml}} = 2$ to 3. The behavior of the PML transmission for this benchmark is very similar to the one reported with HABC transmission conditions.

3.4 Multi-directional sweeping preconditioning

The contribution is the result of a collaboration with R. Dai, X. Geuzaine and J.-F. Remacle, in the framework of the doctoral research of R. Dai. It corresponds to the article [A4]. The numerical results have been obtained by R. Dai with a dedicated `C` code.

We have proposed and studied multidimensional sweeping preconditioning techniques for DDMs with checkerboard domain partition. The preconditioning matrices are applied to the reduced system obtained with the non-overlapping DDMs with HABC transmission and cross-point treatment presented in Section 3.2.

For 1D domain partitions, such as partitions in layers or onion skins, the global matrix can be written as a block tridiagonal matrix. This particular structure has been used to propose 1D sweeping preconditioners, see Section 3.1.3. In [A4], we have extended some of these sweeping preconditioners for checkerboard domain partitions by using specific numbering systems for the subdomains, and by rewriting the global matrix as a block tridiagonal matrix. These strategies can be interpreted as sweeping in multiple directions (e.g. Cartesian or diagonal directions), in sequence, in parallel or in alternation. It can be related to works on L-sweeps preconditioners [274] and diagonal sweeps [211] proposed for the polarized traces method and the source transfer method, respectively.

3.4.1 Description of the preconditioning methods

To describe the methods, we consider the DDM with basic ABC transmission conditions (presented in Section 3.1.1) for the Helmholtz equation on a rectangular domain with a checkerboard domain partition. The method can be easily extended to DDMs with HABC or PML transmission conditions.

The matrix form of the reduced problem (3.1.4) is denoted by

$$\mathbf{F}\mathbf{g} := (\mathbf{I} - \mathbf{T})\mathbf{g} = \mathbf{b}, \tag{3.4.1}$$

with the set of all the transmission variables $\mathbf{g}$, the identity matrix $\mathbf{I}$, the iteration matrix $\mathbf{T}$, and the source term $\mathbf{b}$. The transmission variables are associated with the interfaces between the subdomains, i.e. the edges of the domain partition. We seek a preconditioning matrix for the global matrix $\mathbf{F}$.

Algebraic structure of the transmission problem. The global matrix $\mathbf{F}$ can be represented as a $N_{\text{dom}} \times N_{\text{dom}}$ sparse block matrix, where each block corresponds to the coupling between the unknowns associated with two subdomains. The abstract system (3.4.1) can then be rewritten as

$$\sum_{J=1}^{N_{\text{dom}}} \mathbf{F}_I^J \mathbf{g}_J = \mathbf{b}_I, \quad I = 1 \dots N_{\text{dom}},$$

where the vectors $\mathbf{g}_I$ and $\mathbf{b}_I$ contain the transmission variables and the source terms, respectively, for Ω_I, and the matrix $\mathbf{F}_I^J$ corresponds to a coupling between the transmission variables of Ω_I and Ω_J.

To be more specific, if Ω_I and Ω_J are neighboring subdomains, applying $\mathbf{F}_I^J$ on a vector $\mathbf{v}_J$ corresponds to solving the subproblem defined on Ω_I with the transmission data contained in $\mathbf{v}_J$, and computing the transmission data $\mathbf{v}_I := \mathbf{F}_I^J \mathbf{v}_J$ associated with Ω_I. If Ω_I and Ω_J are not neighbors, the block $\mathbf{F}_I^J$ is a zero matrix because there is no direct coupling between the corresponding transmission variables. The size of $\mathbf{g}_I$ and $\mathbf{b}_I$ depends on the number of interior edges for Ω_I. The block $\mathbf{F}_I^J$ can then be rectangular if the subdomains Ω_I and Ω_J have different numbers of interior edges. The blocks are sparse, see [A4].

With 1D domain partitions, the global matrix is block tridiagonal if the neighboring subdomains are numbered in a consecutive order. With checkerboard partitions, there are at most four off-diagonal blocks in each line and each column of the global block matrix, because there are at most four neighboring subdomains for each subdomain. Nevertheless, a block tridiagonal structure can be recovered.

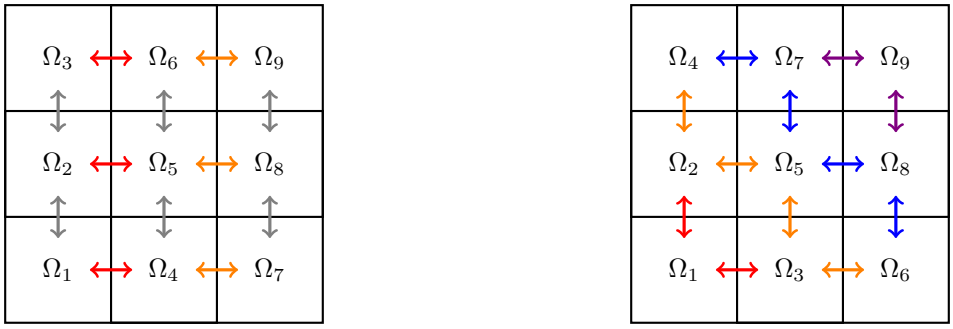

(a) Numbering by column (b) Numbering by diagonal

Figure 3.13: Two numbering systems for the subdomains with a 3×3 checkerboard domain partition. The colored arrows indicate interactions between groups of subdomains. Adapted from [A4].

The proposed sweeping preconditioners are based on numbering systems by column and by diagonal, which are illustrated in Figure 3.13 for a 3×3 checkerboard partition of the domain. For these numbering systems, the reduced system can be represented as

$$\begin{bmatrix} \mathbf{I}_1 & \mathbf{F}_1^2 & \mathbf{F}_1^4 & & & & & & \\ \mathbf{F}_2^1 & \mathbf{I}_2 & \mathbf{F}_2^3 & \mathbf{F}_2^5 & & & & & \\ & \mathbf{F}_3^2 & \mathbf{I}_3 & & \mathbf{F}_3^6 & & & & \\ \mathbf{F}_4^1 & & & \mathbf{I}_4 & \mathbf{F}_4^5 & & \mathbf{F}_4^7 & & \\ & \mathbf{F}_5^2 & & \mathbf{F}_5^4 & \mathbf{I}_5 & \mathbf{F}_5^6 & & \mathbf{F}_5^8 & \\ & & \mathbf{F}_6^3 & & \mathbf{F}_6^5 & \mathbf{I}_6 & & & \mathbf{F}_6^9 \\ & & & \mathbf{F}_7^4 & & & \mathbf{I}_7 & \mathbf{F}_7^8 & \\ & & & & \mathbf{F}_8^5 & & \mathbf{F}_8^7 & \mathbf{I}_8 & \mathbf{F}_8^9 \\ & & & & & \mathbf{F}_9^6 & & \mathbf{F}_9^8 & \mathbf{I}_9 \end{bmatrix} \begin{bmatrix} \mathbf{g}_1 \\ \mathbf{g}_2 \\ \mathbf{g}_3 \\ \mathbf{g}_4 \\ \mathbf{g}_5 \\ \mathbf{g}_6 \\ \mathbf{g}_7 \\ \mathbf{g}_8 \\ \mathbf{g}_9 \end{bmatrix} = \begin{bmatrix} \mathbf{b}_1 \\ \mathbf{b}_2 \\ \mathbf{b}_3 \\ \mathbf{b}_4 \\ \mathbf{b}_5 \\ \mathbf{b}_6 \\ \mathbf{b}_7 \\ \mathbf{b}_8 \\ \mathbf{b}_9 \end{bmatrix} \quad \text{and} \quad \begin{bmatrix} \mathbf{I}_1 & \mathbf{F}_1^2 & \mathbf{F}_1^3 & & & & & & \\ \mathbf{F}_2^1 & \mathbf{I}_2 & & \mathbf{F}_2^4 & \mathbf{F}_2^5 & & & & \\ \mathbf{F}_3^1 & & \mathbf{I}_3 & & \mathbf{F}_3^5 & \mathbf{F}_3^6 & & & \\ & \mathbf{F}_4^2 & & \mathbf{I}_4 & & & \mathbf{F}_4^7 & & \\ & \mathbf{F}_5^2 & \mathbf{F}_5^3 & & \mathbf{I}_5 & & \mathbf{F}_5^7 & \mathbf{F}_5^8 & \\ & & \mathbf{F}_6^3 & & & \mathbf{I}_6 & & \mathbf{F}_6^8 & \\ & & & \mathbf{F}_7^4 & \mathbf{F}_7^5 & & \mathbf{I}_7 & & \mathbf{F}_7^9 \\ & & & & \mathbf{F}_8^5 & \mathbf{F}_8^6 & & \mathbf{I}_8 & \mathbf{F}_8^9 \\ & & & & & & \mathbf{F}_9^7 & \mathbf{F}_9^8 & \mathbf{I}_9 \end{bmatrix} \begin{bmatrix} \mathbf{g}_1 \\ \mathbf{g}_2 \\ \mathbf{g}_3 \\ \mathbf{g}_4 \\ \mathbf{g}_5 \\ \mathbf{g}_6 \\ \mathbf{g}_7 \\ \mathbf{g}_8 \\ \mathbf{g}_9 \end{bmatrix} = \begin{bmatrix} \mathbf{b}_1 \\ \mathbf{b}_2 \\ \mathbf{b}_3 \\ \mathbf{b}_4 \\ \mathbf{b}_5 \\ \mathbf{b}_6 \\ \mathbf{b}_7 \\ \mathbf{b}_8 \\ \mathbf{b}_9 \end{bmatrix},$$

respectively, where $\mathbf{I}_I$ is the identity matrix associated with the subdomain Ω_I. The colors correspond to the interactions between subdomains represented in Figure 3.13. With the numbering by column, the global matrix can be rewritten as a 3×3 block tridiagonal matrix, where the large blocks on the diagonal (resp. off the diagonal) correspond to interactions between subdomains of a given column (resp. of two different columns). With the numbering by diagonal, the matrix of the system can also be written as a block tridiagonal matrix with large blocks corresponding to interactions between subdomains belonging to two diagonals of the domain partition. By contrast with the other numbering system, the blocks on the diagonal are identity matrices because subdomains belonging to the same group are never neighbors.

With both numbering systems, the global system can be represented with a block tridiagonal matrix. For convenience, we introduce the general representation

$$\begin{bmatrix} \mathbf{F}_{[1]}^{[1]} & \mathbf{F}_{[1]}^{[2]} & & & \\ \mathbf{F}_{[2]}^{[1]} & \mathbf{F}_{[2]}^{[2]} & \mathbf{F}_{[2]}^{[3]} & & \\ & \mathbf{F}_{[3]}^{[2]} & \mathbf{F}_{[3]}^{[3]} & \mathbf{F}_{[3]}^{[4]} & \\ & & \mathbf{F}_{[4]}^{[3]} & \mathbf{F}_{[4]}^{[4]} & \mathbf{F}_{[4]}^{[5]} \\ & & & \mathbf{F}_{[5]}^{[4]} & \mathbf{F}_{[5]}^{[5]} \end{bmatrix} \begin{bmatrix} \mathbf{g}_{[1]} \\ \mathbf{g}_{[2]} \\ \mathbf{g}_{[3]} \\ \mathbf{g}_{[4]} \\ \mathbf{g}_{[5]} \end{bmatrix} = \begin{bmatrix} \mathbf{b}_{[1]} \\ \mathbf{b}_{[2]} \\ \mathbf{b}_{[3]} \\ \mathbf{b}_{[4]} \\ \mathbf{b}_{[5]} \end{bmatrix}, \tag{3.4.2}$$

where the vectors $\mathbf{g}_{[I]}$ and $\mathbf{b}_{[I]}$ are associated with one group of subdomains and each block $\mathbf{F}_{[I]}^{[J]}$ corresponds to the coupling between the transmission variables of two groups. The groups of subdomains, corresponding to columns or diagonals of subdomains in Figure 3.13, are denoted by $\Omega_{[S]}$, with $S = 1 \dots N_{\text{gr}}$.

Symmetric Gauss-Seidel (SGS) preconditioner. This technique consists in applying the Gauss-Seidel preconditioner forward and backward successively [260]. The preconditioning matrix is

$$\mathbf{P}_{\mathrm{SGS}} = (\mathbf{D} + \mathring{\mathbf{L}})\mathbf{D}^{-1}(\mathbf{D} + \mathring{\mathbf{U}}),$$

where $\mathbf{D}$, $\mathring{\mathbf{L}}$ and $\mathring{\mathbf{U}}$ are respectively the diagonal part, the strictly lower triangular part and the strictly upper triangular part of the block matrix $\mathbf{F}$ represented in equation (3.4.2).

Assuming that there is no coupling between subdomains of the same group, the diagonal part is an identity matrix, i.e. $\mathbf{D} = \mathbf{I}$, and the preconditioning matrix can then be rewritten as

$$\mathbf{P}_{\mathrm{SGS}} = \mathbf{L}\mathbf{U} = \begin{bmatrix} \mathbf{I} & & & & \\ \mathbf{F}^{[1]}_{[2]} & \mathbf{I} & & & \\ & \mathbf{F}^{[2]}_{[3]} & \mathbf{I} & & \\ & & \ddots & \ddots & \\ & & & \mathbf{F}^{[N_{\mathrm{gr}}-1]}_{[N_{\mathrm{gr}}]} & \mathbf{I} \end{bmatrix} \begin{bmatrix} \mathbf{I} & \mathbf{F}^{[2]}_{[1]} & & & \\ & \mathbf{I} & \mathbf{F}^{[3]}_{[2]} & & \\ & & \ddots & \ddots & \\ & & & \mathbf{I} & \mathbf{F}^{[N_{\mathrm{gr}}]}_{[N_{\mathrm{gr}}-1]} \\ & & & & \mathbf{I} \end{bmatrix}.$$

To use this preconditioner, the inverse of $\mathbf{L}$ and $\mathbf{U}$ could be computed explicitly, but it is not necessary. In fact, applying $\mathbf{L}^{-1}$ on any vector $\mathbf{r}$ corresponds to solving the local problems associated with the subdomains of each group by following the numbering of the groups. The local problems associated with $\Omega_{[1]}$ are solved in the first step by using the transmission data contained in $\mathbf{r}$, then the local problems associated with $\Omega_{[2]}$ are solved by using the updated data, and so on. Similarly, applying $\mathbf{U}^{-1}$ corresponds to solving the local problems in the decreasing order of the groups, i.e. from $\Omega_{[N_{\mathrm{gr}}]}$ to $\Omega_{[1]}$.

The SGS preconditioner can then be interpreted as a forward sweep followed by a backward sweep, where information is propagated forward and backward in the domain partition at each application. This strategy is very close to the 1D sweeping techniques considered e.g. in [233, 270, 290]. The direction of the sweep is determined by the numbering system. Numbering systems by column and by diagonal result in horizontal and diagonal sweeps, respectively. Note that, with the numbering by column, the blocks on the diagonal are not identity matrices, and then $\mathbf{D} \neq \mathbf{I}$. Therefore, the interactions between subdomains of the same column are ignored with this approach.

Parallel Double Sweep (DS) preconditioner. In the approach, the matrices $\mathbf{L}$ and $\mathbf{U}$ are modified in so that they commute. The forward and backward sweeps can then be performed in parallel, reducing the runtime per iteration by a factor of two in parallel environments. The preconditioning matrix is

$$\mathbf{P}_{\mathrm{DS}} = \widetilde{\mathbf{L}}\,\widetilde{\mathbf{U}} = \widetilde{\mathbf{U}}\,\widetilde{\mathbf{L}},$$

where $\widetilde{\mathbf{L}}$ and $\widetilde{\mathbf{U}}$ are modified versions of $\mathbf{L}$ and $\mathbf{U}$. To remove the dependencies between $\mathbf{L}$ and $\mathbf{U}$, the blocks are modified so that, for any group $\Omega_{[S]}$, the forward sweep (resp. the backward sweep) does not use transmission data of the edges shared with the subdomains of $\Omega_{[S+1]}$ (resp. $\Omega_{[S-1]}$). Depending on the sweeping direction, transmission data are simply cancelled to remove dependencies.

Combination of sweeping directions. In the SGS and DS sweeping preconditioning strategies, the sweeps are performed forward/backward in only one direction. In practice, it may be advantageous to combine different directions in order to propagate information faster to different zones of the computational domain. This can be achieved thanks to the Flexible GMRES *(FGMRES)* [259, 260], where a different preconditioning strategy can be used at each iteration.

Discussion of parallelization strategies. With the SGS preconditioner (resp. the DS preconditioner), the forward and backward sweeps are sequential operations (resp. parallel operations). For both preconditioners, the solution of the local problems associated with the subdomains of each group can be performed in parallel, because we have assumed that the dependencies between these subdomains

were ignored. In distributed-memory parallel environments, the placement of the subdomains raises new questions. When using diagonal sweeps, it can be advantageous to place one row of subdomains on each processor. In [A4], this question has not been investigated further, and the results have been obtained only in shared-memory parallel environments. Strategies to improve the parallel efficiency have been discussed in [290] for 1D domain partitions. Placement strategies have been discussed in [274] for L-sweeps preconditioners with checkerboard domain partitions.

3.4.2 Computational results

A first intuitive result. We consider the scattering of a plane wave $u_{\text{inc}}(\boldsymbol{x}) = e^{\imath\kappa x}$ by a sound-soft disk, placed in the middle of a square computational domain Ω. The Dirichlet boundary condition is prescribed on the boundary of the disk. The Padé-type HABC is prescribed on the exterior border of the square domain with the compatibility conditions at the corners. The computational domain is partitioned into 5×5 square subdomains, the DDM with HABC transmission is used with the cross-point treatment, and the resulting interface system is solved by using GMRES or FGMRES with the sweeping preconditioning techniques. The solution is computed by using a standard high-order finite element method on meshes made of triangles and generated with `Gmsh` [142]. The results have been obtained with a dedicated `C` code (`https://gitlab.com/ruiyang/ddmwave`).

Figure 3.14 shows snapshots of the solutions after the first iterations with the SGS and DS preconditions and different sweeping directions. After the very first iteration, the zone of influence of the source corresponds to the subdomains that are mainly along the sweeping direction, starting from the center of the domain. In Figure 3.14b, the subdomains at the right-up and left-down corners cannot be reached by the source after the first iteration, because the forward and backward diagonal sweeps are performed independently with the DS preconditioner. In contrast, with the SGS preconditioner, these subdomains can be reached during the backward sweep, which is performed after the forward sweep (Figure 3.14a).

For the diagonal sweeps, four iterations are required to obtain an accurate solution in all the subdomains with the DS preconditioner, while only two iterations are required with the SGS preconditioner. For the horizontal sweeps, three iterations are required with both preconditioners (Figures 3.14c and 3.14d). An accurate solution is obtained after two iterations with both preconditions when FGMRES is used with the alternating diagonal sweeps (Figures 3.14e and 3.14f). These observations are confirmed by comparing the residual histories with P1 and P7 finite elements (not shown here, see [A4]).

Influence of the simulation parameters. The benchmark is modified by placing two scattering disks in the middle of the lower left and lower right subdomains (see Figure 3.15a). This case is slightly more complicated than the previous one because of the multiple reflections between the two disks. By default, the parameters are the same as before.

Influence of the number of subdomains. We have studied the weak scaling of the preconditioning strategies by performing the simulation on square domains of increasing size, with checkerboard partitions of $\mathrm{N}_{\mathrm{dom},x} \times \mathrm{N}_{\mathrm{dom},y}$ square subdomains for $\mathrm{N}_{\mathrm{dom},x} = \mathrm{N}_{\mathrm{dom},y} = 4$, 8, 12, 16 and 20. In all the cases, the size of all the subdomains is always 2.5×2.5, and the scattering objects are placed in the center of the lower left and lower right subdomains. We observe in Figure 3.15b that the SGS and DS preconditioners do not scale with the fixed diagonal and horizontal sweep directions. The number of iterations to reach the relative residual 10^{-6} increases with the number of the subdomains per direction, but the increase is slower than without preconditioning (bold black line). In contrast, the method scale for both preconditioners when FGMRES is used with the alternating diagonal sweeping directions. This is mainly due to the position of the scattering disks: each diagonal direction is well suited to one of the disks.

Influence of the wavenumber κ. Without preconditioner, we have observed that the DDM with HABC transmission conditions remains efficient for high-frequency scattering problems with a single scattering object (see Section 3.2.2), provided that the HABC parameters are well chosen. In [A4], we have studied the influence of κ, varying from 5 to 25, for a given mesh density. We did not observe any significant effect of κ on the convergence with the different preconditioning strategies.

(a) Diagonal sweeps – GMRES with SGS preconditioner

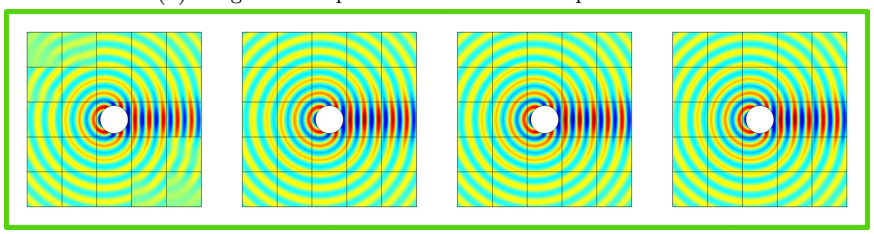

(b) Diagonal sweeps – GMRES with DS preconditioner

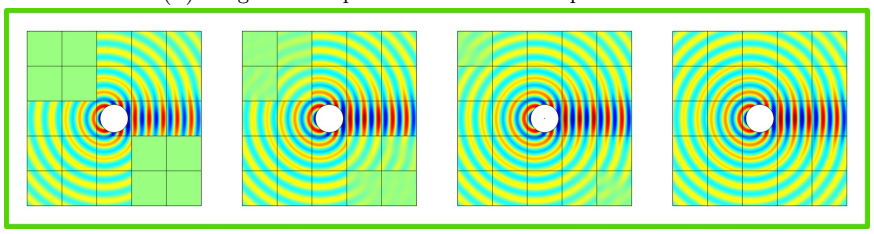

(c) Horizontal sweeps – GMRES with SGS preconditioner

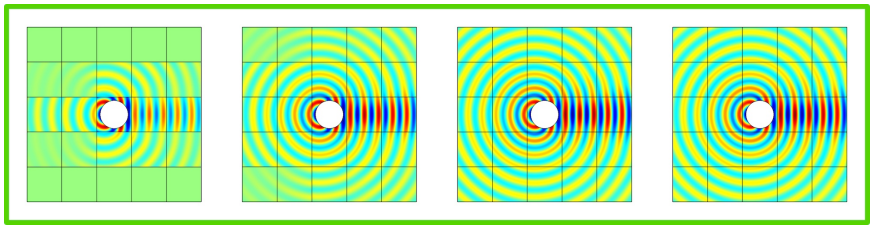

(d) Horizontal sweeps – GMRES with DS preconditioner

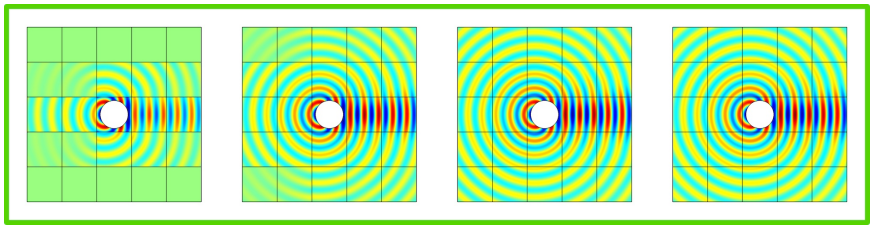

(e) Alternating diagonal sweeps – FGMRES with SGS preconditioner

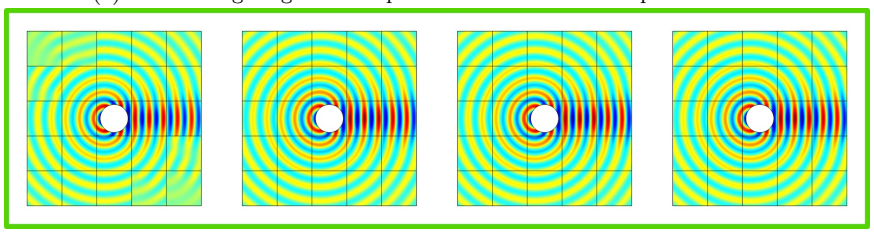

(f) Alternating diagonal sweeps – FGMRES with DS preconditioner

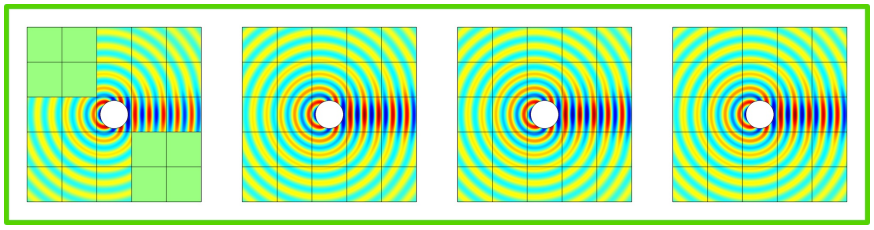

Figure 3.14: Benchmark with one obstacle. Solution after 1, 2, 3 and 4 (F)GMRES iterations with different preconditioning strategies: diagonal sweeps (from lower left to upper right, then vice versa), horizontal sweeps (to the right, then to the left), alternating diagonal sweeps with FGMRES (between lower left and upper right, and between upper left and lower right, in alternance). *Parameters: radius of disk* $R = 1$, *size of subdomain* $= 2.5 \times 2.5$, *HABC parameters* $N = 8$ *and* $\phi = \pi/3$ *for both boundary and transmission conditions, wavenumber* $\kappa = 2\pi$, *P1 elements, characteristic mesh size* $h = 1/20$. Reproduced from [A4].

(a) Configuration for the 5×5 domain partition

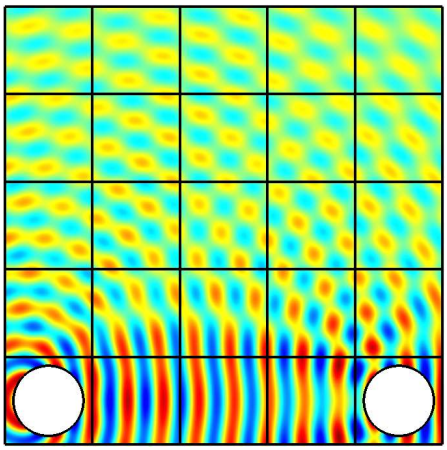

(b) Influence of the number of subdomains per direction

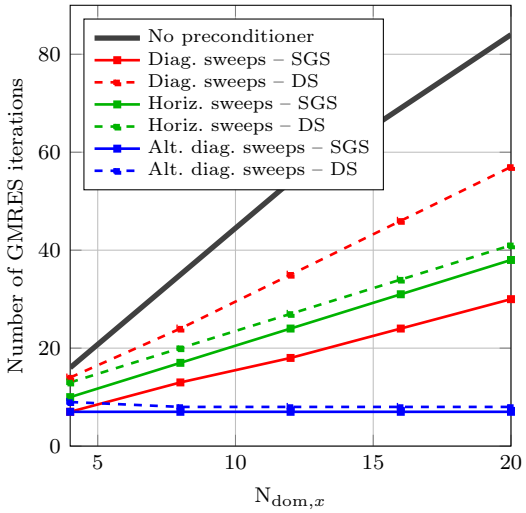

Figure 3.15: Benchmark with two obstacles. Solution for the 5×5 domain partition *(left)* and number of (F)GMRES iterations to reach the relative residual 10^{-6} as a function of the number of subdomains per direction with the different preconditioning strategies *(right)*. *Parameters: See legend of Figure 3.14.* Adapted from [A4].

(a) Configuration

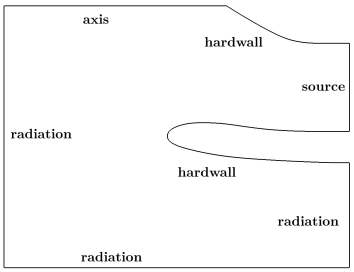

(b) Numerical solution

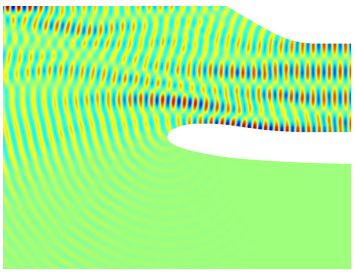

(c) Domain partition

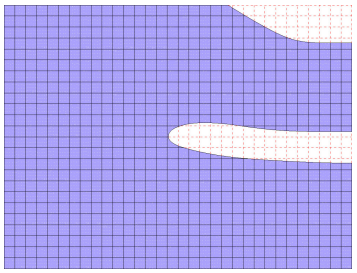

Figure 3.16: Benchmark *"turbofan intake"*. Geometry and boundary conditions *(a)*, numerical solution *(b)* and the domain partition for the 24×32 configuration *(c)*. *Parameters:* P5 *finite elements, HABC operators with* $N = 4$ *and* $\phi = \pi/3$ *for both interior and boundary edges.* Reproduced from [A4].

Illustrative example with a non-rectangular domain. Our approach can be applied to computational domains that are not rectangular. To illustrate this, we have considered the geometry shown in Figure 3.16a, which represents the cylindrical duct of a generic turbofan intake. The 2D Helmholtz equation is solved in the computational domain, with a sinusoidal non-homogeneous Dirichlet boundary condition at the interior of the turbofan, and a Padé-type HABC on the artificial boundaries.

Since the domain is not rectangular and our approach is a priori designed for checkerboard domain partitions, additional steps are required. The domain partition is performed for a rectangular region containing the computational domain, and the solution procedure is performed by iterating over all subdomains. Several subdomains are partially or completely outside the computational domain. There are fewer or no unknowns associated with these subdomains. Therefore, the code developed for checkerboard partitions can be easily applied to this case.

The different preconditioning strategies have been compared in [A4] from the point of view of both the number of iterations (to reach a given relative residual) and the runtime (in a shared-memory parallel environment). We have observed that all the preconditioning strategies with fixed sweeping directions reduce the number of iterations, but the runtime is sometimes higher due to the inner steps of these preconditioners at each iteration. Nevertheless, for many subdomains, FGMRES with the alternating diagonal sweeping performs the best, reducing both the number of iterations and the runtime.

Chapter 4

Discontinuous finite element solvers

In this chapter, we consider *discontinuous Galerkin* (DG) finite element methods, as an alternative to the conforming Galerkin methods with continuous basis functions. In DG schemes, the numerical solution and the test functions are discontinuous at the interfaces between the elements, and the continuity of the solution at the interfaces is weakly enforced thanks to interface terms involving numerical fluxes in the variational formulation. This approach provides some flexibility in the choice of interface terms and basis functions.

The DG methods have a tremendous success for time-dependent wave propagation problems. With explicit time-stepping schemes, the algorithmic procedures require intensive local element-wise operations and limited memory storage, which is well suited for efficient parallel computing on modern computers. In addition, the degrees of freedom (DOFs) are associated only with elements, and they can be linearly indexed in memory, allowing for efficient parallel implementations on modern parallel computer architectures, including clusters with GPUs, see e.g. [176, 198, A13, A14]. However, for time-harmonic problems, the DG methods still lead to large sparse ill-conditioned systems, which are difficult to solve. Today, the research about DG methods for time-harmonic problems is very active, including developments on improved formulations, non-standard basis functions and accelerated iterative solvers.

This chapter is related to the JCJC ANR project *"WavesDG"*, which is still in progress. In *WavesDG*, we investigate accelerated iterative DG finite element solvers for time-harmonic problems. By building the DG solver with wave-specific strategies at all the levels, we seek to improve the properties of the resulting algebraic system in order to speed up the iterative solution procedures in parallel environments.

In the first contribution of the project [A6], we have proposed a new hybridization strategy for a standard DG scheme based on upwind fluxes. Compared to the standard DG scheme and the standard *hybridizable discontinuous Galerkin* (HDG) scheme, the iterative procedures converge with a smaller number of iterations with the new approach, which we called the *"CHDG method"*. The first letter corresponds to the *"C"* of characteristic variables, which play a key role in our approach.

An overview of DG methods for Helmholtz problems is proposed in Section 4.1, with a description of the standard DG and HDG methods with upwind fluxes. My contribution to this topic, corresponding to [A6], is presented in Section 4.2. The current work and perspectives related to *WavesDG* are presented in Chapter 5.

4.1 Overview of DG methods for Helmholtz problems

4.1.1 A rapid survey of DG formulations and computational strategies

The first *discontinuous Galerkin* (DG) method was proposed in 1973 by Reed and Hill [253] to solve steady-state neutron transport problems. It was then rapidly extended and studied for a wide range of PDE problems, see for example the reference books [81, 176, 255, 102] and the review articles [13, 78]. The DG framework offers more flexibility than the continuous methods because many basis functions, and many interface treatments are possible. High-order polynomial basis functions are very easily handled, which limits the dispersion errors that occur when considering high-frequency problems [187, 4], and non-polynomial functions can also be used.

Many DG formulations have been proposed for time-harmonic problems, and a comprehensive review would be complicated. Below we describe some of the main approaches and computational strategies.

IPDG formulations. In the *interior penalty discontinuous Galerkin* (IPDG) method, the main unknown of the formulations corresponds to the scalar field governed by the Helmholtz equation. The variational formulations are obtained using the standard Galerkin approach, similarly to the continuous Galerkin methods, but the grad-grad term is defined element per element, and penalty terms are introduced at the interfaces between the elements to ensure consistency and stability. The IPDG method has been initially proposed by Arnold [12] for parabolic problems. Formulations have been derived and analyzed for the Helmholtz equation [5, 217, 123, 124, 182, 227]. Similar formulations have been studied for the time-harmonic Maxwell equations, see e.g. [247, 183], with a vector field as the main unknown, and a curl-curl term on each element in the variational formulations.

Hybridized DG formulations. Mixed DG formulations are obtained by introducing an additional vector field corresponding to the gradient of the scalar field, or by first rewriting the Helmholtz equation as a first-order PDE system, such as the pressure-velocity system. In fact, for time-dependent problems, many formulations have been derived from first-order PDE systems, inspired by the literature on the finite volume methods [283]. In particular, DG formulations with upwind fluxes are widely used [176, 193]. For time-harmonic problems, this approach introduces additional unknowns, which can increase the size of the algebraic system to be solved, but the system can be reduced thanks to the *hybridization* strategy.

In the *hybridized discontinuous Galerkin* (HDG) methods, the physical unknowns associated to different elements are decoupled by introducing additional unknowns at the interface between the elements. Depending on the method, these additional unknowns can be interpreted as Lagrange multipliers or numerical fluxes. The physical unknowns are then removed from the system by solving local element-wise problems. This strategy is related to the static condensation, and leads to a reduced system with unknowns defined only on the skeleton of the mesh, i.e. on the faces of the elements.

The HDG approach [80] was first proposed for coercive problems, and has been widely studied in the last two decades, see e.g. the review articles [77, 78]. HDG formulations have been proposed and analyzed more specifically for Helmholtz problems e.g. in [229, 157, 65, 90]. Several extensions for different wave propagation models have been studied e.g. in [236, 237, 143, 212, 153, 25].

The standard DG method with upwind fluxes and the related HDG method for the Helmholtz equation are described in Sections 4.1.2 and 4.1.3, respectively.

DPG formulations. In the *discontinuous Petrov-Galerkin* (DPG) methods, the spaces of the trial and test functions are different. DPG formulations have been studied for time-harmonic problems in [96, 248].

Trefftz and wave-based methods. In Trefftz methods, the trial and test functions are local solutions of the target equations. They are popular for time-harmonic problems because the approximation spaces contain oscillating basis functions and can achieve better approximation properties than classical polynomials, see e.g. [179].

Plane-wave basis functions are often considered in Trefftz DG methods because the linear systems are easy to construct, and the wave directions can be optimized with physical considerations. Cessenat and Després [60] proposed a method based on the *ultra-weak variational formulation* (UWVF) of the Helmholtz problems with plane-wave basis functions, which was studied and extended in [186, 61, 144]. Plane-wave basis functions have also been used in DG formulations based on Lagrange multipliers [279] and upwind fluxes [128]. However, conditioning and stability problems can arise with plane-wave basis functions [179]. Numerical strategies to reduce these problems have been studied in [21, 246]. Many other approaches, such as the use of phase-based basis functions [238], evanescent basis functions [243] and BEM formulations inside each element [22], have also been proposed. To deal with spatially varying coefficients, basis functions based on approximate local solutions are also investigated e.g. in [188].

Many other approaches with wave-based basis functions have been proposed. For example, in [119], the standard polynomial space is enriched with plane waves in a DG formulation. For a more complete survey, we refer to the review article by Hiptmair, Moiola and Perugia [179].

Combinations with DDMs. DDMs are usually developed and tested with standard finite difference schemes and continuous finite element schemes, but they can also be applied to DG schemes. Several combinations have been proposed for time-harmonic problems. In [186, 11], additive Schwarz preconditioners is applied to Trefftz DG schemes with plane-wave basis functions. A DG scheme based on Lagrange multipliers was combined with a FETI DDM in [122]. A non-overlapping DDM with impedance-type transmission conditions is combined with a DG scheme in [104] and a HDG scheme in [213, 3]. In the latter references, the same transmission condition is used for both the DDM and the DG scheme.

4.1.2 Standard DG method with upwind fluxes for Helmholtz problems

To describe the DG and HDG methods, with consider a time-harmonic scalar wave propagation problem on a Lipschitz polytopal domain $\Omega \subset \mathbb{R}^d$, with $d = 2$ or 3,

$$\begin{cases} -\imath\kappa u + \nabla\cdot\boldsymbol{q} = 0, & \text{in } \Omega, \\ -\imath\kappa\boldsymbol{q} + \nabla u = \boldsymbol{0}, & \text{in } \Omega, \\ u - \boldsymbol{n}\cdot\boldsymbol{q} = s, & \text{on } \Gamma := \partial\Omega, \end{cases} \tag{4.1.1}$$

with the unknown fields u and $\boldsymbol{q}$, the wavenumber κ (assumed to be a positive real constant), the outgoing unit normal $\boldsymbol{n}$, and a given boundary data $s(\boldsymbol{x})$ defined on Γ.

Mesh, approximation spaces and notations. We consider a conforming mesh $\mathcal{T}_h$ of the domain Ω consisting of simplicial elements K. The set of element boundaries is denoted by $\partial\mathcal{T}_h := \{\partial K \,|\, K \in \mathcal{T}_h\}$. The set of faces of the mesh is denoted by $\mathcal{F}_h$, and the set of faces of an element K is denoted by $\mathcal{F}_K$.

The approximate fields are piecewise polynomials. For the sake of simplicity, we fix a polynomial degree $p \geq 0$ and introduce

$$V_h := \prod_{K\in\mathcal{T}_h} \mathcal{P}_p(K) \qquad \text{and} \qquad \boldsymbol{V}_h := \prod_{K\in\mathcal{T}_h} \boldsymbol{\mathcal{P}}_p(K),$$

where $\mathcal{P}_p(\cdot)$ and $\boldsymbol{\mathcal{P}}_p(\cdot)$ denote the spaces of scalar and vector complex-valued polynomials of degree smaller or equal to p. By convention, the restrictions of $u_h \in V_h$ and $\boldsymbol{u}_h \in \boldsymbol{V}_h$ on K are denoted by u_K and $\boldsymbol{u}_K$, respectively. We introduce the sesquilinear forms

$$(u,v)_K := \int_K u\overline{v}\,d\boldsymbol{x}, \qquad (\boldsymbol{u},\boldsymbol{v})_K := \int_K \boldsymbol{u}\cdot\overline{\boldsymbol{v}}\,d\boldsymbol{x}, \qquad \langle u,v\rangle_{\partial K} := \sum_{F\in\mathcal{F}_K}\int_F u\overline{v}\,d\sigma(\boldsymbol{x}),$$
$$(u,v)_{\mathcal{T}_h} := \sum_{K\in\mathcal{T}_h}(u,v)_K, \qquad (\boldsymbol{u},\boldsymbol{v})_{\mathcal{T}_h} := \sum_{K\in\mathcal{T}_h}(\boldsymbol{u},\boldsymbol{v})_K, \qquad \langle u,v\rangle_{\partial\mathcal{T}_h} := \sum_{K\in\mathcal{T}_h}\langle u,v\rangle_{\partial K}.$$

By convention, the quantities used in the surface integral $\langle\cdot,\cdot\rangle_{\partial K}$ correspond to the restriction of fields defined on K (e.g. v_K and $\boldsymbol{v}_K$) or quantities associated to the faces of K (e.g. $\boldsymbol{n}_{K,F}$ with $F \in \mathcal{F}_K$).

Standard DG formulation. The general DG formulation of system (4.1.1) reads:

$$\left|\begin{array}{l}\text{Find } (u_h, \boldsymbol{q}_h) \in V_h \times \boldsymbol{V}_h \text{ such that, for all } (v_h, \boldsymbol{p}_h) \in V_h \times \boldsymbol{V}_h,\\ \quad\begin{cases} -\imath\kappa(u_h, v_h)_{\mathcal{T}_h} - (\boldsymbol{q}_h, \nabla v_h)_{\mathcal{T}_h} + \langle \boldsymbol{n}\cdot\widehat{\boldsymbol{q}}(u_h,\boldsymbol{q}_h), v_h\rangle_{\partial\mathcal{T}_h} = 0,\\ -\imath\kappa(\boldsymbol{q}_h, \boldsymbol{p}_h)_{\mathcal{T}_h} - (u_h, \nabla\cdot\boldsymbol{p}_h)_{\mathcal{T}_h} + \langle \widehat{u}(u_h,\boldsymbol{q}_h), \boldsymbol{n}\cdot\boldsymbol{p}_h\rangle_{\partial\mathcal{T}_h} = 0,\end{cases}\end{array}\right. \tag{4.1.2}$$

where $\widehat{u}(u_h, \boldsymbol{q}_h)$ and $\boldsymbol{n}\cdot\widehat{\boldsymbol{q}}(u_h, \boldsymbol{q}_h)$ are the *numerical fluxes*. The properties of the DG formulation depend strongly on the choice of the numerical fluxes. In this work, we consider the *upwind fluxes* defined as

$$\begin{cases} \widehat{u}_F := (u_K + u_{K'})/2 + \boldsymbol{n}_{K,F}\cdot(\boldsymbol{q}_K - \boldsymbol{q}_{K'})/2,\\ \boldsymbol{n}_{K,F}\cdot\widehat{\boldsymbol{q}}_F := \boldsymbol{n}_{K,F}\cdot(\boldsymbol{q}_K + \boldsymbol{q}_{K'})/2 + (u_K - u_{K'})/2,\end{cases} \quad \text{if } F \notin \Gamma, \tag{4.1.3a}$$

$$\begin{cases} \widehat{u}_F := (u_K + \boldsymbol{n}_{K,F}\cdot\boldsymbol{q}_K + s)/2,\\ \boldsymbol{n}_{K,F}\cdot\widehat{\boldsymbol{q}}_F := (u_K + \boldsymbol{n}_{K,F}\cdot\boldsymbol{q}_K - s)/2,\end{cases} \quad \text{if } F \subset \Gamma. \tag{4.1.3b}$$

For an interior face $F \notin \Gamma$, K' is the neighboring element and $\boldsymbol{n}_{K,F}$ is the unit outward normal to K on F. For a boundary face $F \subset \Gamma$ of an element K, the fluxes take the boundary condition into account. These fluxes are consistent, i.e. $\widehat{u}(u, \boldsymbol{q}) = u$ and $\boldsymbol{n}\cdot\widehat{\boldsymbol{q}}(u, \boldsymbol{q}) = \boldsymbol{n}\cdot\boldsymbol{q}$ on both interior and boundary faces.

Under standard assumptions, the method achieves the optimal convergence rate for the numerical fields u_h and $\boldsymbol{q}_h$ in L^2-norm, i.e. $p+1$ where p is the polynomial degree of the basis functions. Error estimates have been derived for HDG formulations, equivalent to the DG formulation above, for the Helmholtz problem with a Dirichlet boundary condition in [157] and a Robin boundary condition in [125, 90]. By using a post-processing, the convergence rate for u_h can be increased by one, see e.g. [79].

Origin of the upwind fluxes. Let us consider the time-domain version of the governing equations. Assuming there is no source and the fields are varying only in direction $\boldsymbol{n}$, we get

$$\begin{cases} \partial_t u + c\,\partial_n(\boldsymbol{n}\cdot\boldsymbol{q}) = 0,\\ \partial_t(\boldsymbol{n}\cdot\boldsymbol{q}) + c\,\partial_n u = 0.\end{cases}$$

A simple linear combination gives the transport equations

$$\begin{cases} \partial_t(u + \boldsymbol{n}\cdot\boldsymbol{q}) + c\,\partial_n(u + \boldsymbol{n}\cdot\boldsymbol{q}) = 0,\\ \partial_t(u - \boldsymbol{n}\cdot\boldsymbol{q}) - c\,\partial_n(u - \boldsymbol{n}\cdot\boldsymbol{q}) = 0.\end{cases}$$

Therefore, $g^{\oplus} = u + \boldsymbol{n}\cdot\boldsymbol{q}$ and $g^{\ominus} = u - \boldsymbol{n}\cdot\boldsymbol{q}$ correspond to quantities transported in the domain in directions $+\boldsymbol{n}$ (downstream) and $-\boldsymbol{n}$ (upstream), respectively, at velocity c. The variables $g^{\oplus}$ and $g^{\ominus}$, commonly called *characteristic variables*, are used to define *upwind fluxes* for solving time-dependent problems, see e.g. [283]. For more general problems, characteristic variables and upwind fluxes are obtained by solving local Riemann problems along the normal direction, see e.g. [176, 283].

4.1.3 Standard HDG method for Helmholtz problems

In standard HDG formulations, an additional variable $\widehat{u}_h$ corresponding to the numerical flux $\widehat{u}$ is introduced at the interface between the elements and on the boundary faces. The additional variable, which is called the *numerical trace* in the HDG literature, belongs to the space $\widehat{V}_h := \prod_{F\in\mathcal{F}_h}\mathcal{P}_p(F)$. The discrete unknowns associated to the fields u_h and $\boldsymbol{q}_h$ are eliminated in the solution procedure, leading to a reduced system with discrete unknowns associated to $\widehat{u}_h$ on the skeleton, see e.g. [80, 77].

After observing that $\boldsymbol{n}\cdot\widehat{\boldsymbol{q}}(u_h, \boldsymbol{q}_h) = u_h + \boldsymbol{n}\cdot\boldsymbol{q}_h - \widehat{u}_h$, we obtain the following HDG formulation, where

the numerical trace appears as a hybrid variable:

Find $(u_h, \boldsymbol{q}_h, \widehat{u}_h) \in V_h \times \boldsymbol{V}_h \times \widehat{V}_h$ such that, for all $(v_h, \boldsymbol{p}_h, \widehat{v}_h) \in V_h \times \boldsymbol{V}_h \times \widehat{V}_h$,

$$\begin{cases} -\imath\kappa(u_h, v_h)_{\mathcal{T}_h} - (\boldsymbol{q}_h, \nabla v_h)_{\mathcal{T}_h} + \langle u_h + \boldsymbol{n}\cdot\boldsymbol{q}_h - \widehat{u}_h, v_h\rangle_{\partial\mathcal{T}_h} = 0, \\ -\imath\kappa(\boldsymbol{q}_h, \boldsymbol{p}_h)_{\mathcal{T}_h} - (u_h, \nabla\cdot\boldsymbol{p}_h)_{\mathcal{T}_h} + \langle \widehat{u}_h, \boldsymbol{n}\cdot\boldsymbol{p}_h\rangle_{\partial\mathcal{T}_h} = 0, \\ \langle \widehat{u}_h, \widehat{v}_h\rangle_{\mathcal{F}_h} - \langle \tfrac{1}{2}(u_h + \boldsymbol{n}\cdot\boldsymbol{q}_h), \widehat{v}_h\rangle_{\partial\mathcal{T}_h} = \langle \tfrac{1}{2}s, \widehat{v}_h\rangle_{\Gamma}, \end{cases}$$

for a given surface data s on Γ.

This formulation is equivalent to the standard DG formulation (Problem 4.1.2) in the sense that the discrete solutions u_h and $\boldsymbol{q}_h$ are identical, see e.g. [212].

In the HDG literature [80, 157, 212], a generalization of the above formulation is often considered with

$$\boldsymbol{n}\cdot\widehat{\boldsymbol{q}}(u_h, \boldsymbol{q}_h) = \boldsymbol{n}\cdot\boldsymbol{q}_h + \tau(u_h - \widehat{u}_h),$$

where τ is the so-called *stabilization function*. The case $\tau = 1$ corresponds to the standard upwind fluxes, which are widely used in practice.

Local element-wise problems. In the hybridization procedure, the fields u_h and $\boldsymbol{q}_h$ are eliminated by solving local element-wise problems, where the numerical trace $\widehat{u}_h$ is considered as a given data. For each element K, the local problem reads:

Find $(u_K, \boldsymbol{q}_K) \in \mathcal{P}_p(K) \times \boldsymbol{\mathcal{P}}_p(K)$ such that, for all $(v_K, \boldsymbol{p}_K) \in \mathcal{P}_p(K) \times \boldsymbol{\mathcal{P}}_p(K)$,

$$\begin{cases} -\imath\kappa(u_K, v_K)_K - (\boldsymbol{q}_K, \nabla v_K)_K + \displaystyle\sum_{F\in\mathcal{F}_K} \langle u_K + \boldsymbol{n}_{K,F}\cdot\boldsymbol{q}_K, v_K\rangle_F = \sum_{F\in\mathcal{F}_K} \langle \widehat{u}_F, v_K\rangle_F, \\ -\imath\kappa(\boldsymbol{q}_K, \boldsymbol{p}_K)_K - (u_K, \nabla\cdot\boldsymbol{p}_K)_K = -\displaystyle\sum_{F\in\mathcal{F}_K} \langle \widehat{u}_F, \boldsymbol{n}_{K,F}\cdot\boldsymbol{p}_K\rangle_F, \end{cases} \tag{4.1.4}$$

for given surface data $\widehat{u}_F \in \mathcal{P}_p(F)$ for all $F \in \mathcal{F}_K$.

This local discrete problem is similar to a Helmholtz problem defined on K with a non-homogeneous Dirichlet boundary condition on ∂K. At the continuous level, Helmholtz problems with Dirichlet boundary conditions are ill-posed if the frequency corresponds to an eigenvalue of the Laplace operator, but the discrete problem is well-posed without any constraint. Nevertheless, the matrices of the local systems become ill-conditioned as kh goes to zero, see e.g. in [153, A6].

4.2 A hybridizable DG method with characteristic variables

This contribution is the result of a collaboration with T. Chaumont-Frelet in the framework of the ANR project *WavesDG*. It corresponds to the article [A6]. I obtained the numerical results using dedicated `MATLAB` scripts.

We have proposed a novel hybridization strategy, called the CHDG method, to accelerate the iterative solution of time-harmonic problems discretized with upwind DG finite element schemes. The CHDG method uses characteristic variables defined at the interface between the elements as the hybrid variables, as opposed to the Dirichlet traces in the standard HDG method. This choice leads to favorable properties for the resulting reduced system and to more efficient iterative solution procedures compared to the standard hybridization strategy.

Specifically, the reduced system can be written in the form $(\mathrm{I} - \Pi\mathrm{S})g = b$, where g corresponds to the characteristic variables, Π is an exchange operator, and S is scattering operator. We have proven that $\Pi\mathrm{S}$ is a strict contraction, so that the system is well-posed and can be solved with a fixed-point iteration. Numerical results show that CHDG always requires fewer iterations than the standard DG and HDG methods to reach a given accuracy with the GMRES and CGNR iterations.

4.2.1 Description of the CHDG method

We consider the standard DG formulation (4.1.2) with the upwind fluxes (4.1.3a)-(4.1.3b) for the time-harmonic problem (4.1.1). The CHDG method is a specific hybridization of this formulation in terms of the characteristic variables. For each face F of each element K, the upwind fluxes are rewritten as

$$\begin{cases} \widehat{u}_F = (g^{\oplus}_{K,F} + g^{\ominus}_{K,F})/2, \\ \boldsymbol{n}_{K,F} \cdot \widehat{\boldsymbol{q}}_F = (g^{\oplus}_{K,F} - g^{\ominus}_{K,F})/2, \end{cases}$$

with the *outgoing characteristic variable* $g^{\oplus}_{K,F}$ and the *incoming characteristic variable* $g^{\ominus}_{K,F}$ defined as

$$g^{\oplus}_{K,F} = u_K + \boldsymbol{n}_{K,F} \cdot \boldsymbol{q}_K \qquad \text{and} \qquad g^{\ominus}_{K,F} = \begin{cases} g^{\oplus}_{K',F} & \text{if } F \not\subset \Gamma \text{ is shared by } K \text{ and } K', \\ s & \text{if } F \subset \Gamma. \end{cases}$$

The outgoing characteristic variable depends only on the physical unknowns defined on K. The incoming characteristic variable depends on the unknowns of the neighboring element K' if F is an interior face (i.e. $F \not\subset \Gamma$), and it depends on the boundary condition if F is a boundary face (i.e. $F \subset \Gamma$). For an interior face, the outgoing characteristic variable of one side corresponds to the incoming characteristic variable of the other side, i.e. $g^{\oplus}_{K,F} = g^{\ominus}_{K',F}$ and $g^{\ominus}_{K,F} = g^{\oplus}_{K',F}$. The notations are illustrated on Figure 4.1.

The CHDG formulation. We introduce an additional variable, denoted $g^{\ominus}_h$, corresponding to the incoming characteristic variable at the boundary of each element. The variable $g^{\ominus}_h$ belongs to the space $G_h := \prod_{K\in\mathcal{T}_h} \prod_{F\in\mathcal{F}_K} \mathcal{P}_p(F)$. Therefore, at each interior face, there are two variables corresponding to

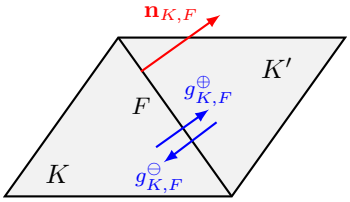

Figure 4.1: Notations for the outgoing and incoming characteristic variables (resp. $g^{\oplus}_{K,F}$ and $g^{\ominus}_{K,F}$) at the face F shared by an element K and a neighboring element K'. Reproduced from [A6].

the incoming variables associated with the neighboring elements. The CHDG formulation then reads:

$$\left|\begin{array}{l}\text{Find } (u_h, \boldsymbol{q}_h, g_h^{\ominus}) \in V_h \times \boldsymbol{V}_h \times G_h \text{ such that, for all } (v_h, \boldsymbol{p}_h, \xi_h) \in V_h \times \boldsymbol{V}_h \times G_h, \\ \quad \left\{\begin{array}{rl} -\imath\kappa(u_h, v_h)_{\mathcal{T}_h} - (\boldsymbol{q}_h, \nabla v_h)_{\mathcal{T}_h} + \langle \frac{1}{2}(g^{\oplus}(u_h, \boldsymbol{q}_h) - g_h^{\ominus}), v_h\rangle_{\partial\mathcal{T}_h} &= 0, \\ -\imath\kappa(\boldsymbol{q}_h, \boldsymbol{p}_h)_{\mathcal{T}_h} - (u_h, \nabla\cdot\boldsymbol{p}_h)_{\mathcal{T}_h} + \langle \frac{1}{2}(g^{\oplus}(u_h, \boldsymbol{q}_h) + g_h^{\ominus}), \boldsymbol{n}\cdot\boldsymbol{p}_h\rangle_{\partial\mathcal{T}_h} &= 0, \\ \langle g_h^{\ominus} - \Pi(g^{\oplus}(u_h, \boldsymbol{q}_h)), \xi_h\rangle_{\partial\mathcal{T}_h} &= \langle b, \xi_h\rangle_{\partial\mathcal{T}_h}, \end{array}\right. \\ \text{with } g^{\oplus}(u_h, \boldsymbol{q}_h) := u_h + \boldsymbol{n}\cdot\boldsymbol{q}_h. \end{array}\right. \tag{4.2.1}$$

In the last equation, we have introduced the *global exchange operator* $\Pi : G_h \longrightarrow G_h$ and the *global right-hand side* b. For each face F of each element K, they are given by

$$\Pi(g^{\oplus})|_{K,F} = \begin{cases} g^{\oplus}_{K',F} & \text{if } F \not\subset \Gamma \text{ is shared by } K \text{ and } K', \\ 0 & \text{if } F \subset \Gamma, \end{cases} \qquad \text{and} \qquad b|_{K,F} = \begin{cases} 0 & \text{if } F \not\subset \Gamma, \\ s & \text{if } F \subset \Gamma. \end{cases}$$

With these definitions, the last equation of system (4.2.1) weakly enforces that the incoming characteristic variable of an element is the outgoing one of the neighboring element at each interior face. At each boundary face, it weakly enforces the boundary condition. The DG, HDG and CHDG are equivalent.

Local element-wise problems. In the hybridization procedure, the physical variables are eliminated from the formulation by solving local element-wise problems, where the incoming characteristic variable is considered as a given data. For each element K, the local problem reads:

$$\left|\begin{array}{l}\text{Find } (u_K, \boldsymbol{q}_K) \in \mathcal{P}_p(K) \times \boldsymbol{\mathcal{P}}_p(K) \text{ such that, for all } (v_K, \boldsymbol{p}_K) \in \mathcal{P}_p(K) \times \boldsymbol{\mathcal{P}}_p(K), \\ \quad \left\{\begin{array}{rl} -\imath\kappa(u_K, v_K)_K - (\boldsymbol{q}_K, \nabla v_K)_K + \displaystyle\sum_{F\in\mathcal{F}_K} \langle \frac{1}{2} g^{\oplus}_{K,F}, v_K\rangle_F &= \displaystyle\sum_{F\in\mathcal{F}_K} \langle \frac{1}{2} g^{\ominus}_{K,F}, v_K\rangle_F, \\ -\imath\kappa(\boldsymbol{q}_K, \boldsymbol{p}_K)_K - (u_K, \nabla\cdot\boldsymbol{p}_K)_K + \displaystyle\sum_{F\in\mathcal{F}_K} \langle \frac{1}{2} g^{\oplus}_{K,F}, \boldsymbol{n}_{K,F}\cdot\boldsymbol{p}_K\rangle_F &= -\displaystyle\sum_{F\in\mathcal{F}_K} \langle \frac{1}{2} g^{\ominus}_{K,F}, \boldsymbol{n}_{K,F}\cdot\boldsymbol{p}_K\rangle_F, \end{array}\right. \\ \text{with } g^{\oplus}_{K,F} = u_K + \boldsymbol{n}_{K,F}\cdot\boldsymbol{q}_K, \text{ for given surface data } g^{\ominus}_{K,F} \in \mathcal{P}_p(F) \text{ for all } F \in \mathcal{F}_K. \end{array}\right. \tag{4.2.2}$$

This local problem is well-posed [A6, Theorem 2.9]. It can be interpreted as a discretized Helmholtz problem defined on K with a Robin boundary condition on ∂K. In contrast to Helmholtz problems with Dirichlet boundary conditions, these local problems are always well-posed at the continuous level.

Reduced problem. To write the reduced problem obtained after removing the physical variables, we introduce the *global scattering operator* $\mathrm{S} : G_h \longrightarrow G_h$. For each face F of each element K, it is given by

$$\mathrm{S}(g_h^{\ominus})\big|_{K,F} := u_K(g_h^{\ominus}) + \boldsymbol{n}_{K,F}\cdot\boldsymbol{q}_K(g_h^{\ominus}),$$

where $(u_K, \boldsymbol{q}_K)$ is the solution of the local problem (4.2.2) with the surface data $(g^{\ominus}_{K,F})_{F\in\mathcal{F}_K}$ contained in $g_h^{\ominus}$. This operator can be interpreted as an *"incoming characteristic variable to outgoing characteristic variable"* operator. The reduced problem then reads:

$$\left|\begin{array}{l}\text{Find } g_h^{\ominus} \in G_h \text{ such that } \langle g_h^{\ominus} - \Pi\mathrm{S}(g_h^{\ominus}), \xi_h\rangle_{\partial\mathcal{T}_h} = \langle b, \xi_h\rangle_{\partial\mathcal{T}_h} \text{ for all } \xi_h \in G_h, \end{array}\right.$$

which can be rewritten as

$$\left|\begin{array}{l}\text{Find } g_h^{\ominus} \in G_h \text{ such that } (\mathrm{I} - \Pi\mathrm{S})g_h^{\ominus} = b_h. \end{array}\right. \tag{4.2.3}$$

with the *global projected right-hand side* $b_h \in G_h$ defined such that $\langle b, \xi_h\rangle_{\partial\mathcal{T}_h} = \langle b_h, \xi_h\rangle_{\partial\mathcal{T}_h}$ for all $\xi_h \in G_h$. The reduced problem is equivalent to the global problem because the local problems are well-posed.

Systems with the same form as the reduced system (4.2.3) appear in non-overlapping substructuring DDMs, see Section 3.1.2. This system is also similar to the UWVF proposed in the framework of Trefftz

DG methods with non-polynomial basis functions for time-harmonic problems, see e.g. [60, 219, 21, 246]. The operator ΠS was already used in the seminal works of Després [98] and Cessenat and Després [60]. In fact, the CHDG method can be seen as an element-wise DDM, where the discrete transmission conditions are built from the numerical fluxes that naturally arise in the DG setting. Here, cross-points where multiple mesh faces meet are naturally handled without any special treatment. In contrast, DDMs based on conformal FEMs may require special treatments to properly account for cross-points, see Section 3.1.2.

Analysis of the reduced problem. In [A6, Section 3.2], we have proved that the operator ΠS is a *strict contraction* for the norm $\|\cdot\|$ defined as

$$\|g_h^{\ominus}\|^2 := \sum_{K\in\mathcal{T}_h}\sum_{F\in\mathcal{F}_K} \|g_{K,F}^{\ominus}\|_F^2,$$

where $\|\cdot\|_F$ is the L^2 norm on F. As a consequence, the reduced problem is always well-posed, and it can be solved with the fixed-point iteration (at least in principle). The result is as follows.

Proposition 4.2.1.

- *The operator* S *is a strict contraction:* $\|\mathrm{S}(g_h^{\ominus})\| < \|g_h^{\ominus}\|$, *for all* $g_h^{\ominus} \in G_h\backslash\{0\}$.
- *The operator* Π *is a contraction:* $\|\Pi(g_h^{\ominus})\| \leq \|g_h^{\ominus}\|$, *for all* $g_h^{\ominus} \in G_h$.
- *The operator* ΠS *is a strict contraction:* $\|\Pi\mathrm{S}(g_h^{\ominus})\| < \|g_h^{\ominus}\|$ *for all* $g_h^{\ominus} \in G_h\backslash\{0\}$.

If a Dirichlet or Neumann boundary condition is prescribed on Γ *instead of a Robin boundary condition, then* Π *is an involution and an isometry:* $\Pi^2 = \mathrm{I}$ *and* $\|\Pi(g_h^{\ominus})\| = \|g_h^{\ominus}\|$, *for all* $\forall g_h^{\ominus} \in G_h$.

The strict contraction of ΠS is due to the fact that S and/or Π dissipate energy. The scattering operator S is always strictly contracting whereas, in a continuous context, it preserves energy. This property is a numerical artifact related to the fact that there is no polynomial solution to the Helmholtz equation. The exchange operator Π can dissipate energy with a Robin condition, and it is an involution with a Dirichlet or Neumann condition. Therefore, there are two sources of dissipation: numerical dissipation, which is always present but can become small as the mesh is refined (possibly leading to slow convergence of fixed-point iterations for energy-preserving problems), and physical dissipation.

Note that, for conservative methods (including standard conforming FEMs), S does not dissipate, and ΠS preserve energy if there is no physical dissipation. In fact, the convergence of standard DDMs is proven only for energy-preserving problems with relaxation, e.g. [75]. It has been proven recently in [246] that the iteration matrix of a Trefftz DG method is also a strict contraction for a configuration with a Robin boundary condition. To the best of our knowledge, this is the only other example of FEM that can be written with a strictly contracting iterative matrix for Helmholtz problems.

4.2.2 Numerical study of the algebraic system

Algebraic system. In this work, the physical fields u_h and $\boldsymbol{q}_h$ are represented with standard hierarchical shape functions based on Lobatto functions, see e.g. [267, 40]. The hybrid fields defined on the skeleton, i.e. $\widehat{u}_h$ for HDG and $g_h^{\ominus}$ for CHDG, are univariate polynomials on each face. A possible choice of shape functions would be the *Lobatto functions*, which correspond to the restriction of the shape functions used for the physical fields. We can also consider the *scaled Legendre functions* that are scaled so that the local mass matrix of each face is the identity matrix. Both approaches give rigorously the same numerical solution (up to floating point errors), but they lead to different algebraic systems.

In fact, the algebraic system corresponding to the scaled Legendre functions, denoted by $\mathbf{A}\mathbf{g} = \mathbf{b}$, can be obtained from the one corresponding to the Lobatto functions, denoted by $\mathbf{A}_{\mathrm{Lob}}\mathbf{g}_{\mathrm{Lob}} = \mathbf{b}_{\mathrm{Lob}}$, by using a symmetric preconditioning: $\mathbf{A} = \mathbf{M}_{\mathrm{Lob}}^{-1/2}\mathbf{A}_{\mathrm{Lob}}\mathbf{M}_{\mathrm{Lob}}^{-1/2}$, $\mathbf{g} = \mathbf{M}_{\mathrm{Lob}}^{1/2}\mathbf{g}_{\mathrm{Lob}}$ and $\mathbf{b} = \mathbf{M}_{\mathrm{Lob}}^{-1/2}\mathbf{b}_{\mathrm{Lob}}$, where $\mathbf{M}_{\mathrm{Lob}}$ is the mass matrix associated to the faces. In preliminary comparisons, we have observed that, for both

(a) Benchmark 1: Robin problem (Plane wave)

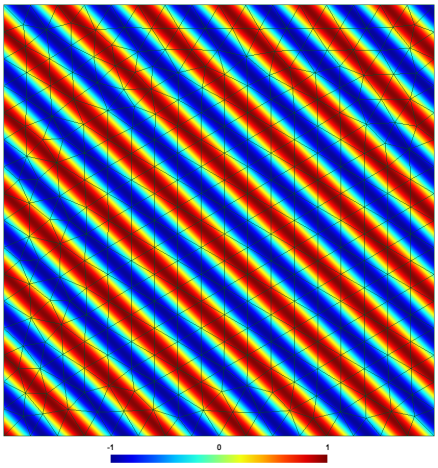

(b) Benchmark 2: Dirichlet problem (Cavity)

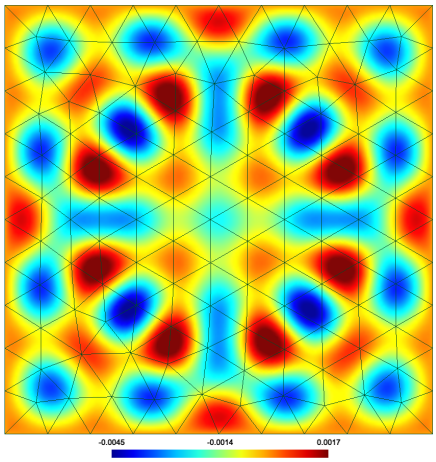

(c) Benchmark 3: Robin/Dirichlet problem (Half-open waveguide)

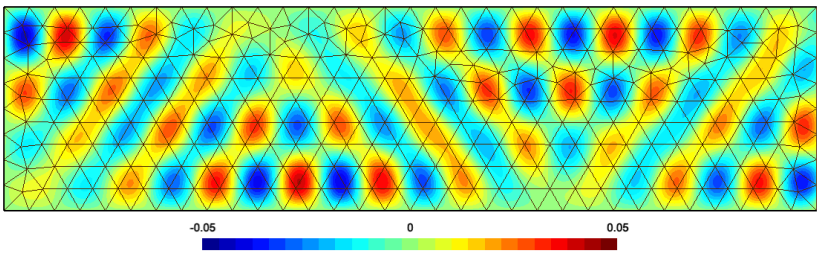

Figure 4.2: Real part of the reference solution of the three benchmarks with the default parameters. Reproduced from [A6].

HDG and CHDG, the convergence of the iterative solution procedures (without preconditioning) is faster with the scaled Legendre functions than with the Lobatto functions. The preconditioning approach is equivalent to using $\mathbf{M}_{\mathrm{Lob}}$ as a left preconditioner and using $\langle\cdot,\cdot\rangle_F$ as inner product in weighted Krylov methods. For the sake of brevity, only results with the scaled Legendre functions are presented below.

Reference benchmarks. We have considered three benchmarks already used in [64], see Figure 4.2. The simulations were performed with a dedicated `MATLAB` code and `Gmsh` [142] for the pre- and post-processing operations. For each benchmark, we have used third-degree polynomial bases (i.e. $p = 3$), two values for the wavenumber κ, and an element size h corresponding to a relative error close to 10^{-2} in each case. In this work, we always consider the relative error of the physical fields defined as

$$\sqrt{\|u_h - u_{\mathrm{ref}}\|_\Omega^2 + \|\boldsymbol{q}_h - \boldsymbol{q}_{\mathrm{ref}}\|_\Omega^2} \Big/ \sqrt{\|u_{\mathrm{ref}}\|_\Omega^2 + \|\boldsymbol{q}_{\mathrm{ref}}\|_\Omega^2},$$

where $u_{\mathrm{ref}}(\boldsymbol{x})$ and $\boldsymbol{q}_{\mathrm{ref}}(\boldsymbol{x})$ correspond to the reference analytical or semi-analytical solution.

Benchmark 1: Robin problem (Plane wave). The plane wave $u_{\mathrm{ref}}(\boldsymbol{x}) = e^{\imath\kappa\boldsymbol{d}\cdot\boldsymbol{x}}$ with $\boldsymbol{d} = (1,1)/\sqrt{2}$ is prescribed at the boundary of $\Omega =]0,1[\times]0,1[$ by using a non-homogeneous Robin boundary condition. We have used $\kappa = 15\pi$ and $h = 1/16$ (default parameters), and $\kappa = 30\pi$ and $h = 1/34$ (higher frequency).

Benchmark 2: Dirichlet problem (Cavity). The homogeneous Dirichlet boundary condition on p is used on the boundary of $\Omega =]0,1[\times]0,1[$ with a unit source term on Ω. The eigenvalues of this problem are $\kappa_{n,m}^2 := (n^2+m^2)\pi^2$ for all $m, n > 0$. The reference solution, which is real, is obtained semi-analytically by truncating the Fourier expansion, see [64]. We have used $\kappa = (7+1/10)\sqrt{2}\pi$ and $h = 1/10$ (default parameters), and $\kappa = (7+1/100)\sqrt{2}\pi$ and $h = 1/15$ (parameters closer to an eigenvalue).

Benchmark 3: Robin/Dirichlet problem (Half-open waveguide). We consider the waveguide $\Omega =$

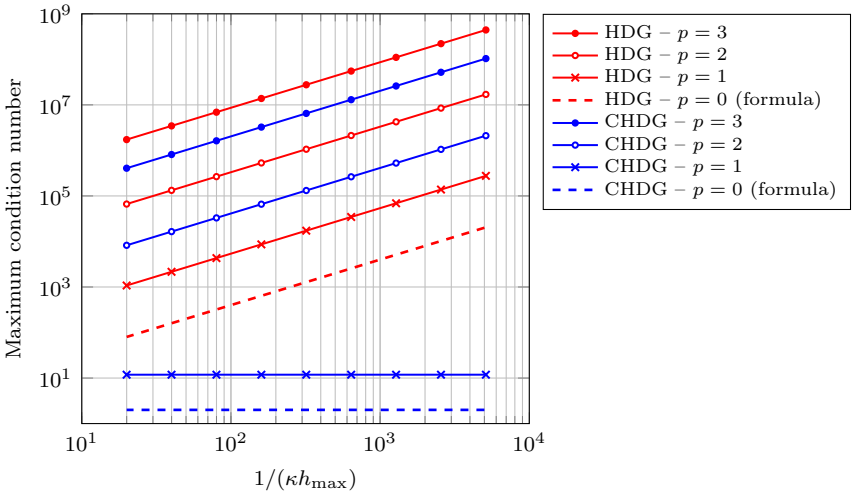

Figure 4.3: Maximum condition number of the local HDG/CHDG matrices as a function of $1/(\kappa h_{\max})$ for $p = 1, 2$ and 3, where κ is the wavenumber and $h_{\max}$ is the length of the longest edge. The condition numbers corresponding to formulas (4.2.4) and (4.2.5) are plotted with dashed lines. Reproduced from [A6].

$]0,4[\times]0,1[$ with the non-homogeneous Robin condition $\partial_n u - \imath\kappa u = e^{\imath\kappa \boldsymbol{d}\cdot\boldsymbol{x}}$ on the right side, and $u = 0$ on the other sides. The reference solution is computed by using a semi-analytical approach, see [64]. We have used $\kappa = 6\pi$ and $h = 1/8$ (default parameters), and $\kappa = 12\pi$ and $h = 1/17$ (higher frequency).

Memory storage. The number of degrees of freedom (DOFs) is almost twice as high with the CHDG method than with the HDG method because there are two characteristic variables and only one numerical trace per interior face. The number of non-zero entries (NNZ) in the reduced matrices $\mathbf{A}_{\mathrm{HDG}}$ and $\mathbf{A}_{\mathrm{CHDG}}$ can be estimated. Assuming that the number of boundary faces is negligible compared to the number of interior faces, we have obtained the estimate $\#\mathrm{NNZ}(\mathbf{A}_{\mathrm{CHDG}})/\#\mathrm{NNZ}(\mathbf{A}_{\mathrm{HDG}}) \approx 1.6$. For the matrices of the reference benchmarks, this ratio varies between 1.54 and 1.66. Thus, although CHDG has almost twice as many DOFs as HDG, the number of non-zero elements does not increase as much. These results are similar in 3D, but the ratio between the number of non-zero entries is smaller (1.43).

Conditionning of the local matrices. The construction of the reduced matrix $\mathbf{A}$ of HDG and CHDG, and the application of $\mathbf{A}$ in matrix-free iterative procedures, require the solution of the local element-wise problems (4.1.4) and (4.2.2), respectively. As a preliminary study, the local problems are defined on a square element of side length h with constant shape functions, i.e. $p = 0$. This configuration was considered in [153]. The condition number of the matrices corresponding to the HDG local problem (4.1.4) and the CHDG local problem (4.2.2) are

$$\mathrm{cond}(\mathbf{A}_{\mathrm{HDG,loc}}) = \sqrt{1 + 16/(\kappa h)^2}, \tag{4.2.4}$$

$$\mathrm{cond}(\mathbf{A}_{\mathrm{CHDG,loc}}) = \sqrt{((\kappa h)^2 + 4)/((\kappa h)^2 + 1)}. \tag{4.2.5}$$

The condition number is always the larger for the HDG local matrix, and this matrix becomes ill-conditioned as κh goes to zero, while the CHDG local matrix remains well-conditioned.

To continue the study, we have considered an unstructured mesh of $\Omega =]0,1[^2$ with 1478 triangles. The condition number of the local matrices is computed on all triangles. On Figure 4.3, the maximum condition number is plotted as a function of $1/(\kappa h_{\max})$, which is a measure of the mesh density. We observe that the condition number increases linearly with $1/(\kappa h_{\max})$ in all cases, except for CHDG with $p = 1$. Therefore, refining the mesh for a given wavenumber, or using a smaller wavenumber with a given mesh, increases the condition number of the local matrices. For a given p, the condition number is always higher with HDG than with CHDG. Increasing p increases the condition number in all the cases.

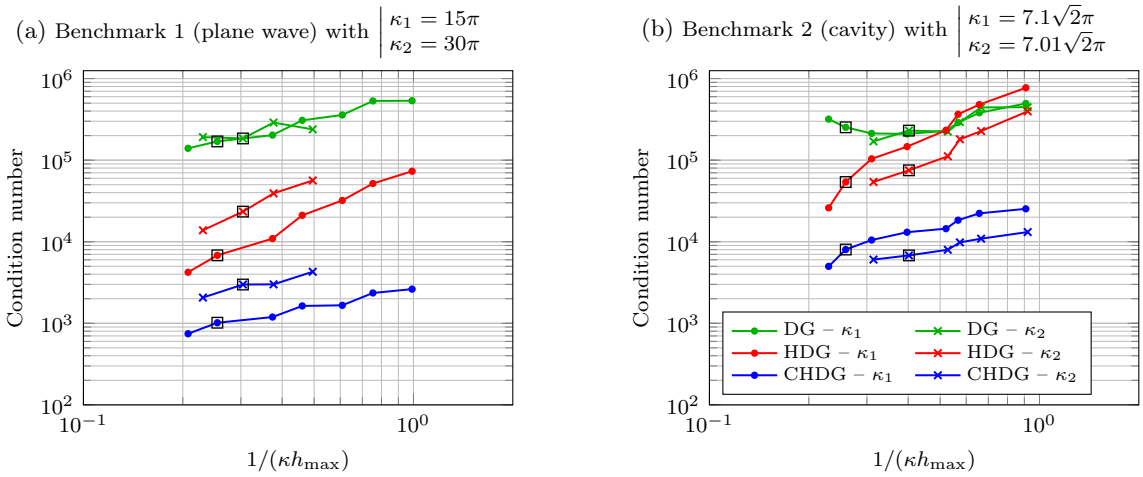

Figure 4.4: Condition number of the global/reduced matrix $\mathbf{A}$ of the different methods as a function of $1/(\kappa h_{\max})$, where $h_{\max}$ is the length of the longest edge. Two benchmarks are considered with two values of κ. The black squares correspond to configurations with a relative error close to 10^{-2}. Reproduced from [A6].

Conditionning of the global matrices. The condition number of the global/reduced matrix $\mathbf{A}$ is plotted as a function of $1/(\kappa h_{\max})$ for the DG, HDG and CHDG methods on Figure 4.4. The first two benchmarks are considered with two sets of parameters. For all the results, the relative error is smaller than 10^{-1}. The black squares correspond to configurations with a relative error close to 10^{-2}.

The condition number is always smaller with CHDG than with HDG and DG by one or two orders of magnitude in almost all the cases. Moreover, the condition number increases almost linearly with $1/(\kappa h_{\max})$ for DG and CHDG, while the increase is almost quadratic for HDG. The influence of κ on the condition number is similar for HDG and CHDG: the condition number increases with the wavenumber. In contrast, the condition number for the DG method without hybridization does not vary much with κ.

4.2.3 Numerical study of the iterative solution procedures

Convergence of the fixed-point iterative scheme for CHDG. The algebraic CHDG system can be written as $(\mathbf{I} - \mathbf{\Pi S})\mathbf{g} = \mathbf{b}$, where $\mathbf{I}$, $\mathbf{\Pi}$ and $\mathbf{S}$ are the identity, exchange and scattering matrices, respectively. Since ΠS is a strict contraction, the spectral radius $\rho(\mathbf{\Pi S})$ must be strictly lower than 1, and the Richardson iteration converges without relaxation. For a given initial guess $\mathbf{g}^{(0)}$, the procedure reads $\mathbf{g}^{(\ell+1)} = \mathbf{\Pi S}\mathbf{g}^{(\ell)} + \mathbf{b}$, for $\ell = 0, 1, \ldots$. If the eigenvalues of the iteration operator are far from the unit disk, i.e. $\rho(\mathbf{\Pi S}) \ll 1$, this procedure will converge rapidly.

The values of the spectral radius $\rho(\mathbf{\Pi S})$ obtained with the different benchmarks and different parameters are given in Table 4.1. In all the cases, the eigenvalues are strictly inside the unit circle, and we will see below that the fixed-point iteration effectively converges. Nevertheless, some eigenvalues are close to the unit circle, so that the spectral radius is close to one. For each benchmark, we observe that the spectral radius is closer to one when using a finer mesh (second column of each benchmark in Table 4.1) or when using the second wavenumber with the fine mesh (third column).

Table 4.1: Spectral radius $\rho(\mathbf{\Pi S})$ for the three benchmarks with different parameters. Reproduced from [A6].

	Benchmark 1 (plane wave)			Benchmark 2 (cavity)			Benchmark 3 (waveguide)		
κ	15π	15π	30π	$7.1\sqrt{2}\pi$	$7.1\sqrt{2}\pi$	$7.01\sqrt{2}\pi$	6π	6π	12π
h	1/16	1/34	1/34	1/10	1/15	1/15	1/8	1/17	1/17
κh	2.95	1.39	2.77	3.15	2.10	2.08	2.36	1.11	2.22
$1 - \rho(\mathbf{\Pi S})$	$2.9\,10^{-3}$	$7.8\,10^{-5}$	$5.5\,10^{-4}$	$2.8\,10^{-4}$	$1.5\,10^{-5}$	$1.4\,10^{-5}$	$5.5\,10^{-5}$	$2.5\,10^{-6}$	$2.9\,10^{-5}$

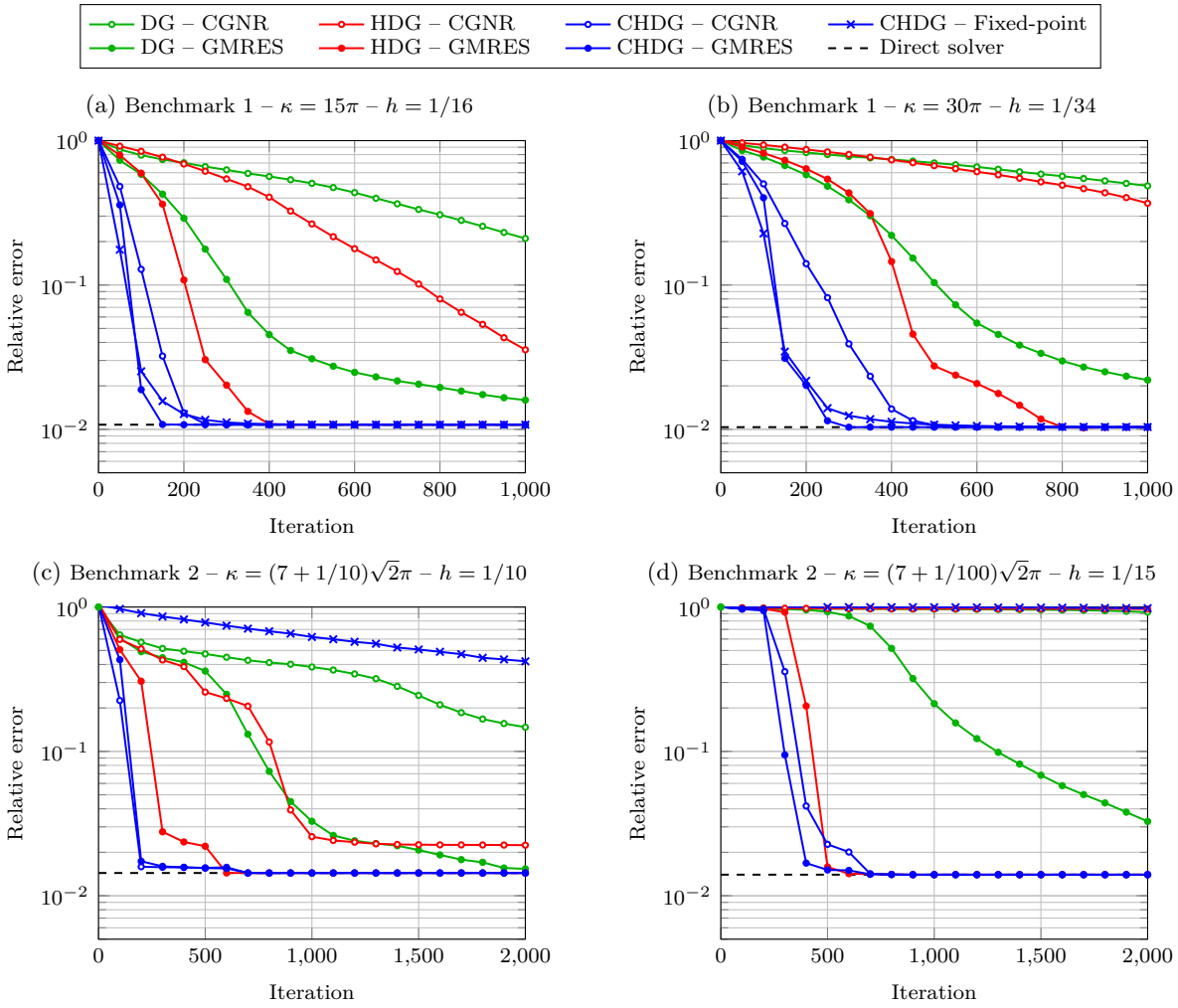

Figure 4.5: Error history with different iterative schemes and different DG schemes for two benchmarks. The dashed horizontal lines correspond to the relative errors obtained with a direct solver. Reproduced from [A6].

Comparison of DG, HDG and CHDG with for iterative solution procedures. The error histories obtained with the fixed-point iteration (for CHDG only), CGNR (i.e. conjugate gradient applied to the normal equation $\mathbf{A}^*\mathbf{A}\mathbf{g} = \mathbf{A}^*\mathbf{b}$) and GMRES (without restart) are shown on Figure 4.5 for the different methods and the first two benchmarks. The numerical solution is always compared to the analytical or semi-analytical reference solution. See [A6] for more results.

We observe that the fixed-point iteration effectively converges for the CHDG method, but the performance strongly depends on the physical setting. The convergence is very fast for purely propagating cases, and it is slow for cavity or waveguide cases. In the latter cases, the asymptotic regime, which can start relatively quickly, is rather slow. The fixed-point iteration does not converge for the DG and HDG methods. If the problem is solved with either CGNR or GMRES, the convergence of the iterative process is always faster with the CHDG method than with the DG and HDG methods.

When using the CHDG method, the convergence is always slightly faster with GMRES than with CGNR, but the difference is not very large. In the worst case (Figure 4.5b), the number of iterations to achieve the reference relative error (obtained with the direct solver) is twice larger with CGNR than with GMRES. Considering the computational cost of GMRES, which increases at each iteration, the CGNR is a potential good candidate for realistic cases.

Chapter 5

Perspectives

In this chapter, I describe open questions, ongoing works and possible future research directions that are directly related to the work presented in this manuscript.

About domain truncation methods

HABC with corner/edge treatments for other wave models. Padé-type HABCs are available for electromagnetic, elastic and heterogeneous scalar waves, but only for smooth artificial boundaries [108, 62, 224, 221]. To the best of my knowledge, no corner treatment has been proposed for these models, except one approach by Collino [83] for the time-domain Maxwell equations discretized with finite differences. The extension of the corner compatibility relations derived in [A9] remains to be done for these models, but this is technically more difficult than for the acoustic case because of the transverse operators involved in the corresponding HABCs. In contrast, the numerical curvature strategy studied in [A9] can be used directly in the formulations available for curved boundaries.

AML implementation of the PML for other wave models. The AML implementation has only been tested for acoustic waves, but similar implementations could be derived for electromagnetic and elastic waves. For these models, PML formulations that exhibit the complex Jacobian matrix of the PML transformation are available [225]. It should then be possible to derive AML finite element implementations similarly to the acoustic case. Note that, for elastic wave models, the choice of parameters may be trikier due to the different types of elastic waves.

Dealing with non-right and non-flat angles. Both HABC and PML implementations are much less accurate for configurations with angles far from 90° and 180°. For Padé-type HABCs, the modeling errors due to the corners can be reduced thanks to the treatments presented e.g. in [A9], but these errors are still significant. The generalization of the corner/edge compatibility relations for non-right angles is still an open question for the Padé-type HABC. The adaptation of techniques proposed for other truncation methods [159, 95, 47, 192] could be explored.

Other uses of the domain truncation methods. As presented in Chapter 3, the domain truncation operators can be used to improve DDMs. In [63, 9, 92], Padé-type HABC operators are also used in the definition of boundary integral formulations in order to speed up iterative solution procedures based on these formulations. Investigating combinations with the improved domain truncation methods presented in this manuscript could be an interesting research direction. A first study was carried out in the context of the M1 internship of N. Kesmia, in collaboration with S. Chaillat (CNRS, POEMS).

About accelerated iterative solvers

Extending the DDMs with HABC/PML transmissions and cross-point treatments. The DDM strategies presented in this manuscript could be extended to other physical models and 3D checkerboard domain

partitions, provided that the corner/edge treatments are available for the HABC and PML boundary operators. The 3D extension is not an issue in the acoustic case: 3D results have been presented in the PhD theses of R. Dai [91] and A. Royer [257] for DDMs with HABC and PML transmissions, respectively. A. Royer also proposed DDM results for 2D and 3D elastic wave models with a PML transmission and cross-point treatments. A similar extension should not be too complicated to obtain for electromagnetic waves. In contrast, cross-point treatments for DDMs with HABC transmission are currently out of reach for other wave models due to the unavailability of corner/edge treatments. In practice, general mesh-based domain partitioning is often used, and extensions of our approaches could be explored for such partitions. However, I am not sure if this is a good way to go, since the HABC and PML techniques are initially designed for smooth boundaries (with special treatments for corners/edges), and adaptation to non-straight boundaries would require several additional non-trivial steps.

Extending the multidirectional sweeping preconditioners. The sweeping preconditioners presented in Section 3.4 can be extended to 3D checkerboard domain partition, see [91] for preliminary results. The idea remains to propagate information as fast as possible across the domain partition, possibly with parallel sweeps in different directions. It would be interesting to investigate similar sweeping strategies for general mesh-based domain partitions, as well as placement strategies when using parallel computing on distributed memory architectures.

Improving our understanding of the convergence of iterative solvers. Iterative solvers based on Krylov methods are widely used to solve time-harmonic problems discretized with finite elements. By using DDM, we aim to improve the properties of the resulting algebraic systems in order to speed up the iterative solution procedures. However, it is difficult to know which properties to study and how to interpret them. In the context of the PhD research of T. Raynaud, which I supervise together with P. Marchand (Inria, POEMS) and V. Dolean (TU/e, The Netherlands), we aim to improve our understanding of the convergence of Krylov methods for solving time-harmonic problems, and then to improve preconditioning strategies.

About discontinuous finite element solvers

Dealing with other wave models. In principle, the CHDG method that we proposed for acoustic waves in [A6] could be extended to other physical waves and to heterogeneous media. DG formulations with upwind fluxes are available for most of the standard wave propagation models, and hybridization strategies with characteristic variables (or similar transmission variables) could be explored. For heterogeneous media and more complicated physical models, several choices of numerical fluxes are possible (see e.g. [102, 283]), which raise additional questions. For each model, the goal is to find the best numerical fluxes and the best hybrid variables that lead to reduced systems with good properties for fast iterative solutions procedures. The aeroacoustic and heterogeneous cases are currently studied in the context of the PhD research of S. Pescuma, in collaboration with G. Gabard (LAUM, Le Mans U.). The electromagnetic case will be studied in the context of *ElectroMath*.

Coupling with other methods. Many extensions of the CHDG method can be explored to improve the accuracy of the numerical solution and the efficiency of the iterative procedures. Some of these are planned in the context of *WavesDG*. First, the CHDG formulation could be tested with plane-wave basis functions (or other wave-specific basis functions), instead of the polynomial basis functions, in the spirit of the Trefftz methods. Second, HABC and PML can be incorporated into CHDG formulations to improve the representation of artificial boundaries for e.g. scattering problems. In [A11, A5], we have implemented HABC and PML in DG formulations based on upwind fluxes for a time-dependent acoustic model. Similar formulations could be proposed with the CHDG methods. During his internship, S. Pescuma investigated the use of HABC with a Trefftz DG method. Finally, we plan to investigate DDM substructuring and preconditioning strategies for the reduced system obtained with CHDG. These extensions are natural continuations and intersections of the different works presented in this manuscript.

Towards time-harmonic electromagnetic problems with anisotropic media *[ElectroMath]*

The numerical simulation of time-harmonic electromagnetic problems with anisotropic/dissipative media is of paramount importance for the study of wave propagation in plasmas, optical metamaterials and metasurfaces. Both theoretical and practical aspects are challenging areas of research.

In the context of the PhD research of D. Chicaud [A3, 69, 70], which I co-supervised with P. Ciarlet (ENSTA Paris, POEMS), we studied time-harmonic electromagnetic problems with *elliptic* material tensor fields, which are a general class of material coefficients. A complex d-by-d tensor field $\boldsymbol{\xi} \in \boldsymbol{L}^\infty(\Omega)$ is *elliptic* if there exist $\theta_{\boldsymbol{\xi}} \in \mathbb{R}$ and $\exists \xi_- > 0$, almost everywhere in Ω, $\Re\{e^{\imath\theta_{\boldsymbol{\xi}}}\, \boldsymbol{z}^* \boldsymbol{\xi} \boldsymbol{z}\} \geq \xi_- |\boldsymbol{z}|^2$, for all $\boldsymbol{z} \in \mathbb{C}^d$. We extended the functional framework that was available for isotropic media, and we generalized well-posedness and regularity results. We considered problems with Dirichlet and Neumann boundary conditions in [A3], and D. Chicaud and P. Ciarlet [70] completed analyses for the Robin case with an impedance tensor field. Some of these tools have been used to study the DDM iterative schemes, which was our initial motivation.

These results provide a solid foundation for further studies, some of which are planned within the CIEDS project *ElectroMath*. We are currently extending the analysis of DDM for electromagnetic wave propagation in anisotropic media, which was started at the end of the PhD research of D. Chicaud. We plan to investigate a CHDG method for electromagnetic problems with media of increasing complexity (i.e. isotropic, anisotropic, dissipative, ...). We would like to link the proposed methods with real applications by classifying problems coming from physicists and physical engineers.

Towards GPU-accelerated CHDG solvers for time-harmonic problems *[WavesDG]*

To conclude this manuscript, I would like to mention that one of my long-term goals is to develop efficient time-harmonic solvers that scale on modern supercomputers composed of many-core processors and limited-memory accelerators (such as GPUs). Existing approaches are not well suited for efficient computation on these architectures because they require sparse direct solvers or large memory storages, or they are prohibitively expensive in terms of the number of iterations. I believe that the research done in the *WavesDG* project is a step in the direction of more efficient solvers. The use of wave-specific strategies at all levels, with the CHDG finite element method combined with suited DDM preconditioning and substructuring strategies, could lead to efficient solvers for GPU clusters.

Bibliography

Selected articles of the author published in peer-reviewed journals

[A1] H. Bériot and A. Modave. An automatic perfectly matched layer for acoustic finite element simulations in convex domains of general shape. *International Journal for Numerical Methods in Engineering*, 122(5):1239–1261, 2021.

[A2] J. Chan, Z. Wang, A. Modave, J.-F. Remacle, and T. Warburton. GPU-accelerated discontinuous Galerkin methods on hybrid meshes. *Journal of Computational Physics*, 318:142–168, 2016.

[A3] D. Chicaud, P. Ciarlet Jr, and A. Modave. Analysis of variational formulations and low-regularity solutions for time-harmonic electromagnetic problems in complex anisotropic media. *SIAM Journal on Mathematical Analysis*, 53(3):2691–2717, 2021.

[A4] R. Dai, A. Modave, J.-F. Remacle, and C. Geuzaine. Multidirectional sweeping preconditioners with non-overlapping checkerboard domain decomposition for Helmholtz problems. *Journal of Computational Physics*, 453:110887, 2022.

[A5] A. Modave, A. Atle, J. Chan, and T. Warburton. A GPU-accelerated nodal discontinuous Galerkin method with high-order absorbing boundary conditions and corner/edge compatibility. *International Journal for Numerical Methods in Engineering*, 112(11):1659–1686, 2017.

[A6] A. Modave and T. Chaumont-Frelet. A hybridizable discontinuous Galerkin method with characteristic variables for Helmholtz problems. *Journal of Computational Physics*, 493:112459, 2023.

[A7] A. Modave, E. Deleersnijder, and E. Delhez. On the parameters of absorbing layers for shallow water models. *Ocean Dynamics*, 60(1):65–79, 2010.

[A8] A. Modave, E. Delhez, and C. Geuzaine. Optimizing perfectly matched layers in discrete contexts. *International Journal for Numerical Methods in Engineering*, 99(6):410–437, 2014.

[A9] A. Modave, C. Geuzaine, and X. Antoine. Corner treatments for high-order local absorbing boundary conditions in high-frequency acoustic scattering. *Journal of Computational Physics*, 401:109029, 2020.

[A10] A. Modave, A. Kameni, J. Lambrechts, E. Delhez, L. Pichon, and C. Geuzaine. An optimum PML for scattering problems in the time domain. *The European Physical Journal-Applied Physics*, 64(2), 2013.

[A11] A. Modave, J. Lambrechts, and C. Geuzaine. Perfectly matched layers for convex truncated domains with discontinuous Galerkin time domain simulations. *Computers & Mathematics with Applications*, 73(4):684–700, 2017.

[A12] A. Modave, A. Royer, X. Antoine, and C. Geuzaine. A non-overlapping domain decomposition method with high-order transmission conditions and cross-point treatment for Helmholtz problems. *Computer Methods in Applied Mechanics and Engineering*, 368:113162, 2020.

[A13] A. Modave, A. St-Cyr, W. A. Mulder, and T. Warburton. A nodal discontinuous Galerkin method for reverse-time migration on GPU clusters. *Geophysical Journal International*, 203(2):1419–1435, 2015.

[A14] A. Modave, A. St-Cyr, and T. Warburton. GPU performance analysis of a nodal discontinuous Galerkin method for acoustic and elastic models. *Computers & Geosciences*, 91:64–76, 2016.

[A15] A. Royer, C. Geuzaine, E. Béchet, and A. Modave. A non-overlapping domain decomposition method with perfectly matched layer transmission conditions for the Helmholtz equation. *Computer Methods in Applied Mechanics and Engineering*, 395:115006, 2022.

Other references

[1] S. Abarbanel, D. Gottlieb, and J. S. Hesthaven. Well-posed perfectly matched layers for advective acoustics. *Journal of Computational Physics*, 154(2):266–283, 1999.

[2] S. Acosta. High-order surface radiation conditions for time-harmonic waves in exterior domains. *Computer Methods in Applied Mechanics and Engineering*, 322:296–310, 2017.

[3] E. Agullo, L. Giraud, A. Gobé, M. Kuhn, S. Lanteri, and L. Moya. High order HDG method and domain decomposition solvers for frequency-domain electromagnetics. *International Journal of Numerical Modelling: Electronic Networks, Devices and Fields*, 33(2):e2678, 2020.

[4] M. Ainsworth. Dispersive and dissipative behaviour of high order discontinuous Galerkin finite element methods. *Journal of Computational Physics*, 198(1):106–130, 2004.

[5] G. B. Alvarez, A. F. D. Loula, E. G. D. do Carmo, and F. A. Rochinha. A discontinuous finite element formulation for Helmholtz equation. *Computer Methods in Applied Mechanics and Engineering*, 195(33-36):4018–4035, 2006.

[6] X. Antoine. *Conditions de Radiation sur le Bord*. PhD thesis, Université de Pau et des Pays de l'Adour, 1997.

[7] X. Antoine. Fast approximate computation of a time-harmonic scattered field using the on-surface radiation condition method. *IMA Journal of Applied Mathematics*, 66(1):83–110, 2001.

[8] X. Antoine, H. Barucq, and A. Bendali. Bayliss-Turkel-like radiation conditions on surfaces of arbitrary shape. *Journal of Mathematical Analysis and Applications*, 229(1):184–211, 1999.

[9] X. Antoine, A. Bendali, and M. Darbas. Analytic preconditioners for the boundary integral solution of the scattering of acoustic waves by open surfaces. *Journal of Computational Acoustics*, 13(03):477–498, 2005.

[10] X. Antoine, M. Darbas, and Y. Y. Lu. An improved surface radiation condition for high-frequency acoustic scattering problems. *Computer Methods in Applied Mechanics and Engineering*, 195(33):4060–4074, 2006.

[11] P. F. Antonietti, I. Perugia, and Z. Davide. Schwarz domain decomposition preconditioners for plane wave discontinuous Galerkin methods. In *Proceedings of the 10th European Conference on Numerical Mathematics and Advanced Applications (ENUMATH)*, pages 557–572. Springer, 2015.

[12] D. N. Arnold. An interior penalty finite element method with discontinuous elements. *SIAM journal on numerical analysis*, 19(4):742–760, 1982.

[13] D. N. Arnold, F. Brezzi, B. Cockburn, and L. D. Marini. Unified analysis of discontinuous Galerkin methods for elliptic problems. *SIAM journal on numerical analysis*, 39(5):1749–1779, 2002.

[14] F. Assous, P. Ciarlet, and S. Labrunie. *Mathematical Foundations of Computational Electromagnetism*. Springer, 2018.

[15] A. V. Astaneh and M. N. Guddati. A two-level domain decomposition method with accurate interface conditions for the Helmholtz problem. *International Journal for Numerical Methods in Engineering*, 107(1):74–90, 2016.

[16] S. Asvadurov, V. Druskin, M. N. Guddati, and L. Knizhnerman. On optimal finite-difference approximation of PML. *SIAM Journal on Numerical Analysis*, 41(1):287–305, 2003.

[17] D. H. Baffet, M. J. Grote, S. Imperiale, and M. Kachanovska. Energy decay and stability of a perfectly matched layer for the wave equation. *Journal of Scientific Computing*, 81(3):2237–2270, 2019.

[18] A. Bamberger, B. Engquist, L. Halpern, and P. Joly. Higher order paraxial wave equation approximations in heterogeneous media. *SIAM Journal on Applied Mathematics*, 48(1):129–154, 1988.

[19] A. Bamberger, P. Joly, and J. E. Roberts. Second-order absorbing boundary conditions for the wave equation: a solution for the corner problem. *SIAM Journal on Numerical Analysis*, 27(2):323–352, 1990.

[20] C. B. Barber, D. P. Dobkin, and H. Huhdanpaa. The quickhull algorithm for convex hulls. *ACM Transactions on Mathematical Software*, 22(4):469–483, 1996.

[21] H. Barucq, A. Bendali, J. Diaz, and S. Tordeux. Local strategies for improving the conditioning of the plane-wave Ultra-Weak Variational Formulation. *Journal of Computational Physics*, 441:110449, 2021.

[22] H. Barucq, A. Bendali, M. Fares, V. Mattesi, and S. Tordeux. A symmetric Trefftz-DG formulation based on a local boundary element method for the solution of the Helmholtz equation. *Journal of Computational Physics*, 330:1069–1092, 2017.

[23] H. Barucq, R. Djellouli, and A. Saint-Guirons. Performance assessment of a new class of local absorbing boundary conditions for elliptical- and prolate spheroidal-shaped boundaries. *Applied Numerical Mathematics*, 59(7):1467–1498, 2009.

[24] H. Barucq, R. Djellouli, and A. Saint-Guirons. Three-dimensional approximate local DtN boundary conditions for prolate spheroid boundaries. *Journal of Computational and Applied Mathematics*, 234(6):1810–1816, 2010.

[25] H. Barucq, N. Rouxelin, and S. Tordeux. Construction and analysis of a HDG+ method for the diffusive-flux formulation of the convected Helmholtz equation. 2023.

[26] U. Basu and A. K. Chopra. Perfectly matched layers for time-harmonic elastodynamics of unbounded domains: theory and finite-element implementation. *Computer Methods in Applied Mechanics and Engineering*, 192(11):1337–1375, 2003.

[27] A. Bayliss, C. I. Goldstein, and E. Turkel. An iterative method for the Helmholtz equation. *Journal of Computational Physics*, 49(3):443–457, 1983.

[28] A. Bayliss, M. Gunzburger, and E. Turkel. Boundary conditions for the numerical solution of elliptic equations in exterior regions. *SIAM Journal on Applied Mathematics*, 42(2):430–451, 1982.

[29] A. Bayliss and E. Turkel. Radiation boundary conditions for wave-like equations. *Communications on Pure and Applied Mathematics*, 33(6):707–725, 1980.

[30] E. Bécache, A.-S. Bonnet-Ben Dhia, and G. Legendre. Perfectly matched layers for the convected Helmholtz equation. *SIAM Journal on Numerical Analysis*, 42(1):409–433, 2004.

[31] E. Bécache, A.-S. Bonnet-Ben Dhia, and G. Legendre. Perfectly matched layers for time-harmonic acoustics in the presence of a uniform flow. *SIAM Journal on Numerical Analysis*, 44(3):1191–1217, 2006.

[32] E. Bécache, S. Fauqueux, and P. Joly. Stability of perfectly matched layers, group velocities and anisotropic waves. *Journal of Computational Physics*, 188(2):399–433, 2003.

[33] E. Bécache and M. Kachanovska. Stable perfectly matched layers for a class of anisotropic dispersive models. Part I: Necessary and sufficient conditions of stability. *ESAIM: Mathematical Modelling and Numerical Analysis*, 51(6):2399–2434, 2017.

[34] E. Bécache, P. G. Petropoulos, and S. D. Gedney. On the long-time behavior of unsplit perfectly matched layers. *IEEE Transactions on Antennas and Propagation*, 52(5):1335–1342, 2004.

[35] J.-D. Benamou and B. Després. A domain decomposition method for the Helmholtz equation and related optimal control problems. *Journal of Computational Physics*, 136(1):68–82, 1997.

[36] A. Bendali and Y. Boubendir. Non-overlapping domain decomposition method for a nodal finite element method. *Numerische Mathematik*, 103(4):515–537, 2006.

[37] A. Bendali, Y. Boubendir, and M. Fares. A FETI-like domain decomposition method for coupling finite elements and boundary elements in large-size problems of acoustic scattering. *Computers & structures*, 85(9):526–535, 2007.

[38] J.-P. Bérenger. A perfectly matched layer for the absorption of electromagnetic waves. *Journal of Computational Physics*, 114(2):185–200, 1994.

[39] J.-P. Bérenger. Three-dimensional perfectly matched layer for the absorption of electromagnetic waves. *Journal of Computational Physics*, 127(2):363–379, 1996.

[40] H. Bériot, A. Prinn, and G. Gabard. Efficient implementation of high-order finite elements for Helmholtz problems. *International Journal for Numerical Methods in Engineering*, 106(3):213–240, 2016.

[41] H. Bériot and M. Tournour. On the locally-conformal perfectly matched layer implementation for Helmholtz equation. In *INTER-NOISE and NOISE-CON Congress and Conference Proceedings*, pages 503–513. Institute of Noise Control Engineering, 2009.

[42] A. Bermúdez, L. Hervella-Nieto, A. Prieto, and R. Rodríguez. An exact bounded perfectly matched layer for time-harmonic scattering problems. *SIAM Journal on Scientific Computing*, 30(1):312–338, 2007.

[43] A. Bermúdez, L. Hervella-Nieto, A. Prieto, and R. Rodriguez. An optimal perfectly matched layer with unbounded absorbing function for time-harmonic acoustic scattering problems. *Journal of Computational Physics*, 223(2):469–488, 2007.

[44] D. Boffi, F. Brezzi, and M. Fortin. *Mixed Finite Element Methods and Applications*, volume 44. Springer, 2013.

[45] M. Bonazzoli and X. Claeys. Multi-domain FEM-BEM coupling for acoustic scattering. 2023. Preprint arXiv:2305.09278.

[46] M. Bonazzoli, V. Dolean, I. G. Graham, E. A. Spence, and P.-H. Tournier. Two-level preconditioners for the Helmholtz equation. In *Proceedings of the 24th International Conference on Domain Decomposition Methods*, pages 139–147. Springer, 2018.

[47] A.-S. Bonnet-Ben Dhia, S. Fliss, and Y. Tjandrawidjaja. Numerical analysis of the Half-Space Matching method with Robin traces on a convex polygonal scatterer. *Maxwell's equations: Analysis and numerics*, 24, 2019.

[48] A.-S. Bonnet-Ben Dhia, S. Fliss, and A. Tonnoir. The halfspace matching method: A new method to solve scattering problems in infinite media. *Journal of Computational and Applied Mathematics*, 338:44–68, 2018.

[49] N. Bootland, S. Borzooei, V. Dolean, and P.-H. Tournier. Numerical assessment of PML transmission conditions in a domain decomposition method for the Helmholtz equation. In *Proceedings of the 27th International Conference on Domain Decomposition Methods*, pages 445–453. Springer Cham, 2024.

[50] N. Bootland, V. Dolean, P. Jolivet, and P.-H. Tournier. A comparison of coarse spaces for Helmholtz problems in the high frequency regime. *Computers & Mathematics with Applications*, 98:239–253, 2021.

[51] N. Bootland, V. Dolean, A. Kyriakis, and J. Pestana. Analysis of parallel Schwarz algorithms for time-harmonic problems using block Toeplitz matrices. *ETNA - Electronic Transactions on Numerical Analysis*, 55:112–141, 2022.

[52] Y. Boubendir, X. Antoine, and C. Geuzaine. A quasi-optimal non-overlapping domain decomposition algorithm for the Helmholtz equation. *Journal of Computational Physics*, 231(2):262–280, 2012.

[53] Y. Boubendir and A. Bendali. Dealing with cross-points in a non-overlapping domain decomposition solution of the Helmholtz equation. In *Proceedings of the 6th International Conference on Mathematical and Numerical Aspects of Wave Propagation (WAVES)*, pages 319–324. Springer, 2003.

[54] Y. Boubendir and D. Midura. Non-overlapping domain decomposition algorithm based on modified transmission conditions for the Helmholtz equation. *Computers & Mathematics with Applications*, 75(6):1900–1911, 2018.

[55] N. Bouziani, F. Nataf, and P.-H. Tournier. A unified framework for double sweep methods for the Helmholtz equation. *Journal of Computational Physics*, page 112305, 2023.

[56] J. H. Bramble and J. E. Pasciak. Analysis of a Cartesian PML approximation to acoustic scattering problems in R2 and R3. *Journal of Computational and Applied Mathematics*, 247:209–230, 2013.

[57] G. Bunting, A. Prakash, T. Walsh, and C. Dohrmann. Parallel ellipsoidal perfectly matched layers for acoustic Helmholtz problems on exterior domains. *Journal of theoretical and computational acoustics*, 26(02):1850015, 2018.

[58] X.-C. Cai, M. A. Casarin, F. W. Elliott Jr, and O. B. Widlund. Overlapping Schwarz algorithms for solving Helmholtz's equation. *Contemporary Mathematics*, 218:391–399, 1998.

[59] M. Cenanovic, P. Hansbo, and M. G. Larson. Finite element procedures for computing normals and mean curvature on triangulated surfaces and their use for mesh refinement. *Computer Methods in Applied Mechanics and Engineering*, 372:113445, 2020.

[60] O. Cessenat and B. Després. Application of an ultra weak variational formulation of elliptic PDEs to the two-dimensional Helmholtz problem. *SIAM Journal on Numerical Analysis*, 35(1):255–299, 1998.

[61] O. Cessenat and B. Després. Using plane waves as base functions for solving time harmonic equations with the ultra weak variational formulation. *Journal of Computational Acoustics*, 11(02):227–238, 2003.

[62] S. Chaillat, M. Darbas, and F. Le Louër. Approximate local Dirichlet-to-Neumann map for three-dimensional time-harmonic elastic waves. *Computer Methods in Applied Mechanics and Engineering*, 297:62–83, 2015.

[63] S. Chaillat, M. Darbas, and F. Le Louër. Fast iterative boundary element methods for high-frequency scattering problems in 3D elastodynamics. *Journal of Computational Physics*, 341:429–446, 2017.

[64] T. Chaumont-Frelet, M. J. Grote, S. Lanteri, and J. H. Tang. A controllability method for maxwell's equations. *SIAM Journal on Scientific Computing*, 44(6):A3700–A3727, 2022.

[65] H. Chen, P. Lu, and X. Xu. A hybridizable discontinuous Galerkin method for the Helmholtz equation with high wave number. *SIAM Journal on Numerical Analysis*, 51(4):2166–2188, 2013.

[66] W. Chew, J. Jin, and E. Michielssen. Complex coordinate stretching as a generalized absorbing boundary condition. *Microwave and Optical Technology Letters*, 15(6):363–369, 1997.

[67] W. Chew and Q. Liu. Perfectly matched layers for elastodynamics: a new absorbing boundary condition. *Journal of Computational Acoustics*, 4(04):341–359, 1996.

[68] W. C. Chew and W. H. Weedon. A 3D perfectly matched medium from modified Maxwell's equations with stretched coordinates. *Microwave and optical technology letters*, 7(13):599–604, 1994.

[69] D. Chicaud. *Analysis of time-harmonic electromagnetic problems in elliptic anisotropic media*. PhD thesis, Institut polytechnique de Paris, France, 2021.

[70] D. Chicaud and P. Ciarlet Jr. Analysis of time-harmonic Maxwell impedance problems in anisotropic media. *SIAM Journal on Mathematical Analysis*, 55(3):1969–2000, 2023.

[71] R. Cimpeanu, A. Martinsson, and M. Heil. A parameter-free perfectly matched layer formulation for the finite-element-based solution of the Helmholtz equation. *Journal of Computational Physics*, 296:329–347, 2015.

[72] X. Claeys. Non-local variant of the Optimised Schwarz method for arbitrary non-overlapping subdomain partitions. *ESAIM: Mathematical Modelling and Numerical Analysis*, 55(2):429–448, 2021.

[73] X. Claeys. Nonlocal optimized Schwarz method for the Helmholtz equation with physical boundaries. *SIAM Journal on Mathematical Analysis*, 55(6):7490–7512, 2023.

[74] X. Claeys, F. Collino, and E. Parolin. Nonlocal optimized Schwarz methods for time-harmonic electromagnetics. *Advances in Computational Mathematics*, 48(6):72, 2022.

[75] X. Claeys and E. Parolin. Robust treatment of cross-points in optimized Schwarz methods. *Numerische Mathematik*, pages 1–38, 2022.

[76] R. Clayton and B. Engquist. Absorbing boundary conditions for acoustic and elastic wave equations. *Bulletin of the seismological society of America*, 67(6):1529–1540, 1977.

[77] B. Cockburn. Static condensation, hybridization, and the devising of the HDG methods. *Building Bridges: Connections and Challenges in Modern Approaches to Numerical Partial Differential Equations*, pages 129–177, 2016.

[78] B. Cockburn. Hybridizable discontinuous Galerkin methods for second-order elliptic problems: overview, a new result and open problems. *Japan Journal of Industrial and Applied Mathematics*, 40(3):1637–1676, 2023.

[79] B. Cockburn, B. Dong, and J. Guzmán. A superconvergent LDG-hybridizable Galerkin method for second-order elliptic problems. *Mathematics of Computation*, 77(264):1887–1916, 2008.

[80] B. Cockburn, J. Gopalakrishnan, and R. Lazarov. Unified hybridization of discontinuous Galerkin, mixed, and continuous Galerkin methods for second order elliptic problems. *SIAM Journal on Numerical Analysis*, 47(2):1319–1365, 2009.

[81] B. Cockburn, G. E. Karniadakis, and C.-W. Shu. *Discontinuous Galerkin Methods: Theory, Computation and Applications*. Springer Berlin, Heidelberg, 2000.

[82] F. Collino. Conditions absorbantes d'ordre élevé pour des modèles de propagation d'onde dans des domaines rectangulaires. Technical Report 1790, INRIA, 1992.

[83] F. Collino. Conditions absorbantes d'ordre élevé pour les équations de Maxwell dans des domaines rectangulaires. Technical Report 2932, INRIA, 1993.

[84] F. Collino, S. Ghanemi, and P. Joly. Domain decomposition method for harmonic wave propagation: a general presentation. *Computer Methods in Applied Mechanics and Engineering*, 184(2-4):171–211, 2000.

[85] F. Collino, P. Joly, and M. Lecouvez. Exponentially convergent non overlapping domain decomposition methods for the Helmholtz equation. *ESAIM: Mathematical Modelling and Numerical Analysis*, 54(3):775–810, 2020.

[86] F. Collino and P. Monk. The perfectly matched layer in curvilinear coordinates. *SIAM Journal on Scientific Computing*, 19(6):2061–2090, 1998.

[87] F. Collino and P. B. Monk. Optimizing the perfectly matched layer. *Computer Methods in Applied Mechanics and Engineering*, 164(1-2):157–171, 1998.

[88] F. Collino and C. Tsogka. Application of the perfectly matched absorbing layer model to the linear elastodynamic problem in anisotropic heterogeneous media. *Geophysics*, 66(1):294–307, 2001.

[89] L. Conen, V. Dolean, R. Krause, and F. Nataf. A coarse space for heterogeneous Helmholtz problems based on the Dirichlet-to-Neumann operator. *Journal of Computational and Applied Mathematics*, 271:83–99, 2014.

[90] J. Cui and W. Zhang. An analysis of HDG methods for the Helmholtz equation. *IMA Journal of Numerical Analysis*, 34(1):279–295, 2014.

[91] R. Dai. *Generalized sweeping preconditioners for domain decomposition methods applied to Helmholtz problems*. PhD thesis, Université de Liège and Université catholique de Louvain, Belgique, 2021.

[92] M. Darbas, E. Darrigrand, and Y. Lafranche. Combining analytic preconditioner and fast multipole method for the 3-D Helmholtz equation. *Journal of Computational Physics*, 236:289–316, 2013.

[93] G. Darblade, R. Baraille, X. Carton, D. Pinchon, et al. Conditions limites non réfléchissantes pour un modele de Saint-Venant bidimensionnel barotrope linéarisé. *Comptes Rendus de l'Académie des Sciences – Series I-Mathematics*, 324(4):485–490, 1997.

[94] A. de La Bourdonnaye, C. Farhat, A. Macedo, F. Magoules, F.-X. Roux, et al. A non-overlapping domain decomposition method for the exterior Helmholtz problem. *Contemporary Mathematics*, 218:42–66, 1998.

[95] E. Demaldent and S. Imperiale. Perfectly matched transmission problem with absorbing layers: Application to anisotropic acoustics in convex polygonal domains. *International Journal for Numerical Methods in Engineering*, 96(11):689–711, 2013.

[96] L. Demkowicz, J. Gopalakrishnan, I. Muga, and J. Zitelli. Wavenumber explicit analysis of a dpg method for the multidimensional Helmholtz equation. *Computer Methods in Applied Mechanics and Engineering*, 213:126–138, 2012.

[97] B. Després. Domain decomposition method and the Helmholtz problem. In G. Cohen, L. Halpern, and P. Joly, editors, *Proceedings of the 1st International Conference on Mathematical and Numerical Aspects of Wave Propagation (WAVES)*, pages 44–52. SIAM, 1991.

[98] B. Després. *Une méthodes de décomposition de domaine pour les problèmes de propagation d'ondes en régime harmonique. Le théorème de Borg pour l'équation de Hill vectorielle.* PhD thesis, Université de Paris-IX, 1991.

[99] B. Després. Domain decomposition method and the Helmholtz problem (part II). In *Proceedings of the 2nd International Conference on Mathematical and Numerical Aspects of Wave Propagation (WAVES)*, pages 197–206. SIAM, 1993.

[100] B. Després, A. Nicolopoulos, and B. Thierry. Corners and stable optimized domain decomposition methods for the Helmholtz problem. *Numerische Mathematik*, 149(4):779–818, 2021.

[101] B. Després, A. Nicolopoulos, and B. Thierry. Optimized transmission conditions in domain decomposition methods with cross-points for Helmholtz equation. *SIAM Journal on Numerical Analysis*, 60(5):2482–2507, 2022.

[102] D. A. Di Pietro and A. Ern. *Mathematical Aspects of Discontinuous Galerkin Methods*, volume 69. Springer Science & Business Media, 2011.

[103] V. Dolean, P. Jolivet, and F. Nataf. *An Introduction to Domain Decomposition Methods: Algorithms, Theory, and Parallel Implementation*, volume 144. SIAM, 2015.

[104] V. Dolean, S. Lanteri, and R. Perrussel. A domain decomposition method for solving the three-dimensional time-harmonic Maxwell equations discretized by discontinuous Galerkin methods. *Journal of Computational Physics*, 227(3):2044–2072, 2008.

[105] V. Druskin, S. Güttel, and L. Knizhnerman. Near-optimal perfectly matched layers for indefinite Helmholtz problems. *SIAM Review*, 58(1):90–116, 2016.

[106] P. Dular, C. Geuzaine, F. Henrotte, and W. Legros. A general environment for the treatment of discrete problems and its application to the finite element method. *IEEE Transactions on Magnetics*, 34(5):3395–3398, 1998.

[107] V. Dwarka and C. Vuik. Scalable convergence using two-level deflation preconditioning for the Helmholtz equation. *SIAM Journal on Scientific Computing*, 42(2):A901–A928, 2020.

[108] M. El Bouajaji, X. Antoine, and C. Geuzaine. Approximate local magnetic-to-electric surface operators for time-harmonic Maxwell's equations. *Journal of Computational Physics*, 279:241–260, 2014.

[109] A. El Kacimi, O. Laghrouche, D. Ouazar, M. Mohamed, M. Seaid, and J. Trevelyan. Enhanced conformal perfectly matched layers for Bernstein–Bézier finite element modelling of short wave scattering. *Computer Methods in Applied Mechanics and Engineering*, 355:614–638, 2019.

[110] B. Engquist and A. Majda. Absorbing boundary conditions for numerical simulation of waves. *Proceedings of the National Academy of Sciences*, 74(5):1765–1766, 1977.

[111] B. Engquist and A. Majda. Radiation boundary conditions for acoustic and elastic wave calculations. *Communications on Pure and Applied Mathematics*, 32(3):313–357, 1979.

[112] B. Engquist and L. Ying. Sweeping preconditioner for the Helmholtz equation: moving perfectly matched layers. *Multiscale Modeling & Simulation*, 9(2):686–710, 2011.

[113] Y. A. Erlangga. Advances in iterative methods and preconditioners for the Helmholtz equation. *Archives of Computational Methods in Engineering*, 15:37–66, 2008.

[114] Y. A. Erlangga, L. García Ramos, and R. Nabben. The multilevel Krylov-multigrid method for the Helmholtz equation preconditioned by the shifted Laplacian. *Modern Solvers for Helmholtz Problems*, pages 113–139, 2017.

[115] Y. A. Erlangga, C. W. Oosterlee, and C. Vuik. A novel multigrid based preconditioner for heterogeneous Helmholtz problems. *SIAM Journal on Scientific Computing*, 27(4):1471–1492, 2006.

[116] Y. A. Erlangga, C. Vuik, and C. W. Oosterlee. On a class of preconditioners for solving the Helmholtz equation. *Applied Numerical Mathematics*, 50(3-4):409–425, 2004.

[117] O. G. Ernst and M. J. Gander. Why it is difficult to solve Helmholtz problems with classical iterative methods. In *Numerical Analysis of Multiscale Problems*, pages 325–363. Springer, 2012.

[118] C. Farhat, P. Avery, R. Tezaur, and J. Li. FETI-DPH: a dual-primal domain decomposition method for acoustic scattering. *Journal of Computational Acoustics*, 13(03):499–524, 2005.

[119] C. Farhat, I. Harari, and U. Hetmaniuk. A discontinuous Galerkin method with Lagrange multipliers for the solution of Helmholtz problems in the mid-frequency regime. *Computer Methods in Applied Mechanics and Engineering*, 192(11-12):1389–1419, 2003.

[120] C. Farhat, A. Macedo, and M. Lesoinne. A two-level domain decomposition method for the iterative solution of high frequency exterior Helmholtz problems. *Numerische Mathematik*, 85(2):283–308, 2000.

[121] C. Farhat, A. Macedo, M. Lesoinne, F.-X. Roux, F. Magoulés, and A. de La Bourdonnaie. Two-level domain decomposition methods with Lagrange multipliers for the fast iterative solution of acoustic scattering problems. *Computer Methods in Applied Mechanics and Engineering*, 184(2-4):213–239, 2000.

[122] C. Farhat, R. Tezaur, and J. Toivanen. A domain decomposition method for discontinuous Galerkin discretizations of Helmholtz problems with plane waves and Lagrange multipliers. *International Journal for Numerical Methods in Engineering*, 78(13):1513–1531, 2009.

[123] X. Feng and H. Wu. Discontinuous Galerkin methods for the Helmholtz equation with large wave number. *SIAM Journal on Numerical Analysis*, 47(4):2872–2896, 2009.

[124] X. Feng and H. Wu. hp-discontinuous Galerkin methods for the Helmholtz equation with large wave number. *Mathematics of Computation*, 80(276):1997–2024, 2011.

[125] X. Feng and Y. Xing. Absolutely stable local discontinuous Galerkin methods for the Helmholtz equation with large wave number. *Mathematics of Computation*, 82(283):1269–1296, 2013.

[126] S. François, M. Schevenels, G. Lombaert, and G. Degrande. A two-and-a-half-dimensional displacement-based PML for elastodynamic wave propagation. *International Journal for Numerical Methods in Engineering*, 90(7):819–837, 2012.

[127] T. Frankel. *The Geometry of Physics: An Introduction*. Cambridge University Press, 2011.

[128] G. Gabard. Discontinuous Galerkin methods with plane waves for time-harmonic problems. *Journal of Computational Physics*, 225(2):1961–1984, 2007.

[129] M. J. Gander et al. Schwarz methods over the course of time. *Electronic Transactions on Numerical Analysis*, 31(5):228–255, 2008.

[130] M. J. Gander, I. G. Graham, and E. A. Spence. Applying GMRES to the Helmholtz equation with shifted Laplacian preconditioning: what is the largest shift for which wavenumber-independent convergence is guaranteed? *Numerische Mathematik*, 131(3):567–614, 2015.

[131] M. J. Gander and L. Halpern. A simple finite difference discretization for Ventcell transmission conditions at cross points. In *Proceedings of the 26th International Conference on Domain Decomposition Methods*, pages 257–264. Springer, 2023.

[132] M. J. Gander, L. Halpern, and F. Magoules. An optimized Schwarz method with two-sided Robin transmission conditions for the Helmholtz equation. *International journal for numerical methods in fluids*, 55(2):163–175, 2007.

[133] M. J. Gander and F. Kwok. Best Robin parameters for optimized Schwarz methods at cross points. *SIAM Journal on Scientific Computing*, 34(4):A1849–A1879, 2012.

[134] M. J. Gander and F. Kwok. On the applicability of Lions' energy estimates in the analysis of discrete optimized Schwarz methods with cross points. In *Proceedings of the 20th International Conference on Domain Decomposition Methods*, pages 475–483. Springer, 2013.

[135] M. J. Gander, F. Magoules, and F. Nataf. Optimized Schwarz methods without overlap for the Helmholtz equation. *SIAM Journal on Scientific Computing*, 24(1):38–60, 2002.

[136] M. J. Gander and K. Santugini. Cross-points in domain decomposition methods with a finite element discretization. *Electronic Transactions on Numerical Analysis*, 45:219–240, 2016.

[137] M. J. Gander and H. Zhang. Optimized Schwarz methods with overlap for the Helmholtz equation. *SIAM Journal on Scientific Computing*, 38(5):A3195–A3219, 2016.

[138] M. J. Gander and H. Zhang. A class of iterative solvers for the Helmholtz equation: Factorizations, sweeping preconditioners, source transfer, single layer potentials, polarized traces, and optimized Schwarz methods. *SIAM Review*, 61(1):3–76, 2019.

[139] M. J. Gander and H. Zhang. Schwarz methods by domain truncation. *Acta Numerica*, 31:1–134, 2022.

[140] M. Ganesh and C. Morgenstern. High-order FEM domain decomposition models for high-frequency wave propagation in heterogeneous media. *Computers & Mathematics with Applications*, 75(6):1961–1972, 2018.

[141] S. D. Gedney. An anisotropic PML absorbing media for the FDTD simulation of fields in lossy and dispersive media. *Electromagnetics*, 16(4):399–415, 1996.

[142] C. Geuzaine and J.-F. Remacle. Gmsh: A 3-D finite element mesh generator with built-in pre-and post-processing facilities. *International Journal for Numerical Methods in Engineering*, 79(11):1309–1331, 2009.

[143] G. Giorgiani, S. Fernández-Méndez, and A. Huerta. Hybridizable discontinuous Galerkin p-adaptivity for wave propagation problems. *International Journal for Numerical Methods in Fluids*, 72(12):1244–1262, 2013.

[144] C. J. Gittelson, R. Hiptmair, and I. Perugia. Plane wave discontinuous Galerkin methods: analysis of the h-version. *ESAIM: Mathematical Modelling and Numerical Analysis*, 43(2):297–331, 2009.

[145] D. Givoli. Non-reflecting boundary conditions. *Journal of Computational Physics*, 94(1):1–29, 1991.

[146] D. Givoli. *Numerical Methods for Problems in Infinite Domains*. Elsevier Science Limited, 1992.

[147] D. Givoli. Computational absorbing boundaries. In *Computational Acoustics of Noise Propagation in Fluids-Finite and Boundary Element Methods*, pages 145–166. Springer, 2008.

[148] D. Givoli, T. Hagstrom, and I. Patlashenko. Finite element formulation with high-order absorbing boundary conditions for time-dependent waves. *Computer Methods in Applied Mechanics and Engineering*, 195(29):3666–3690, 2006.

[149] D. Givoli and B. Neta. High-order non-reflecting boundary scheme for time-dependent waves. *Journal of Computational Physics*, 186(1):24–46, 2003.

[150] D. Givoli, I. Patlashenko, and J. B. Keller. High-order boundary conditions and finite elements for infinite domains. *Computer Methods in Applied Mechanics and Engineering*, 143(1):13–39, 1997.

[151] S. Gong, M. J. Gander, I. G. Graham, D. Lafontaine, and E. A. Spence. Convergence of parallel overlapping domain decomposition methods for the Helmholtz equation. *Numerische Mathematik*, 152(2):259–306, 2022.

[152] S. Gong, I. Graham, and E. Spence. Convergence of restricted additive Schwarz with impedance transmission conditions for discretised Helmholtz problems. *Mathematics of Computation*, 92(339):175–215, 2023.

[153] J. Gopalakrishnan, S. Lanteri, N. Olivares, and R. Perrussel. Stabilization in relation to wavenumber in HDG methods. *Advanced Modeling and Simulation in Engineering Sciences*, 2(1):1–24, 2015.

[154] P. Gosselet and C. Rey. Non-overlapping domain decomposition methods in structural mechanics. *Archives of Computational Methods in Engineering*, 13:515–572, 2006.

[155] I. Graham, E. Spence, and E. Vainikko. Domain decomposition preconditioning for high-frequency Helmholtz problems with absorption. *Mathematics of Computation*, 86(307):2089–2127, 2017.

[156] I. G. Graham, E. A. Spence, and J. Zou. Domain decomposition with local impedance conditions for the Helmholtz equation with absorption. *SIAM Journal on Numerical Analysis*, 58(5):2515–2543, 2020.

[157] R. Griesmaier and P. Monk. Error analysis for a hybridizable discontinuous Galerkin method for the Helmholtz equation. *Journal of Scientific Computing*, 49(3):291–310, 2011.

[158] Z. Guan-Quan. High-order approximation of one way wave equations. *J. Comput. Math*, 3:90–97, 1985.

[159] M. N. Guddati and K.-W. Lim. Continued fraction absorbing boundary conditions for convex polygonal domains. *International Journal for Numerical Methods in Engineering*, 66(6):949–977, 2006.

[160] M. N. Guddati and J. L. Tassoulas. Continued-fraction absorbing boundary conditions for the wave equation. *Journal of Computational Acoustics*, 8(01):139–156, 2000.

[161] T. Hagstrom. Radiation boundary conditions for the numerical simulation of waves. *Acta Numerica*, 8:47–106, 1999.

[162] T. Hagstrom, D. Givoli, D. Rabinovich, and J. Bielak. The double absorbing boundary method. *Journal of Computational Physics*, 259:220–241, 2014.

[163] T. Hagstrom and S. Kim. Complete radiation boundary conditions for the Helmholtz equation I: waveguides. *Numerische Mathematik*, 141(4):917–966, 2019.

[164] T. Hagstrom and S. Kim. Complete radiation boundary conditions for the Helmholtz equation II: domains with corners. *Numerische Mathematik*, pages 1–51, 2023.

[165] T. Hagstrom, A. Mar-Or, and D. Givoli. High-order local absorbing conditions for the wave equation: Extensions and improvements. *Journal of Computational Physics*, 227(6):3322–3357, 2008.

[166] T. Hagstrom, R. P. Tewarson, and A. Jazcilevich. Numerical experiments on a domain decomposition algorithm for nonlinear elliptic boundary value problems. *Applied Mathematics Letters*, 1(3):299–302, 1988.

[167] T. Hagstrom and T. Warburton. A new auxiliary variable formulation of high-order local radiation boundary conditions: corner compatibility conditions and extensions to first-order systems. *Wave Motion*, 39(4):327–338, 2004.

[168] T. Hagstrom and T. Warburton. Complete radiation boundary conditions: minimizing the long time error growth of local methods. *SIAM Journal on Numerical Analysis*, 47(5):3678–3704, 2009.

[169] T. Hagstrom, T. Warburton, and D. Givoli. Radiation boundary conditions for time-dependent waves based on complete plane wave expansions. *Journal of Computational and Applied Mathematics*, 234(6):1988–1995, 2010.

[170] M. Halla, M. Kachanovska, and M. Wess. Radial perfectly matched layers and infinite elements for the anisotropic wave equation. 2024. Preprint arXiv:2401.13483.

[171] L. Halpern and L. N. Trefethen. Wide-angle one-way wave equations. *The Journal of the Acoustical Society of America*, 84(4):1397–1404, 1988.

[172] I. Harari and U. Albocher. Studies of FE/PML for exterior problems of time-harmonic elastic waves. *Computer Methods in Applied Mechanics and Engineering*, 195(29-32):3854–3879, 2006.

[173] I. Harari, M. Slavutin, and E. Turkel. Analytical and numerical studies of a finite element PML for the Helmholtz equation. *Journal of Computational Acoustics*, 8(01):121–137, 2000.

[174] F. D. Hastings, J. B. Schneider, and S. L. Broschat. Application of the perfectly matched layer (pml) absorbing boundary condition to elastic wave propagation. *The Journal of the Acoustical Society of America*, 100(5):3061–3069, 1996.

[175] G. W. Hedstrom. Nonreflecting boundary conditions for nonlinear hyperbolic systems. *Journal of Computational Physics*, 30(2):222–237, 1979.

[176] J. S. Hesthaven and T. Warburton. *Nodal Discontinuous Galerkin Methods: Algorithms, Analysis, and Applications*. Springer Science & Business Media, 2007.

[177] R. L. Higdon. Absorbing boundary conditions for difference approximations to the multidimensional wave equation. *Mathematics of computation*, 47(176):437–459, 1986.

[178] R. L. Higdon. Absorbing boundary conditions for elastic waves. *Geophysics*, 56(2):231–241, 1991.

[179] R. Hiptmair, A. Moiola, and I. Perugia. A survey of Trefftz methods for the Helmholtz equation. *Building Bridges: Connections and Challenges in Modern Approaches to Numerical Partial Differential Equations*, pages 237–279, 2016.

[180] T. Hohage and L. Nannen. Hardy space infinite elements for scattering and resonance problems. *SIAM Journal on Numerical Analysis*, 47(2):972–996, 2009.

[181] R. Holland and J. W. Williams. Total-field versus scattered-field finite-difference codes: A comparative assessment. *IEEE Transactions on Nuclear Science*, 30(6):4583–4588, 1983.

[182] R. H. Hoppe and N. Sharma. Convergence analysis of an adaptive interior penalty discontinuous Galerkin method for the Helmholtz equation. *IMA Journal of Numerical Analysis*, 33(3):898–921, 2013.

[183] P. Houston, I. Perugia, A. Schneebeli, and D. Schötzau. Interior penalty method for the indefinite time-harmonic Maxwell equations. *Numerische Mathematik*, 100:485–518, 2005.

[184] F. Q. Hu. On absorbing boundary conditions for linearized Euler equations by a perfectly matched layer. *Journal of Computational Physics*, 129(1):201–219, 1996.

[185] T. Huttunen, J. P. Kaipio, and P. Monk. The perfectly matched layer for the ultra-weak variational formulation of the 3D Helmholtz equation. *International Journal for Numerical Methods in Engineering*, 61(7):1072–1092, 2004.

[186] T. Huttunen, P. Monk, and J. P. Kaipio. Computational aspects of the ultra-weak variational formulation. *Journal of Computational Physics*, 182(1):27–46, 2002.

[187] F. Ihlenburg. *Finite Element Analysis of Acoustic Scattering*. Springer, 1998.

[188] L.-M. Imbert-Gérard. Amplitude-based generalized plane waves: New quasi-Trefftz functions for scalar equations in two dimensions. *SIAM Journal on Numerical Analysis*, 59(3):1663–1686, 2021.

[189] M. Israeli and S. A. Orszag. Approximation of radiation boundary conditions. *Journal of Computational Physics*, 41(1):115–135, 1981.

[190] P. Joly, S. Lohrengel, and O. Vacus. Un résultat d'existence et d'unicité pour l'équation de Helmholtz avec conditions aux limites absorbantes d'ordre 2. *Comptes Rendus de l'Académie des Sciences – Series I-Mathematics*, 329(3):193–198, 1999.

[191] D. S. Jones. An approximate boundary condition in acoustics. *Journal of Sound Vibration*, 121(1):37–45, 1988.

[192] D. Justo, T. Warburton, and T. Hagstrom. Solving scattering problems for Maxwell's equations using polygonal artificial boundaries. In *Proceedings of the 7th International Conference on Mathematical and Numerical Aspects of Wave Propagation (WAVES)*, pages 71–73, 2005.

[193] G. E. Karniadakis, G. Karniadakis, and S. Sherwin. *Spectral/hp Element Methods for Computational Fluid Dynamics*. Oxford University Press on Demand, 2005.

[194] R. Kechroud, X. Antoine, and A. Soulaimani. Numerical accuracy of a Padé-type non-reflecting boundary condition for the finite element solution of acoustic scattering problems at high-frequency. *International Journal for Numerical Methods in Engineering*, 64(10):1275–1302, 2005.

[195] S. Kim and J. E. Pasciak. Analysis of a Cartesian PML approximation to acoustic scattering problems in R2. *Journal of Mathematical Analysis and Applications*, 370(1):168–186, 2010.

[196] S. Kim and H. Zhang. Optimized Schwarz method with complete radiation transmission conditions for the Helmholtz equation in waveguides. *SIAM Journal on Numerical Analysis*, 53(3):1537–1558, 2015.

[197] J.-H. Kimn and M. Sarkis. Restricted overlapping balancing domain decomposition methods and restricted coarse problems for the Helmholtz problem. *Computer Methods in Applied Mechanics and Engineering*, 196(8):1507–1514, 2007.

[198] A. Klöckner, T. Warburton, J. Bridge, and J. S. Hesthaven. Nodal discontinuous Galerkin methods on graphics processors. *Journal of Computational Physics*, 228(21):7863–7882, 2009.

[199] D. Komatitsch and J. Tromp. A perfectly matched layer absorbing boundary condition for the second-order seismic wave equation. *Geophysical Journal International*, 154(1):146–153, 2003.

[200] M. Kuzuoglu and R. Mittra. Frequency dependence of the constitutive parameters of causal perfectly matched anisotropic absorbers. *IEEE Microwave and Guided Wave Letters*, 6(12):447–449, 1996.

[201] J. LaGrone and T. Hagstrom. Double absorbing boundaries for finite-difference time-domain electromagnetics. *Journal of Computational Physics*, 326:650–665, 2016.

[202] D. Lahaye, J. Tang, and K. Vuik. *Modern Solvers for Helmholtz Problems*. Springer, 2017.

[203] D. Lahaye and C. Vuik. How to choose the shift in the shifted Laplace preconditioner for the Helmholtz equation combined with deflation. *Modern Solvers for Helmholtz Problems*, pages 85–112, 2017.

[204] U. Langer and O. Steinbach. Coupled boundary and finite element tearing and interconnecting methods. In *Proceedings of the 15th International Conference on Domain Decomposition Methods*, pages 83–97. Springer, 2005.

[205] M. Lassas, J. Liukkonen, and E. Somersalo. Complex Riemannian metric and absorbing boundary conditions. *Journal des Mathématiques Pures et Appliquées*, 80(7):739–768, 2001.

[206] M. Lassas and E. Somersalo. On the existence and convergence of the solution of PML equations. *Computing*, 60(3):229–241, 1998.

[207] M. Lassas and E. Somersalo. Analysis of the PML equations in general convex geometry. *Proceedings of the Royal Society of Edinburgh Section A: Mathematics*, 131(5):1183–1207, 2001.

[208] M. Lecouvez. *Méthodes itératives de décomposition de domaine sans recouvrement avec convergence géométrique pour l'équation de Helmholtz*. PhD thesis, Ecole Polytechnique, 2015.

[209] M. Lecouvez, B. Stupfel, P. Joly, and F. Collino. Quasi-local transmission conditions for non-overlapping domain decomposition methods for the Helmholtz equation. *Comptes Rendus Physique*, 15(5):403–414, 2014.

[210] W. Leng and L. Ju. An additive overlapping domain decomposition method for the Helmholtz equation. *SIAM Journal on Scientific Computing*, 41(2):A1252–A1277, 2019.

[211] W. Leng and L. Ju. Trace transfer-based diagonal sweeping domain decomposition method for the Helmholtz equation: Algorithms and convergence analysis. *Journal of Computational Physics*, 455:110980, 2022.

[212] L. Li, S. Lanteri, and R. Perrussel. Numerical investigation of a high order hybridizable discontinuous Galerkin method for 2d time-harmonic Maxwell's equations. *COMPEL*, 32(3):1112–1138, 2013.

[213] L. Li, S. Lanteri, and R. Perrussel. A hybridizable discontinuous Galerkin method combined to a Schwarz algorithm for the solution of 3d time-harmonic Maxwell's equation. *Journal of Computational Physics*, 256:563–581, 2014.

[214] E. L. Lindman. "Free-space" boundary conditions for the time-dependent wave equation. *Journal of Computational Physics*, 18(1):66–78, 1975.

[215] P.-L. Lions. On the Schwarz alternating method. III: a variant for nonoverlapping subdomains. In *Proceedings of the 3rd International Conference on Domain Decomposition Methods*, pages 202–223. SIAM Philadelphia, 1990.

[216] S. Loisel. Condition number estimates for the nonoverlapping optimized Schwarz method and the 2-Lagrange multiplier method for general domains and cross points. *SIAM Journal on Numerical Analysis*, 51(6):3062–3083, 2013.

[217] A. F. Loula, G. B. Alvarez, E. G. do Carmo, and F. A. Rochinha. A discontinuous finite element method at element level for Helmholtz equation. *Computer Methods in Applied Mechanics and Engineering*, 196(4-6):867–878, 2007.

[218] Y. Y. Lu. A complex coefficient rational approximation of $\sqrt{1+x}$. *Applied numerical mathematics*, 27(2):141–154, 1998.

[219] T. Luostari, T. Huttunen, and P. Monk. Improvements for the ultra weak variational formulation. *International Journal for Numerical Methods in Engineering*, 94(6):598–624, 2013.

[220] E. Magid, O. Soldea, and E. Rivlin. A comparison of Gaussian and mean curvature estimation methods on triangular meshes of range image data. *Computer Vision and Image Understanding*, 107(3):139–159, 2007.

[221] P. Marchner, X. Antoine, C. Geuzaine, and H. Bériot. Construction and numerical assessment of local absorbing boundary conditions for heterogeneous time-harmonic acoustic problems. *SIAM Journal on Applied Mathematics*, 82(2):476–501, 2022.

[222] P. Marchner, H. Bériot, X. Antoine, and C. Geuzaine. Stable perfectly matched layers with Lorentz transformation for the convected Helmholtz equation. *Journal of Computational Physics*, 433:110180, 2021.

[223] T. P. Mathew. *Domain Decomposition Methods for the Numerical Solution of Partial Differential Equations*. Springer, 2008.

[224] V. Mattesi, M. Darbas, and C. Geuzaine. A high-order absorbing boundary condition for 2D time-harmonic elastodynamic scattering problems. *Computers & Mathematics with Applications*, 77(6):1703–1721, 2019.

[225] P. J. Matuszyk and L. F. Demkowicz. Parametric finite elements, exact sequences and perfectly matched layers. *Computational Mechanics*, 51(1):35–45, 2013.

[226] M. Medvinsky, S. Tsynkov, and E. Turkel. Direct implementation of high order BGT artificial boundary conditions. *Journal of Computational Physics*, 376:98–128, 2019.

[227] J. M. Melenk, A. Parsania, and S. Sauter. General DG-methods for highly indefinite Helmholtz problems. *Journal of Scientific Computing*, 57:536–581, 2013.

[228] F. A. Milinazzo, C. A. Zala, and G. H. Brooke. Rational square-root approximations for parabolic equation algorithms. *The Journal of the Acoustical Society of America*, 101(2):760–766, 1997.

[229] P. Monk, J. Schöberl, and A. Sinwel. Hybridizing Raviart-thomas elements for the Helmholtz equation. *Electromagnetics*, 30(1-2):149–176, 2010.

[230] L. Nannen and M. Wess. Complex-scaled infinite elements for resonance problems in heterogeneous open systems. *Advances in Computational Mathematics*, 48(2):8, 2022.

[231] F. Nataf. On the use of open boundary conditions in block Gauss-Seidel methods for the convection-diffusion equations. Technical report, CMAP, Ecole Polytechnique, France, 1993.

[232] F. Nataf. A new approach to perfectly matched layers for the linearized euler system. *Journal of Computational Physics*, 214(2):757–772, 2006.

[233] F. Nataf and F. Nier. Convergence rate of some domain decomposition methods for overlapping and nonoverlapping subdomains. *Numerische Mathematik*, 75(3):357–377, 1997.

[234] F. Nataf, F. Rogier, and E. de Sturler. Optimal interface conditions for domain decomposition methods. Technical report, CMAP, Ecole Polytechnique, France, 1994.

[235] I. Navon, B. Neta, and M. Hussaini. A perfectly matched layer approach to the linearized shallow water equations models. *Monthly Weather Review*, 132(6):1369–1378, 2004.

[236] N. C. Nguyen, J. Peraire, and B. Cockburn. High-order implicit hybridizable discontinuous Galerkin methods for acoustics and elastodynamics. *Journal of Computational Physics*, 230(10):3695–3718, 2011.

[237] N. C. Nguyen, J. Peraire, and B. Cockburn. Hybridizable discontinuous Galerkin methods for the time-harmonic maxwell's equations. *Journal of Computational Physics*, 230(19):7151–7175, 2011.

[238] N. C. Nguyen, J. Peraire, F. Reitich, and B. Cockburn. A phase-based hybridizable discontinuous Galerkin method for the numerical solution of the Helmholtz equation. *Journal of Computational Physics*, 290:318–335, 2015.

[239] A. Nicolopoulos. *Formulations variationnelles d'équations de Maxwell résonantes et problèmes aux coins en propagation d'ondes*. PhD thesis, Sorbonne Université, 2019.

[240] O. Ozgun and M. Kuzuoglu. Near-field performance analysis of locally-conformal perfectly matched absorbers via Monte Carlo simulations. *Journal of Computational Physics*, 227(2):1225–1245, 2007.

[241] O. Ozgun and M. Kuzuoglu. Non-Maxwellian locally-conformal PML absorbers for finite element mesh truncation. *IEEE Transactions on Antennas and Propagation*, 55(3):931–937, 2007.

[242] E. Parolin. *Non-overlapping domain decomposition methods with non-local transmission operators for harmonic wave propagation problems*. PhD thesis, Institut Polytechnique de Paris, 2020.

[243] E. Parolin, D. Huybrechs, and A. Moiola. Stable approximation of helmholtz solutions in the disk by evanescent plane waves. *ESAIM: Mathematical Modelling and Numerical Analysis*, 57(6):3499–3536, 2023.

[244] C. Pechstein. *Finite and Boundary Element Tearing and Interconnecting Solvers for Multiscale Problems*, volume 90. Springer Science & Business Media, 2012.

[245] Z. Peng and J.-F. Lee. Non-conformal domain decomposition method with second-order transmission conditions for time-harmonic electromagnetics. *Journal of Computational Physics*, 229(16):5615–5629, 2010.

[246] S. Pernet, M. Sirdey, and S. Tordeux. Ultra-weak variational formulation for heterogeneous Maxwell problem in the context of high performance computing. *ESAIM: Proceedings and Surveys*, 75:96–121, 2023.

[247] I. Perugia, D. Schötzau, and P. Monk. Stabilized interior penalty methods for the time-harmonic Maxwell equations. *Computer Methods in Applied Mechanics and Engineering*, 191(41-42):4675–4697, 2002.

[248] S. Petrides and L. F. Demkowicz. An adaptive DPG method for high frequency time-harmonic wave propagation problems. *Computers & Mathematics with Applications*, 74(8):1999–2017, 2017.

[249] A. Piacentini and N. Rosa. An improved domain decomposition method for the 3D Helmholtz equation. *Computer Methods in Applied Mechanics and Engineering*, 162(1-4):113–124, 1998.

[250] A. Quarteroni and A. Valli. *Domain Decomposition Methods for Partial Differential Equations*. Numerical Mathematics and Scientific Computation. The Clarendon Press, Oxford University Press, New York, 1999.

[251] C. M. Rappaport. Perfectly matched absorbing boundary conditions based on anisotropic lossy mapping of space. *IEEE Microwave and Guided Wave Letters*, 5(3):90–92, 1995.

[252] C. M. Rappaport. Interpreting and improving the PML absorbing boundary condition using anisotropic lossy mapping of space. *IEEE Transactions on Magnetics*, 32(3):968–974, 1996.

[253] W. H. Reed and T. R. Hill. Triangular mesh methods for the neutron transport equation. Technical report, Los Alamos National Lab, NM, USA, 1973.

[254] R. Renaut. Absorbing boundary conditions, difference operators, and stability. *Journal of Computational Physics*, 102(2):236–251, 1992.

[255] B. Rivière. *Discontinuous Galerkin Methods for Solving Elliptic and Parabolic Equations: Theory and Implementation*. SIAM, 2008.

[256] J. A. Roden and S. D. Gedney. Convolutional PML (CPML): An efficient FDTD implementation of the CFS-PML for arbitrary media. *Microwave and optical technology letters*, 27(5):334–338, 2000.

[257] A. Royer. *Efficient finite element methods for solving high-frequency time-harmonic acoustic wave problems in heterogeneous media*. PhD thesis, University of Liège, Belgium, 2023.

[258] A. Royer, E. Béchet, and C. Geuzaine. Gmsh-Fem: An efficient finite element library based on Gmsh. In *Proceedings of the 14th WCCM-ECCOMAS congress*, pages 1–13, 2021.

[259] Y. Saad. A flexible inner-outer preconditioned GMRES algorithm. *SIAM Journal on Scientific Computing*, 14(2):461–469, 1993.

[260] Y. Saad. *Iterative Methods for Sparse Linear Systems*. SIAM, 2003.

[261] Z. S. Sacks, D. M. Kingsland, R. Lee, and J.-F. Lee. A perfectly matched anisotropic absorber for use as an absorbing boundary condition. *IEEE Transactions on Antennas and Propagation*, 43(12):1460–1463, 1995.

[262] S. Savadatti and M. N. Guddati. A finite element alternative to infinite elements. *Computer Methods in Applied Mechanics and Engineering*, 199(33-36):2204–2223, 2010.

[263] A. Schädle and L. Zschiedrich. Additive Schwarz method for scattering problems using the PML method at interfaces. In *Proceedings of the 16th International Conference on Domain Decomposition Methods*, pages 205–212. Springer, 2007.

[264] K. Schmidt, J. Diaz, and C. Heier. Non-conforming Galerkin finite element methods for local absorbing boundary conditions of higher order. *Computers & Mathematics with Applications*, 70(9):2252–2269, 2015.

[265] A. H. Sheikh, D. Lahaye, L. G. Ramos, R. Nabben, and C. Vuik. Accelerating the shifted Laplace preconditioner for the Helmholtz equation by multilevel deflation. *Journal of Computational Physics*, 322:473–490, 2016.

[266] Siemens Industry Software. Simcenter Nastran User's Guide (Version 2019.2), 2019. https://docs.plm.automation.siemens.com/tdoc/scnastran/2019_2/help/.

[267] P. Solín, K. Segeth, and I. Doležel. *Higher-Order Finite Element Methods*. Chapman and Hall/CRC, 2003.

[268] A. Sommerfeld. *Partial Differential Equations in Physics*. Academic press, 1949.

[269] A. St-Cyr, M. J. Gander, and S. J. Thomas. Optimized multiplicative, additive, and restricted additive Schwarz preconditioning. *SIAM Journal on Scientific Computing*, 29(6):2402–2425, 2007.

[270] C. C. Stolk. A rapidly converging domain decomposition method for the Helmholtz equation. *Journal of Computational Physics*, 241:240–252, 2013.

[271] C. C. Stolk. An improved sweeping domain decomposition preconditioner for the Helmholtz equation. *Advances in Computational Mathematics*, 43(1):45–76, 2017.

[272] B. Stupfel. Improved transmission conditions for a one-dimensional domain decomposition method applied to the solution of the Helmholtz equation. *Journal of Computational Physics*, 229(3):851–874, 2010.

[273] C. K. Tam, L. Auriault, and F. Cambuli. Perfectly matched layer as an absorbing boundary condition for the linearized Euler equations in open and ducted domains. *Journal of Computational Physics*, 144(1):213–234, 1998.

[274] M. Taus, L. Zepeda-Núñez, R. J. Hewett, and L. Demanet. L-Sweeps: A scalable, parallel preconditioner for the high-frequency Helmholtz equation. *Journal of Computational Physics*, 420:109706, 2020.

[275] F. Teixeira and W. Chew. Analytical derivation of a conformal perfectly matched absorber for electromagnetic waves. *Microwave and Optical technology letters*, 17(4):231–236, 1998.

[276] F. Teixeira and W. Chew. Complex space approach to perfectly matched layers: a review and some new developments. *International Journal of Numerical Modelling: Electronic Networks, Devices and Fields*, 13(5):441–455, 2000.

[277] F. Teixeira and W. C. Chew. Systematic derivation of anisotropic PML absorbing media in cylindrical and spherical coordinates. *IEEE Microwave and Guided Wave Letters*, 7(11):371–373, 1997.

[278] F. Teixeira and W. C. Chew. Differential forms, metrics, and the reflectionless absorption of electromagnetic waves. *Journal of Electromagnetic Waves and Applications*, 13(5):665–686, 1999.

[279] R. Tezaur and C. Farhat. Three-dimensional discontinuous Galerkin elements with plane waves and lagrange multipliers for the solution of mid-frequency Helmholtz problems. *International Journal for Numerical Methods in Engineering*, 66(5):796–815, 2006.

[280] R. Tezaur, A. Macedo, C. Farhat, and R. Djellouli. Three-dimensional finite element calculations in acoustic scattering using arbitrarily shaped convex artificial boundaries. *International Journal for Numerical Methods in Engineering*, 53(6):1461–1476, 2002.

[281] B. Thierry, A. Vion, S. Tournier, M. El Bouajaji, D. Colignon, N. Marsic, X. Antoine, and C. Geuzaine. GetDDM: an open framework for testing optimized Schwarz methods for time-harmonic wave problems. *Computer Physics Communications*, 203:309–330, 2016.

[282] L. L. Thompson. A review of finite-element methods for time-harmonic acoustics. *The Journal of the Acoustical Society of America*, 119(3):1315–1330, 2006.

[283] E. F. Toro. *Riemann solvers and numerical methods for fluid dynamics: a practical introduction*. Springer Science & Business Media, 2013.

[284] A. Toselli. Overlapping methods with perfectly matched layers for the solution of the Helmholtz equation. In *Proceedings of the 11th International Conference on Domain Decomposition Methods*, pages 551–557, 1998.

[285] A. Toselli and O. Widlund. *Domain Decomposition Methods - Algorithms and Theory*, volume 34. Springer Science & Business Media, 2006.

[286] O. Vacus. Mathematical analysis of absorbing boundary conditions for the wave equation: the corner problem. *Mathematics of Computation*, 74(249):177–200, 2005.

[287] V. J. van Joolen, B. Neta, and D. Givoli. High-order Higdon-like boundary conditions for exterior transient wave problems. *International Journal for Numerical Methods in Engineering*, 63(7):1041–1068, 2005.

[288] A. Vaziri Astaneh, B. Keith, and L. Demkowicz. On perfectly matched layers for discontinuous Petrov–Galerkin methods. *Computational Mechanics*, 63:1131–1145, 2019.

[289] A. Vion and C. Geuzaine. Double sweep preconditioner for optimized Schwarz methods applied to the Helmholtz problem. *Journal of Computational Physics*, 266:171–190, 2014.

[290] A. Vion and C. Geuzaine. Improved sweeping preconditioners for domain decomposition algorithms applied to time-harmonic Helmholtz and Maxwell problems. *ESAIM: Proceedings and Surveys*, 61:93–111, 2018.

[291] A. Zarmi and E. Turkel. A general approach for high order absorbing boundary conditions for the Helmholtz equation. *Journal of Computational Physics*, 242:387–404, 2013.

[292] L. Zepeda-Núñez and L. Demanet. The method of polarized traces for the 2D Helmholtz equation. *Journal of Computational Physics*, 308:347–388, 2016.

[293] L. Zepeda-Núñez and L. Demanet. Nested domain decomposition with polarized traces for the 2D Helmholtz equation. *SIAM Journal on Scientific Computing*, 40(3):B942–B981, 2018.

[294] L. Zhao and A. C. Cangellaris. GT-PML: Generalized theory of perfectly matched layers and its application to the reflectionless truncation of finite-difference time-domain grids. *IEEE transactions on Microwave Theory and Techniques*, 44(12):2555–2563, 1996.

[295] L. Zschiedrich, R. Klose, A. Schädle, and F. Schmidt. A new finite element realization of the perfectly matched layer method for Helmholtz scattering problems on polygonal domains in two dimensions. *Journal of Computational and applied mathematics*, 188(1):12–32, 2006.